

---

[All ETDs from UAB](#)

[UAB Theses & Dissertations](#)

---

2024

## Mechanical Behaviors Of Additively Manufactured Fiber-Reinforced Thermoplastic Composites

Yu-Chao Shih  
*University of Alabama at Birmingham*

Follow this and additional works at: <https://digitalcommons.library.uab.edu/etd-collection>



Part of the [Engineering Commons](#)

---

### Recommended Citation

Shih, Yu-Chao, "Mechanical Behaviors Of Additively Manufactured Fiber-Reinforced Thermoplastic Composites" (2024). *All ETDs from UAB*. 3902.  
<https://digitalcommons.library.uab.edu/etd-collection/3902>

This content has been accepted for inclusion by an authorized administrator of the UAB Digital Commons, and is provided as a free open access item. All inquiries regarding this item or the UAB Digital Commons should be directed to the [UAB Libraries Office of Scholarly Communication](#).

MECHANICAL BEHAVIORS OF ADDITIVELY MANUFACTURED  
FIBER-REINFORCED THERMOPLASTIC COMPOSITES

by

YU-CHAO SHIH

HAIBIN NING, COMMITTEE CHAIR  
GREGORY W. KUBACKI  
MANOJ K. MAHAPATRA  
SELVUM PILLAY  
SUBHAYU SEN  
VINOY THOMAS

A DISSERTATION

Submitted to the graduate faculty of the University of Alabama at Birmingham,  
in partial fulfillment of the requirements for the degree of  
Doctor of Philosophy

BIRMINGHAM, ALABAMA

2024

Copyright by  
Yu-Chao Shih  
2024

# MECHANICAL BEHAVIORS OF ADDITIVELY MANUFACTURED FIBER-REINFORCED THERMOPLASTIC COMPOSITES

YU-CHAO SHIH

MATERIALS ENGINEERING

## ABSTRACT

Additive manufacturing (AM) technologies are advantageous in small-batch manufacturing and prototyping functional parts, due to their cost-effectiveness and customizability. Using fiber-reinforced plastic composites (FRP) in extrusion-based AM can significantly improve the mechanical properties compared to neat thermoplastic. However, the two-fold anisotropy introduced by the multiple constituent materials and the layer-by-layer mesostructure can introduce undesired structural weaknesses. Investigating the mechanical behavior and failure mechanism is the key to understanding the synergistic effect of the constituents in FRP and assessing the structural integrity of AM-made FRP.

This research work aims to experimentally, analytically, and numerically assess the mechanical behaviors of AM composite to aid in developing parts with better performance. Different loading scenarios were studied, including tensile, sing-lap shear, flexural, and mode I fracture. The failure mechanisms were identified with respect to the structural anisotropy using microscope and numerical simulation. Three studies were presented to address the effects of material and geometrical nonlinearity on the mechanical behavior of AM-made continuous and discontinuous fiber-reinforced polyamide-based thermoplastic composites.

The effects of fiber orientation on tensile responses for the continuous and discontinuous FRP composites were first evaluated. The mechanical responses were

systematically evaluated, incorporating seven reinforcing strategies for two continuous FRP materials: continuous glass and carbon fiber. The mechanical behavior of the anisotropic FRP under large deformation was successfully simulated using finite element analysis. Fracture morphologies of the samples were observed with microscope and analyzed with the corresponding reinforcing strategies in a case-by-case manner.

A single-lap shear configuration was also designed and printed to investigate the mechanical behavior of AM composites under shear stress. Its failure mechanisms were evaluated using fractography to understand the complex stress field caused by the fiber orientation between interfaces. The stress distribution over the bonding interfaces was modeled and correlated to the observed fracture mode. Finally, a series of double cantilever beam samples were printed and tested to assess the interlaminar bonding based on fracture mechanics methodologies. The crack-initiation mode I fracture toughness ( $G_{IC}$ ) value for two continuous FRP was presented. The  $G_{IC}$  for crack propagation was also reported and was found to correspond to geometrical anomalies such as fiber bridging and beam bending.

*Keywords: Additive manufacturing, fused filament fabrication, fiber-reinforced composites, mechanical behavior, failure mechanism, fracture toughness*

## DEDICATION

This work is dedicated to my parents, Peter and Angie, and my lovely wife, Judy.

## ACKNOWLEDGMENTS

Studying in the Materials Processing and Applications Development Center with the polymer composites group is a privilege. The immersive experience of learning from inspiring people and collaborating with them was rewarding. My sincere gratitude to my advisor, Dr. Haibin Ning, is beyond words. His mentorship was profoundly helpful in productive and methodical discussions that guided me throughout the study. The unconditional support and the opportunities he provided during my time in the department are well appreciated. He ensured the success of this thesis with time, patience, and passion while remaining a caring gentleman with high decency.

I would also like to thank Dr. Subhayu Sen for his invaluable conversations to help with the thesis. His experiences taught me to maintain high integrity in scientific activities and demonstrate wisdom in navigating research with an open mind. Many thanks also to Dr. Selvam Pillay for enabling collaboration on practical projects and hands-on experiences. I learned from his leadership, entrepreneurship, and enthusiasm in engineering education. He is a true engineer who delivers things that must be done correctly. Dr. Vinoy Thomas, Dr. Manoj Mahapatra, and Dr. Gregory Kubacki are greatly appreciated for being on the graduate committee and for their time and guidance.

Additional thanks are given to Dr. Robin Foley and Dr. John Griffin for the instant solutions offered throughout my stay in the laboratory with knowledgeable insights. I want to thank late Patrick for being a decent and skillful engineer whom members of the

laboratory all admired and remembered. I appreciate Mr. Daniel Lerew, who has demonstrated principles and an engineering mindset for me to learn, and also as being a responsive safety officer. I appreciate my fellow researchers and students who worked with me, especially Yongzhe Yan, Derrick Armstrong, Shuo Sun, Kirsten Pittman, Cody Johnson, Joydan Jones, Ethan Stonecipher, Garo Trtrian, George Chambers, Dr. Carlos Angulo, Dr. Siddhartha Brahma, Dr. Jun Ge, and Dr. Mahmoud Mohammed, among the others, gave me mesmerizing moments with their precious friendships and intellectual conversations that I cherish.



## TABLE OF CONTENTS

	<i>Page</i>
ABSTRACT .....	iii
DEDICATION .....	v
ACKNOWLEDGMENTS .....	vi
LIST OF TABLES .....	x
LIST OF FIGURES .....	xii
LIST OF ABBREVIATIONS .....	xv
INTRODUCTION .....	1
Additive Manufacturing .....	3
Design for Additive Manufacturing .....	5
Fused Filament Fabrication .....	6
Failure in AMFRP .....	6
Fiber-reinforced Plastic Composites .....	9
Classical Laminated Theorem .....	11
Fracture Mechanics .....	13
Mechanics of Single-lap Joint .....	15
Mechanical Testing of AMFRP Composite .....	18
Objectives .....	19
Organization of the Work .....	20
MATERIALS AND METHODS .....	22
Materials and Equipment .....	22
Design and Manufacturing of AMFRP Composites .....	23
Mechanical Characterization .....	25
Materials Characterization .....	28
Finite Element Analysis for Verification .....	28
ASSESSMENT OF FIBER REINFORCEMENT STRATEGIES FOR ADDITIVELY MANUFACTURED THERMOPLASTIC COMPOSITES USING MECHANICAL TESTING AND FINITE ELEMENT ANALYSIS .....	31

APPLICATION OF INTERLAMINAR SHEAR STRENGTH AND FINITE ELEMENT MODELING FOR FAILURE ANALYSIS OF 3D PRINTED CONTINUOUS FIBER-REINFORCED COMPOSITES.....	65
COMPARISON OF MECHANICAL BEHAVIORS OF FLEXURAL AND MODE I FRACTURE ON ADDITIVELY MANUFACTURED CONTINUOUS FIBER-REINFORCED THERMOPLASTIC COMPOSITES .....	98
OVERALL CONCLUSIONS.....	137
FUTURE WORK .....	141
GENERAL REFERENCES.....	142

## LIST OF TABLES

<i>Table</i>	<i>Page</i>
INTRODUCTION	
1. Advantages and disadvantages of AM compared to molding processes.....	5
ASSESSMENT OF FIBER REINFORCEMENT STRATEGIES FOR ADDITIVELY MANUFACTURED THERMOPLASTIC COMPOSITES USING MECHANICAL TESTING AND FINITE ELEMENT ANALYSIS	
1. Selected specifications and parameters for Mark Two 3D printer, Onyx, CCF, and HSHTG. ....	38
2. Designed reinforcing strategies set for ASTM D638 Type I sample configurations. ...	41
3. Fiber volume fraction of the feedstock filament material.....	46
4. Detailed configurations for all reinforcing strategies. ....	47
5. Tensile test results for fiber-only 3D-printed composites for modeling input. ....	49
APPLICATION OF INTERLAMINAR SHEAR STRENGTH AND FINITE ELEMENT MODELING FOR FAILURE ANALYSIS OF 3D PRINTED CONTINUOUS FIBER- REINFORCED COMPOSITES	
1. Experiment design on single-lap joint shear test for FRP composites.....	73
2. Tensile test results for continuous fiber-only and Onyx-only 3D-printed composites. ....	76
COMPARISON OF MECHANICAL BEHAVIORS OF FLEXURAL AND MODE I FRACTURE ON ADDITIVELY MANUFACTURED CONTINUOUS FIBER- REINFORCED THERMOPLASTIC COMPOSITES	
1. Materials specifications used in this research. ....	106

2. Designed configurations of all three-point bending flexural samples. ....	107
3. Designed double cantilever beam samples and associated beam compositions. ....	110
4. Single-factor ANOVA analysis for 8C, 10C, and 12C for initial, averaged, and Median $G_{IC}$ . ....	122
5. Single-factor ANOVA analysis for 10G, 12G, and 15G for initial, averaged, and Median $G_{IC}$ . ....	122
6. Comparison of $G_{IC}$ data from literature and this research. ....	123

## LIST OF FIGURES

<i>Figure</i>	<i>Page</i>
1. Illustration of extrusion-caused inhomogeneity (a) Extrusion parameters (b) Tool path parameters. ....	8
2. A general 5-stage laminated composites manufacturing procedure.....	10
3. Representative sandwich element and stress resultants to SLJ analysis.....	15
4. Stiffness centroid of the SLJ sample due to eccentric load.....	17

## ASSESSMENT OF FIBER REINFORCEMENT STRATEGIES FOR ADDITIVELY MANUFACTURED THERMOPLASTIC COMPOSITES USING MECHANICAL TESTING AND FINITE ELEMENT ANALYSIS

1. Reinforcement strategies on each configured specimen's group. ....	42
2. Engineering drawing and dimension of the tensile specimen.....	43
3. (a) Complete workflow to simulate 3d-printed composites using ANSYS (b) Boundary conditions applied in the numerical model, (c) Perspective view - the half model for CF-50-8.....	44
4. Cross-sectional microscopic images for fiber characteristics measurement of (a) Onyx filament, (b) CCF filament, (c) HSHTG filament. ....	46
5. Cross-sectional images of printed CFRP specimen. ....	47
6. Tensile modulus of tested configurations by order of cross-sectional fiber fraction. ....	49
7. Tensile strength of tested configurations by order of cross-sectional fiber fraction. ....	50
8. Effective tangent modulus to total strain for (a) A1, (b) A2, and (c) modeling input for Onyx.....	51
9. (a) Delamination over the x-z surfaces for samples A3 and A4 (b) Wedge failure over the neck-gauge region on group B and C samples. ....	52

10. Corrected cross-sectional fiber fraction to failure strain for all specimens. ....	53
11. Comparison of empirical results and modeled tensile responses numerically. ....	55
12. Stress-strain curve of tested and simulated 50%(left) and 100%(right) Onyx data....	56
APPLICATION OF INTERLAMINAR SHEAR STRENGTH AND FINITE ELEMENT MODELING FOR FAILURE ANALYSIS OF 3D PRINTED CONTINUOUS FIBER- REINFORCED COMPOSITES	
1. Physical defects in continuous fiber-reinforced plastic composite fabricated with extrusion-based additive manufacturing.....	67
2. Typical failure modes of conventional additively manufactured continuous fiber-reinforced plastic composites.....	69
3. Single-lap joint specimen design, (a) isometric view, (b) engineering drawing.....	72
4. Schematics of fiber layout sequences over the bonded joint for the SLJ specimen design.....	74
5. Comparison of all SLJ results by group.....	77
6. Load-displacement curves of all group M results with Onyx baseline.....	80
7. Result of SLJ strength of continuous FRP composites on groups M and N.....	81
8. 95% confidence interval of the mean on all CFRP composites (M, N, O).....	81
9. Failure mode determination of SLJ specimen. ....	82
10. Interlaminar fracture identification for all SLJ specimens. ....	83
11. Single-lap shear results for continuous fiber-reinforced composites with different fiber layups between adjacent interlaminar layers. ....	84
12. The simulated normalized stress distribution along the normalized x location. ....	86
13. FEA result of shear stress distribution - symmetrical adherends.....	87
14. Normalized stress distribution on CFRP samples with symmetrical adherends for ILSS and peel. ....	88
15. FEA result of shear stress distribution – asymmetrical adherends. ....	88
16. FEA result of shear stress distribution – semi-symmetrical adherends. ....	89
17. Comparison of calculated and simulated average interlaminar shear stresses. ....	90

# COMPARISON OF MECHANICAL BEHAVIORS OF FLEXURAL AND MODE I FRACTURE ON ADDITIVELY MANUFACTURED CONTINUOUS FIBER- REINFORCED THERMOPLASTIC COMPOSITES

1. Engineering drawing of the three-point-bending test and schematics. ....	107
2. Engineering drawing of the double cantilever beam sample and schematics.....	109
3. (a) Testing fixture and load blocks for DCB test, (b) the moving microscope recording DCB test. ....	113
4. Flexural (a) modulus and (b) strength for CCF and HSHTG samples. ....	117
5. Flexural stress-strain curve for (a) CCF and (b) HSHTG samples. ....	118
6. Flexural modulus to CFF content relationship with available data from the literature ....	119
7. Mode I fracture toughness for crack initiation and crack propagation for (a) CCF-CCF and (b) HSHTG-HSHTG interfaces. ....	120
8. Reduced load-displacement data points for crack propagation in CCF samples.....	124
9. Reduced load-displacement data points for crack propagation in HSHTG samples.....	125
10. Comparison of all mode I fracture toughness for crack initiation and crack propagation regarding the nominal crack length for CCF samples. ....	126
11. Comparison of all mode I fracture toughness for crack initiation and crack propagation regarding the nominal crack length for HSHTG samples. ....	127
12. The reduced load-displacement curve for crack propagation for all DCB samples. ....	128
13 (a) Upper side of the HSHTG samples signals microcrack coalescence over the outermost fiber layer, (b) Fracture surface of the CCF samples, (c) Fiber bridging on the side of DCB samples for HSHTG(left) and CCF (right).....	129

## LIST OF ABBREVIATIONS

AM	Additive manufacturing
AMFRP	Additively manufactured fiber-reinforced plastic
ANOVA	Analysis of variance
APDL	Ansys parametric design language
ASTM	American Society for Testing and Materials
CAE	Computer-aided engineering
CCF	Continuous carbon fiber
CFF	Continuous fiber filament
CFR	Continuous fiber reinforcement
CFRP	Continuous fiber-reinforced plastic
CFRTP	Continuous fiber-reinforced thermoplastic
CLT	Classical laminated theorem
DCB	Double cantilever beam
DfAM	Design for additive manufacturing
DfMA	Design for manufacturing and assembly
DOE	Design of experiment
DoF	Degree of freedom
EBAM	Extrusion-based additive manufacturing



## LIST OF ABBREVIATIONS (Continued)

FEA	Finite element analysis
FFF	Fused filament fabrication
FRP	Fiber-reinforced plastic
FVF	Fiber volume fraction
HSHTG	High-strength-high-temperature glass
ILSS	Interlaminar shear strength
LEFM	Linear elastic fracture mechanics
MBT	Modified beam theorem
MEAM	Material extrusion additive manufacturing
NASA	National Astronautics and Space Administration
PA 6	Polyamide 6
ROM	Rule of mixture
RP	Rapid prototyping
RVE	Representative volume element
SLA	Stereolithography
SLJ	Single-lap joint
TRL	Technology readiness level
VAS	Volume average stiffness

## INTRODUCTION

A composite material comprises of at least two distinctive constituents bonded together, in which those constituents work synergistically to achieve high strength and rigidity [1]. The composite material is widely used in energy and aviation industries owing to its high specific modulus and strength for lightweight structure [2]. Continuous fiber-reinforced thermoplastic (CFRTP) composite excels as a structural material because it provides outstanding specific strength, great toughness, reasonable maintenance cost, and exceptional customizability [3]. Automation for CFRTP composite manufacturing has been widespread to promote the productivity and quality of the products by reducing processing time and retaining optimal morphologies for performance. One of the newer automated manufacturing processes is additive manufacturing (AM) technology.

AM was first developed in the 1860s for rapid prototyping purposes to deliver replicas of three-dimensional models, and it was later commercialized during the 1980s [4]. The layer-by-layer nature of AM objects originated from the principle of production by accumulating materials with linear and laminar deposition onto the build surface [3,5-7]. The modular nature of AM technologies correlates well with close-loop pollution control, which is well-sought by governing bodies around the globe for sustainable economic growth. AM is also believed to be the next centerpiece of the industrial 4.0 revolution [8] because of its highly digitized workflow. Although polymers have the largest market share by materials type in 2021 [4], their poor structural performance is a significant

barrier to implementing polymer AM in demanding applications. In light of the performance in the need for polymer AM, using fiber as reinforcements to manufacture CFRTP was increasingly common. CFRTP composite components can be manufactured on-demand and on-site with extrusion-based AM technologies [9,10], such as fused filament fabrication (FFF), to deliver performance-driven engineering design in small quantities with high flexibility.

This work focuses on studying the mechanical behavior of additively manufactured fiber-reinforced plastic (AMFRP) composite materials with different configurations under different stress scenarios to provide process-structure-property knowledge, enhance product performance, and avoid faulty designs that could fail prematurely. Mechanical failure of materials is a multi-scale phenomenon governed by a collection of disintegration mechanisms across nucleation of microscopic defects, coalescence of mesostructured cavities, and macroscopic deformation of the body that enables sudden decohesion of materials caused by concentrated stresses. The lack of robust criteria to predict and prevent failure has been the limiting factor for composite applications to achieve their full potential [2]. It is at the forefront of the research to develop generalized formulations based on physical observations [11,12]. Many analytical and numerical tools were implemented to analyze the failure behavior of CFRTP to validate the flightworthiness of composite components in aeronautic applications [13-16] and other lightweight applications [14,17]. Analysis of mechanical behavior generally starts with a series of monotonic mechanical tests on simple geometries to gather baseline properties, followed by identification of fracture mode and stress field from numerical simulation to aid in analysis at the part design level.

The anisotropic mechanical responses of AMFRP composite structures were investigated to evaluate the dependence of the mechanical behavior regarding the reinforcing strategies, such as concentric reinforcement, fiber volume fraction, fiber orientation, and infill percentage. Test specimens of tensile test, single-lap joint shear test, double cantilever beam test, and three-point-bending flexural test were produced by a fused filament fabrication (FFF) printer with filament feedstock materials, including a matrix material of polyamide-based thermoplastic reinforced with chopped carbon fiber and two composite feedstocks reinforced by continuous carbon fiber and continuous glass fiber. The mechanical tests were performed, and the resulting microscopic and fractographic images were analyzed to identify the critical failure mechanisms of those AMFRP samples. In addition, modeling was carried out on those samples to further explain the mechanical behaviors of the AMFRP composites. The nonlinear responses of AMFRP composites were modeled numerically and analytically with representative ply properties and a strain-based failure criterion. Statistics were introduced to quantify and visualize the effect of fiber orientation on their resulting mechanical responses. The establishment of AMFRP failure analysis was evaluated under the framework of beam analysis, laminated theorem, and fracture mechanics.

### Additive Manufacturing

Additive manufacturing, or rapid prototyping (RP), is a trending technology for its compact modular design, precise and customizable deposition to produce performance-driven objects, and outstanding waste and pollution control in the process [18]. It is also called 3D printing, which is denoted by replicating objects with a typography-like

process in two-dimensional ink deposition. Research on additive manufacturing has been spotlighted and funded extensively by world-leading countries [19]. It has the potential to revolutionize manufacturing and enable technology to help deploy novel materials on advanced applications [19,20]. The history of AM can be traced back as early as the late 19th century when photosculpture was proposed by Francois Willeme of France in 1860 to replicate a three-dimensional object [21]. Stereolithography (SLA) was the first patented modern AM technology in 1986 by 3d Systems [22].

AM is a fabrication method for producing three-dimensional objects by material deposition and accumulation, for which traces and layers of material are chemically or physically bonded. A CAD design is first developed using 3D CAE software, and the slicing software is used to generate the toolpath for 3D printing of the design [18]. The fabrication process is managed with material or energy deposition by raster movement of the printing outlet, commonly controlled by a series of programmed G-codes, to guide the material deposition by the tool path file [6]. AM offers ease of design iteration with minimum tooling requirements, enabling flexibility for shortening product development cycles and in-house research integration. Available materials on the AM printer have been expanded to a good portfolio that enables direct part manufacturing, including numerous metal alloys, engineering plastics, biocompatible materials, and FRP composites [23].

Polymer-based single-step AM was categorized in ASTM/ISO 52900:2015 for additive manufacturing's general principles and terminologies as six subcategories: material extrusion (ME), material jetting (MJ), powder bed fusion (PBF), binder jetting (BJ), sheet lamination (SL), and vat photopolymerization (Vat or SLA). Some advantages and

disadvantages of AM compared to the conventional molding process are summarized in **Table 1** below.

Table 1. Advantages and disadvantages of AM compared to molding processes.

	Advantages	Disadvantages
Pro- cess	<ul style="list-style-type: none"> <li>• Low tooling cost</li> <li>• Short iteration cycle</li> <li>• Flexible to change of design</li> <li>• Low minimum quantity requirement</li> </ul>	<ul style="list-style-type: none"> <li>• Higher cost for feedstock material</li> <li>• High cycle time per product</li> <li>• Lack of scalability to drive down cost</li> </ul>
Prod- uct	<ul style="list-style-type: none"> <li>• Eliminate subassembly</li> <li>• Performance-driven design</li> <li>• Enable structure that cannot otherwise be made</li> </ul>	<ul style="list-style-type: none"> <li>• Anisotropy structural performance</li> <li>• Systematic voids result in a lower structural integrity</li> <li>• Susceptible to structural debonding</li> <li>• Surface finish is required</li> </ul>

### Design for Additive Manufacturing

Design for additive manufacturing (DfAM) is bounded by specific sets of manufacturing constraints induced by the discontinuity of materials and energy deposition, which is analogous to design for manufacturing and assembly (DfMA) [24,25] and for measures to deliver functional components effectively. Research in DfAM connects the dots in design and manufacturing to account for the procedural factors of each AM method [26] to the performance outcome. From the material standpoint, design strategies for additive manufacturing require comprehensive knowledge of the process-structure-property interrelationship of the materials. Bonding of adjacent deposition of materials relies on the dynamics of the gradient flow of energy and mass transportation, resulting in the morphology evolution of the inter-material system. The bonding mechanism between the lamina and polymer melt directly results from intimate contact and interfacial diffusion driven by temperature gradient, pressure, and material flow [27].

The approach in this study provides a guideline to enable the effectively reinforced AMFRP structural designs to account for the dual anisotropy of AMFRP.

### Fused Filament Fabrication

Fused filament fabrication (FFF), or fused deposition modeling (FDM), is an extrusion-based additive manufacturing (EBAM) technology that fabricates a solid object layer-by-layer with depositions of molten materials. The assembly used for the deposition of material is generally known as a hot end, comprising a feedstock inlet pipeline guided by a friction-induced feeding mechanism and a hot extrusion zone composed of a thermocouple, a heatsink block, thermostats, and an outlet nozzle [6]. Some processing parameters that were investigated for correlation to the performance of FFF-made objects include raster angle, printing speed, layer height, and infill percentage [28-30]. The main shortcoming of FFF is the inherent anisotropic structure, like any other AM technology, due to the effect of the thermal gradient introduced throughout the deposition process [31]. FFF machines can be equipped with multi-extrusion outlets to fabricate multi-material composites with control on alternate deposition. EBAM also shares an architecture identical to other polymer extrusion processes used to manufacture FRP. Therefore, adapting the well-developed principle of modeling and optimization in other extrusion processes provides a solid technical foundation for EBAM studies.

### Failure in AMFRP

Material engineers and scientists have always highlighted the occurrence of decohesion on physical objects. The efforts to approach an adequate representative criterion for

FRP composites to account for mechanical behaviors in microscopic and macroscopic scales have been well documented [32]. The primary decohesion mechanisms of FRP composite materials include interply cracking, matrix cracking, interlaminar delamination, and fiber breakage due to multi-scale anisotropy [33,34]. Microcrack initiation can occur within the interfacial bonding area between the fiber and matrix of the FRP composite, resulting in premature failure from incidences of debonding or delamination [35]. Stress-based and energy-based criteria are two major criteria used in the engineering design assessment [36]. Stress-based criteria can be evaluated with the result of characterization by applying monotonic stresses on materials undergoing specific bounded stresses, such as tensile and compression [37,38]. On the other hand, energy-based criteria can be derived empirically based on the principle of fracture mechanics, in which the occurrence of fracture can be permitted once a threshold energy value has been exceeded [39]. Other semi-empirical failure criteria widely used in FRP composites, such as Tsai-Hill, Tsai-Wu, LaRC, and Hashin, are used to model the fracture occurrence and guide the structural design of composite fuselages, body panels, and military jet engines [40].

In addition to the typical failure mode for FRP, crack initiation in AMFRP can also be promoted from non-homogeneous boundaries from the non-isothermal cooling, unfilled volume from the printing process, and lack of consolidating pressure. Two principal physical defects were identified in AMFRP composites: voids and inadequate bonding. The principle of FDM lies in a controlled tool path to deposit materials and accumulate beads into lines, lines into lamina, and lamina into the body. The coded raster motion of the material outlet introduces discontinuous constraining conditions over the stages of melting, depositing, solidifying, and consolidating. Voids were embedded into the matrix structure



as the extrusion line morphed from the round nozzle to an elliptical shape after extrusion, while the only constraining factors to the molten filament were the puller, the extruder nozzle, and the print bed.

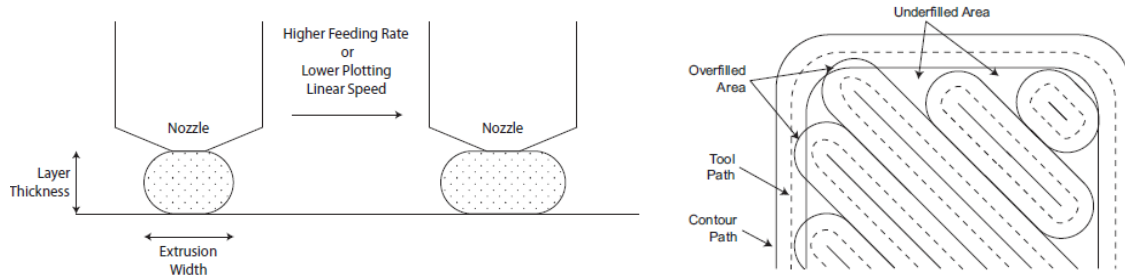


Figure 1. Illustration of extrusion-caused inhomogeneity (a) Extrusion parameters (b) Tool path parameters.

(Note: From “Fused deposition modeling with polypropylene” by O.S. Carneiro, A.F. Silva, and R. Gomes, 2015, *Materials & Design*, 83, p. 9. Copyright 2015 by Elsevier. Reprinted with permission [41])

Illustrations of the physical defects regarding the processing are shown in **Figure 1**. Patterned voids would be embedded beneath each string of deposited materials and the resulting lamina when the material flow solidifies before filling the gaps. Inadequate bonding can happen on the inter-raster, interlayer, and wall-infill interfaces, which would be prone to debond/decohesion type failure. Critical parameters that could be optimized to alleviate the formation of physical defects include nozzle diameter, layer height, fan speed, overlap percentage, and flow compensation multiplier.

The study adopted an integrated approach to examine the failure mechanisms for the AMFRP structures using fracture analysis, finite element analysis, and microscopic images. Their correlation to the mechanical responses of the fiber-reinforced plastic undergoing different loading scenarios was evaluated.

## Fiber-reinforced Plastic Composites

For decades, FRP composites have been integrated into essential structural components to achieve higher energy efficiency for lightweight structures, such as the fuselage structure for commercial aviation vehicles. The first groundbreaking commercial use of FRP on the Boeing 787 Dreamliner utilizes more than 50% by weight with carbon fiber reinforced thermoset plastic composites [42]. Most of the 787 fuselage structures comprised laminated CFRP, while some advanced sandwich panels are also used, with their core made of an aluminum alloy honeycomb structure. To manufacture CFRP composite parts, the woven or nonwoven fabric was first cut to shape and laid inside the mold to constitute a laminated pre-form, then subsequently impregnated with the matrix polymer material via a resin infusion, an over-molding or an autoclave process to combine the constituents. Conventional processing techniques include hand layup, resin transfer molding (RTM), automated tape placement (ATP), and sheet molding compound (SMC) [1]. CFRP composites offer direction-catering high specific strength for energy-intensive applications such as aeronautic vehicles and energy industries. On the contrary, long fiber thermoplastic (LFT) is another popular option for applications that require endurance for economical long-term operation and improved mechanical performance [43]. **Figure 2** illustrates the general FRP processes required in a development and manufacturing cycle.

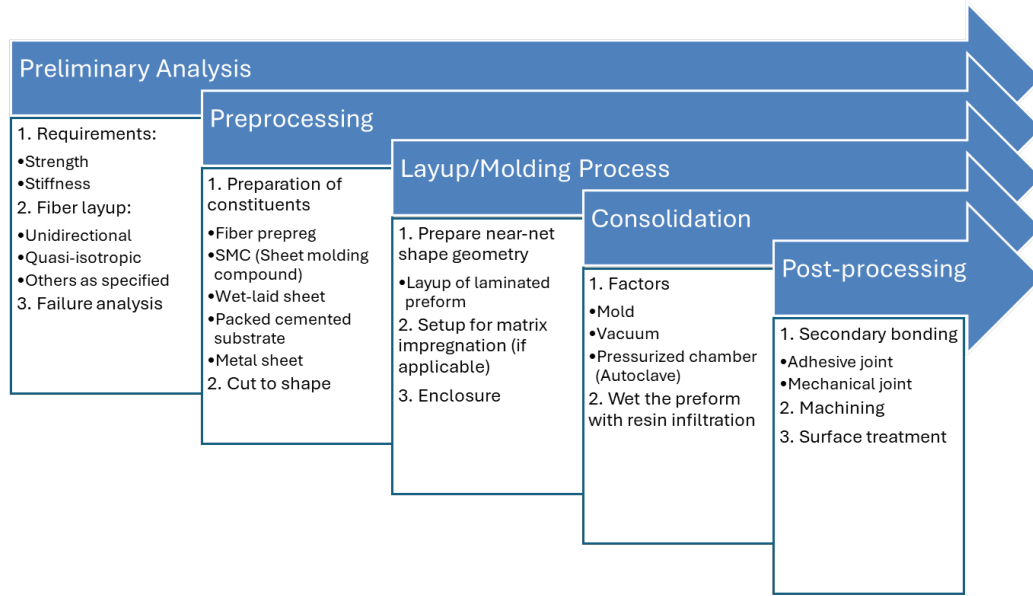


Figure 2. A general 5-stage laminated composites manufacturing procedure.

There is an ongoing effort to develop more thermoplastic composites, due to the concern of a large amount of unrecyclable thermoset composite scrap [44] disposed of annually. This results in the emerging trend to replace the current state-of-the-art CFRP made by tough yet not eco-friendly thermosets with more sustainable thermoplastic composites. CFRTP offers high specific strength, reasonable recyclability, medium impact resistance, and the ability to tailor application properties. The mechanics of composite materials are somehow complex as they are anisotropic materials, while in most cases, they can be simplified as orthotropic materials for laminated composites for analysis. The interfacial bonding quality is essential in the overall performance as the debonding between constituents can result in premature failure.

Interest in studies in AMFRP has been increasing in recent years [5,45,46] for the opportunity to manufacture CFRP using compact EBAM machines for any engineering facility. During the FFF process, the fiber length in FRP is preserved with low shear forces,

providing good strength for FRP composites [43]. Another advantage of using FFF is that it enables a higher degree of fiber alignment for discontinuous FRP to improve the composite's mechanical properties [7]. The surface treatment, conformity, wettability, defects, voids, and diffusion all contribute to the performance of the AM products.

The approach used in this study effectively created an FRP composite structure composed of two distinctive fiber-reinforced plastics, namely a discontinuous fiber-reinforced thermoplastic and a continuous fiber-reinforced thermoplastic filament. The synergistic effects of the combination regarding their non-trivial mechanical responses were investigated.

#### Classical Laminated Theorem

Classical laminated theorem (CLT) is used extensively in modeling the stiffness matrix and other material constants for composite materials that normally have anisotropic material properties. The properties required by the numerical modeling [1] evaluation can also be partially derived with analytical models with minimal mechanical testing.

A general notation to predict elastic constant for an orthotropic lamina under plane stress conditions can be expressed as:

$$\begin{bmatrix} \sigma_x \\ \sigma_y \\ \tau_{xy} \end{bmatrix} = \begin{bmatrix} Q_{11} & Q_{12} & 0 \\ Q_{12} & Q_{22} & 0 \\ 0 & 0 & Q_{66} \end{bmatrix} \begin{bmatrix} \varepsilon_1 \\ \varepsilon_2 \\ \gamma_{12} \end{bmatrix} \quad (1)$$

in which  $Q_{ij}$  are the elements of the stiffness matrix,  $\sigma_x, \sigma_y, \tau_{xy}$  are the principal stresses in x, y and shear direction, and  $\varepsilon_1, \varepsilon_2, \gamma_{12}$  are the corresponding principal strains.

Off-axis ply properties can be calculated with the coordinate transformation:

$$\begin{bmatrix} \sigma_x \\ \sigma_y \\ \tau_{xy} \end{bmatrix} = \begin{bmatrix} m^2 & n^2 & -2mn \\ n^2 & m^2 & 2mn \\ mn & -mn & -n^2 \end{bmatrix} \begin{bmatrix} \sigma_1 \\ \sigma_2 \\ \sigma_3 \end{bmatrix} \quad (2)$$

$$\begin{bmatrix} \varepsilon_1 \\ \varepsilon_2 \\ \gamma_{12} \end{bmatrix} = \begin{bmatrix} m^2 & n^2 & mn \\ n^2 & m^2 & -mn \\ -2mn & 2mn & m^2 - n^2 \end{bmatrix} \begin{bmatrix} \varepsilon_x \\ \varepsilon_y \\ \gamma_{xy} \end{bmatrix} \quad (3)$$

where  $m = \cos\theta$  and  $n = \sin\theta$ , and the resultant stiffness matrix can be used in numerical analysis. The lamination theory also defines the following:  $N_{xx}$  = normal force resultant (per unit width) and  $M_{xx}$  = bending moment resultant, in matrix notation:

$$\begin{bmatrix} N_{xx} \\ N_{yy} \\ N_{xy} \end{bmatrix} = [A] \begin{bmatrix} \varepsilon_{xx}^0 \\ \varepsilon_{yy}^0 \\ \gamma_{xy}^0 \end{bmatrix} + [B] \begin{bmatrix} k_{xx} \\ k_{yy} \\ k_{xy} \end{bmatrix} \quad (4)$$

$$\begin{bmatrix} M_{xx} \\ M_{yy} \\ M_{xy} \end{bmatrix} = [B] \begin{bmatrix} \varepsilon_{xx}^0 \\ \varepsilon_{yy}^0 \\ \gamma_{xy}^0 \end{bmatrix} + [D] \begin{bmatrix} k_{xx} \\ k_{yy} \\ k_{xy} \end{bmatrix} \quad (5)$$

Each [A], [B], and [D] is a 3×3 matrix for the constituted laminate, which

[A] = extensional stiffness matrix, [B] = coupling stiffness matrix, [D] = bending stiffness matrix, in which the resultant stiffness matrices for a laminated structure is

$$A_{mn} = \sum_{j=1}^N (\bar{Q}_{mn})_j (h_j^3 - h_{j-1}^3) \quad (6)$$

$$B_{mn} = \frac{1}{2} \sum_{j=1}^N (\bar{Q}_{mn})_j (h_j^2 - h_{j-1}^2) \quad (7)$$

$$D_{mn} = \frac{1}{3} \sum_{j=1}^N (\bar{Q}_{mn})_j (h_j^3 - h_{j-1}^3) \quad (8)$$

where N = total number of laminae in the laminate,  $(\bar{Q}_{mn})_j$  are the elements in the  $[\bar{Q}]$  matrix of the jth lamina,  $h_{j-1}$  is the distance from the midplane to the top of the jth lamina,  $h_j$  is the distance from the midplane to the bottom of the jth lamina.

The classic lamination theory could also be written in a more compact form as [1]

$$\begin{pmatrix} N_i \\ M_i \end{pmatrix} = \begin{bmatrix} A_{ij} & B_{ij} \\ B_{ij} & D_{ij} \end{bmatrix} \begin{pmatrix} \varepsilon_j^0 \\ \kappa_j \end{pmatrix}, (i, j = xx, yy, xy) \quad (9)$$

The ply-wise material properties can then be approximated and adopted in finite element analysis to account for the orthotropic properties by the stack-up sequences. The model can be further corrected with microstructural parameters and data-driven algorithms [47] to account for geometrical defects and voids.

Implementation of the CLT at a ply level to simulate the mechanical responses of AMFRP structures was not previously reported. This study developed and implemented a homogenization method of the material properties at the ply level using empirical data in FEA to simulate the mechanical response. The CLT was used indirectly in the developed FEA models to calculate the material properties of the composites with different fiber configurations. The material properties profile was used as building blocks of the solid models to conduct structural analysis.

### Fracture Mechanics

The principle of fracture mechanics aims to predict mechanical failure when material bears one of the three loading conditions: opening (mode I), in-plane shear (mode II), and out-of-plane shear (mode III). Two distinct yet convertible material properties, the stress intensity factor  $K$  and the strain energy release rate  $G$ , are referred to as fracture toughness, which can be calculated using an expanded version of the principle of conservation of energy and characterized experimentally. Some noticeable characterization

methods for mode I, mode II, and mixed-mode I/II fracture toughness are double cantilever beam (DCB), end-notched flexural (ENF), and mix-mode bending (MMB), respectively.

First started from Griffith's pioneering work, the energy-based fracture mechanics govern the brittle fracture with the thermodynamic approach [48]. Linear elastic fracture mechanics (LEFM) was first proposed to model the brittle fracture of concrete [49]. In response to the energy balance for the incidence of a fracture, the work done by the load is equivalent to the summation of surface energy to form the new surface area to permit crack initiation and propagation. Fracture mechanics was developed to model the mechanical responses without encountering singularity issues in the vicinity of the crack tip. Various data reduction schemes can be used to calculate fracture parameters as material properties, including the virtual crack closure technique (VCCT), the J-integral, and the compliance derivative technique (CDT). LEFM can also be expanded to provide valuable insights into treating materials that display linear inelasticity, such as functionally graded materials (FGM) [50], composite materials [51], and elastic film [52]. Although fracture toughness is widely accepted and applied in structural safety evaluation, high in-group variability can be observed in the available  $G_{IC}$  data for crack propagation [51], showing evidence for the unsteady nature of the fracture behavior. As a result, the initial fracture toughness is recommended for design purposes for a higher safety factor [53]

The evidence of the fluctuation of fracture toughness during crack propagation manifests the occurrence of collateral fracture incidents, such as fiber bridging or plastic deformation of the beam. Therefore, the propagation fracture toughness is usually considered geometry and material-specific. The incidents described will be corroborated with the findings reported in the third study of this dissertation.

## Mechanics of Single-lap Joint

SLJ sample is designed to evaluate the interfacial bonding strength, typically referred to as the single-lap shear strength [54-56]. The SLJ sample design comprises two thin beams with an overlapping bonding area, which undergoes tensile loading to find the shear strength of the adhesion between two lapped bodies. SLJ strength is a function of many crucial parameters, such as adhesive shear modulus, adhesive layer thickness, adherend tensile modulus, adherend thickness, the overlap length, and tensile stress in adherends away from the joint [57]. The free-body diagram and the equivalent sandwich element are shown in **Figure 3**. The critical boundary conditions and terminology illustrated include:  $P$  is the longitudinal load,  $M$  is the edge moment induced by beam deflection, and  $V$  is the edge shear force. These parameters are essential to constitute analytical equilibrium in the system to evaluate overall stress status. As adherends outside the bonded region are marked as sections 1 and 4, the stress analysis is approximated over the interfaces between sections 2 and 3.

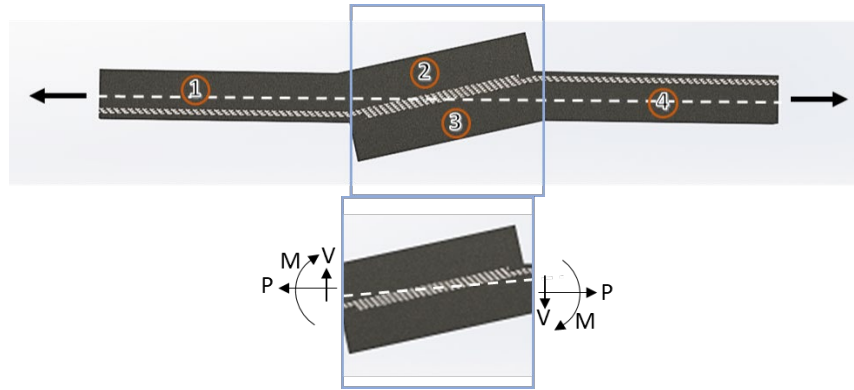


Figure 3. Representative sandwich element and stress resultants to SLJ analysis. (Adapted from [58] )

Under the equivalent sandwich element notation used in classical analytical models [54,58], the elastic strain energy of the joint is calculated from the equation below



$$W = \int_{-c}^c \int_0^t \left\{ \frac{1-\nu^2}{E} \left[ \sigma_x^2 + \sigma_y^2 - \frac{2\nu}{1-\nu} \sigma_x \sigma_y \right] + \frac{1}{G} \tau_{xy}^2 \right\} dx dy + \frac{1}{2} \eta \int_{-c}^c \left\{ \frac{1}{E_c} \sigma_0^2 + \frac{1}{G_c} \tau_0^2 \right\} dx \quad (10)$$

where  $E$ ,  $G$ ,  $\nu$  represent Young's modulus, shear modulus, and Poisson's ratio of the sheet material, respectively. Applying the classical expression for infinitesimal bending of thin cylindrically deformed plates, the resulting moment and shear force between the adherend and the lap are

$$M_0 = k \frac{Ft}{2} \quad (11)$$

$$V_0 = kF \sqrt{\frac{3(1-\nu^2)Ft}{E}} \quad (12)$$

where  $k = \frac{\cosh \Lambda}{\cosh \Delta + 2\sqrt{2} \sinh \Lambda}$ , and  $\Lambda = \sqrt{\frac{3(1-\nu^2)}{2}} \frac{c}{t} \sqrt{\frac{Ft}{E}}$ ,  $M$  is the bending moment, and  $V$  is the transverse shear force on the adherend.

Load eccentricity can be introduced due to the adherend bending over the unsupported ends, and the additional torque would be present, as shown in **Figure 4**. The stiffness centroid over the sandwich region,  $EC$ , could be used as an indicator of the degree of stiffness imbalance with the modified formulations from Hart-Smith's analysis: [58]

$$EC_1 = \frac{\frac{1}{2}(t_1+t_4)}{\left(1 + \frac{E_1 t_1}{E_4 t_4}\right)} \quad (13)$$

$$EC_4 = \frac{\frac{1}{2}(t_1+t_4)}{\left(1 + \frac{E_4 t_4}{E_1 t_1}\right)} \quad (14)$$

in which  $t$  and  $E$  are the adherend's thickness and stiffness, respectively. The resulting centroid would vary by configuration and can be put into parametric analysis to compare the effect of beam asymmetry.

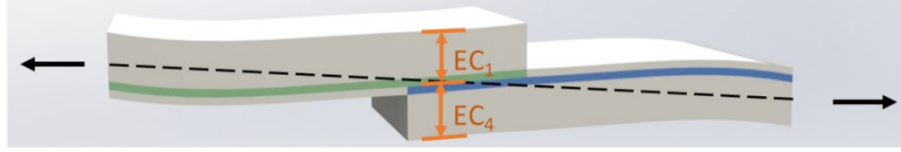


Figure 4. Stiffness centroid of the SLJ sample due to eccentric load.

A lap shear test is usually conducted to examine the interlaminar bonding of adhesives on a quantitative and comparative basis. Goland and Reissner's lap shear model suggests that peel strength prevails under certain dimensional conditions [59]. The single-lap joint test also measures the structural integrity of an interlaminar area between two adherends. Because the lap shear load is a mixture of peel and shear, the acquired strength cannot be directly used for design purposes. An SLJ sample would commonly require symmetrical adherends to reduce the stress concentration over the free edges right next to the bonded interface; however, samples with asymmetric flexural rigidity were also tested in some cases.

The use of the SLJ shear test to examine the interfacial bonding between the layers of the AM composites is understudied. No previous literature was found to address the non-uniform stress distribution of the bonded interface and the stress concentration caused by the beam bending and rotation. The study used a series of SLJ samples made of AMFRP structures to examine the stress within the designed interlaminar bonding interfaces. The failure modes of the AM composites were determined from the fractographic and microscopic images.

## Mechanical Testing of AMFRP Composite

Blok. et al. [60] conducted tensile, flexural, and shear tests on 3D-printed carbon fiber composite. The work estimates the fiber volume fraction (FVF) on the continuous carbon fiber to be 27%. Caminero. et al. [61] characterized the impact resistance of AMFRP using a V-notched specimen following ASTM D6110- Standard test method for determining the Charpy impact resistance of notched specimens of plastics. Results show that the composite samples reinforced with carbon fibers exhibited lower impact strength than those with glass and Kevlar fibers. Dickson. et al. [62] conducted an ANOVA study on continuous FRP reinforced with aramid, carbon, and glass fiber. Flexural and tensile data were correlated with the parameters implemented. Matsuzaki. et al. [63] estimate the upper limit of fiber reinforcement efficiency to be 40%-50% for FDM-based 3D-printed continuous FRP.

It is challenging to determine the shear stress of the material as the other stress components cannot be entirely separated from the analysis. Selected research works that analyzed the identical materials and processes are described below. Araya. et al. [64] characterized the compressive and flexural properties of continuous FRP with three groups of testing: (a) concentric or isotropic reinforcement, (b) center or shell, or both, (c) 0 / 90. The result suggests a statistical significance between different print parameters. Naranjo. et al. [65] conducted an analysis of variance (ANOVA) study on the AMFRP's tensile properties and processing parameters. Their results suggest that the infill percentage has a minor effect on tensile properties when multiple reinforcing strategies are present. Failure occurs differently when the continuous fiber starts at a different location, indicating that the layout starting location affects tensile strength significantly.

Interlaminar fracture toughness (IFT) research work is reviewed as follows. Valoroso. et al. proposed a data reduction method to find mode I fracture toughness on aluminum-filled epoxy-bonded aluminum adherent with DCB testing [66], and the results were used in FEA modeling. Camanho. et al. [67] proposed a new zero-thickness volumetric decohesion element for composite laminates. The 8-node element can account for the softening effect and can be used to aid fracture mode identification. The proposed element was applied to DCB, ENF, and MMB specimens, and a comparison was made with experimental data. Maimi. et al. [68] used a new constitutive model for failure analysis of composite laminate based on four different failure modes. Li. et al. [69] proposed a two-parameter cohesive zone model (CZM) formulation to account for the Mode I parameter and verified the result by testing single edge-notched specimens.

### Objectives

The four objectives of the research are:

1. Design and manufacture of additive manufactured fiber-reinforced thermoplastic composites to validate the reinforcing strategies using fractography, mechanical tests, and finite element simulation.
2. Develop a comprehensive workflow to simulate the nonlinear mechanical response of additively manufactured discontinuous and continuous fiber-reinforced plastic composite to assess the structural performance of designed AMFRP configurations.
3. Design, manufacture, and verify the complex stress field of AMFRP composite using a single-lap joint sample regarding the characteristic multi-scale structural anisotropy. The

complex stress field of interfacial bonding quality to the mechanical behavior of each neighboring plies was analyzed and correlated to the variations of failure mode.

4. Design, manufacture, characterize, and verify the mode I fracture toughness of AMFRP composite considering composition variants of the beam with different flexural rigidity.

### Organization of the work

First, a literature review is presented to identify state-of-the-art on the relative field in additively manufactured fiber-reinforced plastic composite materials. The goals, novelties of the research, and the structure of the dissertation are also included here. Second, the design methodologies, materials, processing methods, characterization methods, and analytical approaches used in this study were introduced.

Three distinctive yet interconnected studies resonating with the AMFRP's mechanical behaviors were presented. The goal of the first manuscript is two-fold: to evaluate the effectiveness of fiber reinforcement strategies for AMFRP and to develop and verify the feasibility of an FEA modeling scheme concerning the nonlinearity of continuous and discontinuous FRP composites. The design of the experiment (DOE) was conducted to find the relevances of the processing parameters and the mechanical performances of AMFRP. Microstructural analysis, fractography, and stress-strain responses were compared to identify the effect of mesostructured anisotropy.

The second manuscript delves into the failure mechanics of a 3D-printed FRP single-lap joint sample concerning the complex stress field over the interfacial area. The SLJ

strength was found to be a function of fiber orientation over the interfacial area.

Multiple failure modes were observed by the fractography analysis and were compared to the finite element method results, revealing that a complex stress field can be generated by the geometrical nonlinearity of the 3D-printed FRP composites with multiple fiber reinforcing strategies.

The third manuscript aims to characterize the flexural responses and the mode I fracture toughness in strain energy release rate for thin laminated AMFRP. The beams of varying flexural stiffness by different fiber orientations were used to monitor the effect on fracture responses of AMFRP composites. The fracture and flexural responses were analyzed with fractography and statistics to find a correlation between the characterization results and effective fiber volume fraction.

## MATERIALS AND METHODS

### Materials and Equipment

A discontinuous carbon-fiber-reinforced polyamide 6 thermoplastic composite, referred to as the matrix material of the AMFRP structure, was used to manufacture all samples. The matrix material is reinforced with less than 10% chopped carbon fiber [70] for reinforcement. Two continuous fiber filament feedstocks were used as reinforcement for some samples to evaluate the effectiveness of configurations and analyze the failure mechanisms. The feedstock filaments were pre-impregnated continuous carbon fiber (CCF) filament and high-strength-high-temperature glass (HSHTG) fiber filament, both supplied by Markforged Inc. (MA, USA). The materials here designated as continuous fiber filaments are continuous fiber reinforced thermoplastic composites with around 30% of equivalent fiber volume fraction, characterized by microscopy studies and image processing software. Owing to the closed-source nature of the AM machine used, the print speed, layer height, and print temperature are all predefined.

A desktop extrusion-based additive manufacturing machine, the Mark Two (by Markforged Inc, MA, USA), was used to manufacture all samples with proper treatment to achieve the geometry of interest. A mold release agent, Henkel Loctite Freekote 770-NC, was used to manufacture the desired precrack area and separate matrix layers while manufacturing DCB samples. Two isocyanide-based adhesives, Loctite 414 and Loctite

496, were used to apply adhesive bonding between the AMFRP samples and the steel loading block for the DCB test.

### Design and Manufacturing of AMFRP Composites

The highly digitized nature of AM centers its advantage in synergies with computer-aided engineering (CAE) workflow. The model's design, analysis, manufacture, prototype, and iteration can be integrated to provide advantages to optimize the functional designs with a suitable combination of materials and processing parameters.

#### *Solidworks*

The coupon geometries were designed with CAE software suites Solidworks (Solidworks, Dassault Systems, Tennessee, US) with respected features to reflect the requirements of relevant ASTM standards. Solidworks software has a built-in compiler to produce a stereolithography (STL) file as a 3D model input for slicing purposes to produce AM samples and a Parasolid (x\_t) file as modeling input for finite element analysis.

#### *ANSYS Software*

ANSYS (ANSYS Inc, Tennessee, US) is a multi-physic simulation software suite specializing in structural analysis utilizing finite element methods. The capability to include a wide range of material properties based on state-of-the-art analytical models is valuable in generating high-fidelity structural responses. ANSYS SpaceClaim is a computer-aided design software integrated within the ANSYS suites, providing utility to mark the shared geometries to aid in the computational pipeline. The ANSYS mechanical module has built-in functions for meshing and defining boundary conditions, and its built-in



solver for iterative solutions is powered by Ansys Parametric Design Language (APDL). The ANSYS Composite Crepost (ACP) suite is a Python-based software based on CLT that calculates and applies anisotropic material properties regarding the fiber orientation of each composite lamina. The structural responses of laminated AMFRP composites can be solved numerically with iterations governed by Newton-Raphson methods for analyzing stress and strain fields. The capability of the ANSYS suites was evaluated by NASA and found to be suitable for reproducing physics-based mechanical responses for the delamination of composite materials [71].

### *Eiger Slicer*

The Eiger software (Markforged Inc, MA, USA) is a cloud-based model slicer that slices the digital solid model into sheets of two-dimensional profiles for the printer to fabricate the three-dimensional models in the physical space. The Eiger software has a collection of printing parameters, including infill percentage, printing patterns, counts of wall and flooring layers, and fiber orientation. The fiber orientation can be configured layer-by-layer, providing an excellent platform for experimentation of fiber blending sequences and a highly tailorable direction-oriented properties profile. The processing tool-path file includes printing parameters in the .mfp file format, which can then be used on the printer to fabricate samples.

### *ImageJ*

The image processing capability provided by ImageJ [72] software enables the microscopy analysis from the qualitative evaluation to the quantification of proportionality and characteristics of constituents. Histogram analysis provides information to remove

irrelevant morphologies that are polarized for ease of setup on the threshold. ImageJ is also equipped with feature recognition to identify rounded objects of interest, such as a cross-section of fiber, to enable efficient counting and further binarization to find fiber areal proportionality.

### *Processing of AMFRP Composites*

Samples were made using an extrusion-based desktop composite printer, the Mark Two 3D printer by Markforged Inc. A toolpath file with an .mfp file format is suitable to be read and executed by the printer after the orientation has been configured in Eiger's cloud-slicing system. The Mark Two printer is a closed-source printer with most parameters predefined and limited configurable parameters. Mark Two has a single hot end with dual nozzles neighboring each other, capable of printing matrix thermoplastics and pre-impregnated continuous fiber filament. The Mark Two also has a modified Bowden-style feeding pipeline, an enclosure to block undesired nonuniform cooling from airflow, and a moisture-controlled dry box to protect raw materials from moisture intake to improve print quality.

## Mechanical Characterization

### *Tensile Test*

Three different tensile samples were designed to characterize different aspects of the tensile properties of AMFRP composites. Raw filaments were characterized following the ASTM D885 standard for tire cord testing, which was conducted to get baseline pre-processing properties. The highest tensile strength was retrieved with the raw filament,

1377 MPa for the CCF and 816 MPa for HSHTG, compared to the tensile strength provided by the manufacturer datasheet, CCF is 800 MPa and 590 MPa for HSHTG [73].

Testing of the ply level properties for single material lamina was conducted following ASTM D3039 to retrieve the baseline mechanical properties of the three materials used in this research: chopped carbon fiber reinforced polyamide 6, CCF composites, and HSHTG composites. The D3039 samples are dimensioned at 152 x 12.7 x 6.4 mm with the gage length set to 76.2 mm. Both clamping areas of the printed composite were tabbed to avoid clamping failure. ASTM D638A samples were designed, manufactured, and tested to find a correlation between reinforcing strategies and performance. A sample dimension of 165 x 19 x 6 mm was chosen, with the gauge length set to 57 mm. An MTS 810 system was used for both tensile sample types. A crosshead rate of 1 mm/min is prescribed for testing, and three specimens were tested for each configuration.

#### *Single-lap Joint Test*

SLJ-style samples were manufactured using an adapted geometry from ASTM D5868, the standard test method for lap shear adhesion for fiber-reinforced plastic bonding, to evaluate the bonding quality on the AMFRP interfaces. Both ends were printed with built-in tabbing materials to avoid clamping failure. The dimensions were chosen to be 158.8 mm x 12.7 mm x 6 mm, with an overlapping area of 6.4 mm x 12.7 mm. Tests were conducted on an MTS 810 system using a crosshead rate of 2 mm/min, and three specimens were tested for each designed configuration.

### *Mode I Fracture Toughness Test*

Double cantilever beam (DCB) samples were manufactured based on ASTM D5528 - mode I interlaminar fracture toughness of unidirectional FRP composites. The samples underwent a preload-unload cycle to reach the initial crack length desired before the tests. Two sets of moving microscopies were used to record the crack propagation length, and another camera to synchronize the acquired data. An Inston 1331 testing machine was used for testing with a 2 mm/min crosshead rate, and three specimens were tested for each configuration.

A new method was developed to create the precrack required for DCB samples. The method is described in more detail in the third study.

### *Flexural Test*

Flexural samples were fabricated according to ASTM D790 Procedure A to characterize the flexural responses. Specimens were configured with various FVFs, types of reinforcement, and fiber orientations. The specified dimensions of the flexural specimen are 12.7 x 40 x 2 mm with a span-to-depth ratio of 17.5:1, complying with the standard required minimum. An Inston 1331 testing machine was used to test the samples at a 1 mm/min crosshead rate, and three specimens were tested for each configuration.

## Materials Characterization

### *Microscopy Analysis*

The analysis was carried out with microscopy characterization using a light microscope. Microstructural analysis was performed on samples' fracture surfaces, fiber-matrix compositions, and void analysis. Microstructural analysis samples were produced with epoxy matrix impregnation and then polished with 50-100-200-400-800-1200 grid sandpaper, followed by a final polish using 5  $\mu\text{m}$  alumina particles. Void analysis was done using ImageJ software, which utilizes histogram equalization, filtering, thresholding, and binarization of the constituents for removal and image sharpening for counting proportionality.

### *Fractography Analysis*

Fracture surfaces of the tested samples were preserved for observation under light microscopy to find a correlation to failure mode. Fractography on the fiber-matrix interaction was observed under a light microscope and a Keyence KHX 6000 microscope. The microscopic images showcase the failure mechanics for the entire fracture surface. The Keyence microscope is equipped with three-dimensional stitching to provide additional depth of view for analysis with high-resolution images.

## Finite Element Analysis for Verification

Finite element analysis is a technique to implement empirically obtained material properties data into appropriately scaled representative volume element (RVE) to simulate the instantaneous stress field to correlate to physical observations in an equivalent virtual

space. The incidents of interest for material responses on objects undergoing specified boundary conditions can be considered a level five in the technology readiness level (TRL) scale used by the National Astronautics and Space Administration (NASA) for validation [74-76] and is a preliminary requirement to advance to prototyping for applications. The effect of microstructural heterogeneity and mesostructural anisotropy in AMFRP composite can be simulated effectively using a multi-scale modeling scheme based on CLT. The synergies of the nonlinearity of AM objects and the effect of each constituent within FRP composite materials are understudied as factors of internal interaction that can complicate the prediction of the mechanical responses.

The digitized workflow of AM manufacturing is a natural fit for numerical simulation using finite element analysis built with meshed elements. The constituting material models, such as phenomenological observations and mechanical behaviors, can be empirically determined and implemented, accompanying the mechanical models implemented using the finite element analysis software. Once the material properties were retrieved, the model underwent meshing and applied boundary conditions to solve for the structural deformation to evaluate the performance by the resulting stress and strain field. Modeling composite materials and their mechanical responses can sometimes be inaccurate if used only at the component's scale to account for the decohesion phenomenon across different length scales. Therefore, a popular multi-scale approach [77] with differentiating simplifications in different scales to account for the topographical characteristics of the object of interest was used.

The study investigates the mechanical responses of a multi-material system composed of orthotropic and elastic-plastic material properties. Each FEA model was designed

with a ply-wise homogenization process to reflect the AMFRP structure's anisotropy and layer-by-layer nature. Convergence studies were conducted to achieve high-fidelity prediction using a built-in Newton-Raphson method in the ANSYS software.

ASSESSMENT OF FIBER REINFORCEMENT STRATEGIES FOR ADDITIVELY  
MANUFACTURED THERMOPLASTIC COMPOSITES USING MECHANICAL  
TESTING AND FINITE ELEMENT ANALYSIS

by

YU-CHAO SHIH, YONGZHE YAN, MAHMOUD MOHAMED, SUBHAYU SEN,  
SELVUM PILLAY, AND HAIBIN NING

*Progress in Additive Manufacturing* 2024

Copyright

2024

by

Springer Nature Switzerland AG

Used by permission.

Format adapted for dissertation.



## ABSTRACT

Additive manufacturing (AM) for fiber-reinforced plastic (FRP) composites are gaining increasing opportunities in small batch parts designed for aviation applications for their high specific strength, freedom of tailorable properties, creep resistance, and accessibility. The fused filament fabrication (FFF) production suites of 3D-printed FRP composites are commercially available, easily operable, and mechanically simple to provide close-proximity manufacturing of parts-in-need. Experimental verification of properties can be made selective and cost-effective when accompanied by validated predictive capabilities. This becomes even more relevant when considering 3D-printed parts on demand for in-space manufacturing and space exploration. The results reported here were supported by a NASA program to develop that comprehensive approach.

The research aims are two-fold – to deliver performance-centric strategies for AM design made by continuous and discontinuous FRP and the validation technique for such strategies by finite element analysis (FEA) simulation. The numerical modeling based on FEA was developed in conjunction with materials properties made available from experiments and literature. A rate-dependent plasticity model for additively manufactured short fiber reinforced composites and an orthotropic material model for continuous fiber-reinforced composites were implemented. Reinforcing strategies were developed to test the effectiveness of each fiber pattern and layout. Tensile specimens were configured, fabricated, and tested to generate experimental data to evaluate the strategies. The feasibility of the modeling approach in predicting mechanical performances was examined by comparing the simulated and empirical results. The procedure would help validate in-field

3D-printed components where mechanical tests might be limited or inaccessible, as in the case of space exploration.

## INTRODUCTION

Additive manufacturing (AM) is a trending technology featuring a compact and capable machine to deliver engineering components efficiently [1]. AM is a layer-by-layer procedure in which objects are fabricated using a raster algorithm to deposit, cure, or sinter a deposited material. The manufacturing procedure finds its applications predominantly in medical [2,3], transportation [4-6], and aeronautic applications [7] for delivering high-quality parts in small volumes at a reasonable cost. Extrusion-based AM has a growing market value for its simplicity of the equipment, a vast selection of possible feedstock, and a competitive precision level. Near-net-shape manufacturing of functional engineering components is available with high precision using material extrusion (ME) additive manufacturing methods [1,8] in conjunction with post-processing techniques [9,10]. Thermoplastic is a class of material commonly used in extrusion AM [1] as feedstock. However, the mediocre performance of neat thermoplastic has been the major drawback to gaining widespread applications for aerospace components [11,12]. High-strength continuous fiber reinforcement can be used alongside polymer extrusion additive manufacturing to manufacture continuous fiber-reinforced plastic (CFRP) composite [13]. CFRP offers a desirable combination of mechanical properties and environmental resistance, combining the strength and stiffness of highly aligned fiber materials and a protective polymer matrix [14,15].

An array of test procedures are discussed in the literature to characterize the mechanical properties of 3D-printed composites, including fixtures and protocol of quasi-indentation [16], tensile and flexural [16-18], in-plane shear [19], impact and fracture properties [19-21], and interlaminar shear strength (ILSS) [22-24]. The reported data shows a general trend of increasing performance with higher fiber content. However, the selection of printing parameters varies widely depending on the specific requirements, materials, and equipment involved. The challenges to model the material response were discussed in [1], which also complicates predicting the quality and properties of the product. The condition of the outlets limits the quality of each extrusion by the raster movement, affecting the resolution, roughness, and accuracy [8] of the parts by pressure drop, feed control, and thermal stresses. The integrity of the components is determined by the bonding quality and systematic defects accumulated during the printing process [24], resulting in a fundamentally anisotropic state that could affect the structural cohesion to resist catastrophic failure. Some efforts to model and formulate constitutive material failure were proposed and summarized in [25,26]. Unlike elastic-plastic responses in most continua, the debate on failure criterion on FRP composites is an ongoing research area [27] that mainly works in practicality rather than physical principles. The state-of-the-art failure assessment models on highly anisotropic composite design lie somewhere between a criteria-based analysis [26], a probabilistic failure [28,29], or a zone-based [30] analysis since the empirically-acquired maximum stress and strain would only be reliable to some extent [31].

In light of reducing the redundant testing to assess performance on specific parameters, various modeling schemes have been proposed to predict the mechanical behavior of AM CFRP. The work of Melenka [32] is one of the earlier adoptions of the laminated

theorem to predict elastic properties in a mesoscopic sense for AM composites. Rule-of-mixture (ROM) and volume average stiffness (VAS) were used to approximate the bulk materials constant by the comprising composition. The simplicity of these micromechanical approximations enables several adaptations [33-36] for volumetric analysis on a set of semi-homogeneous continuums based on walls, infills, and sandwich laminae, for which the stiffness matrices can be populated by proportionality of constituents. The analytical methods can be an entry point to rule out unfit configurations by using micromechanics to predict materials constant. Polyzos [37] evaluated the elastic properties of 3D-printed composites with multi-scale analytical models, considering the effect of fiber volume fraction (FVF), bridging, and voids. The model is limited to linear behavior, assuming linear elasticity until brittle failure. Wang et al. [38] implemented the degree of fiber wettability and misalignment in their micromechanical model to predict modulus for AM-made carbon fiber reinforced plastic (CFRP). An 8% error margin for CFRP with up to 10% FVF is achieved for linear elasticity. Lupone et al. [39] evaluate the AM CFRP with classical laminated theorem (CLT), ROM, VAS, and microscopy analysis. Tensile properties can be predicted conservatively with VAS and CLT, which is applicable to the configurations of [0/90], [0/60/120], and other quasi-isotropic layups. Saeed et al. [22] utilize an ASTM D3039-inspired tabbing method on an ASTM D638 dogbone specimen made of AM FRP to characterize and model the tensile properties. A positive correlation was established for modulus retrieved analytically and empirically, assuming perfectly bonded interfaces and a state of plane stress [22]. Readers are referred to [8,39,40] for a review of modeling techniques in AMFRP.

Integration of analytical micromechanics in conjunction with simulation is valuable in validating aeronautic flightworthiness according to the technology readiness level (TRL) scale [41]. The robustness of FEA as a numerical modeling tool enables scaling up the complexity of the analyzed system in a simulated environment. A review of available FEA methods in modeling composite material can be found in [42]. Representative volume element (RVE) is a popular tool to model the AM construct with repetitive basic volume cells based on the materials' morphology [43,44]. Methods were proposed in using FEA to model nonlinear plasticity with flow rule [45], rate-dependent viscoplasticity [46], and multilinear extrapolation [47]. Bhandari et al. simulated the short carbon fiber-reinforced acrylonitrile butadiene styrene (SCF-ABS) composites, comparing RVE equipped with the formulation of elastoplasticity, Hill's criterion, and linear elasticity [48]. It was determined that Hill's criterion is suitable for predicting tensile failure on the printed contour, and a bimodular approximation can replicate the stress-strain responses on said composites effectively. Fu et al. [49] applied a mesoscopic RVE method in numerical simulation to model the nonlinear mechanical behavior of 3D-printed short carbon fiber-reinforced polyetheretherketone (SCF-PEEK) composites. Components were disseminated to become representative unified unit cells with several fracture criteria applied to capture failure. The method is based on morphological details of the specific material, and they concluded that the interlaminar failure is of major concern for 3D-printed SCF-PEEK composites. Polyzos [50] proposed a contour-stochastic-based RVE model using fiber and matrix morphologies to simulate a composite material of chopped carbon fiber reinforced polyamide matrix with continuous carbon fiber reinforcement. Although RVE can be a high-fidelity method on the linearly elastic behavior of composites, it is not deterministic for the scalability of models

after implementation at a component level [51]. The simulation of nonlinear responses of laminated composites [52] using RVE based on morphological information can also be difficult.

Although AM FRP composite materials have been available for some time, a systematic approach to evaluating and simulating the performance of reinforcing strategies is lacking. The fiber volume fraction does not always improve the mechanical properties proportionally, especially when various failure mechanisms can be in play regarding the contour of functional parts. The progressive damage of the matrix structure can result in nonlinear responses comprised of elastic-plastic transition caused by stages of decohesion. The scalability of the RVEs and stochastic-based elements to model a megastructure can be tricky and computationally inaccessible. Compared to multi-scale RVE, a laminated approach provides an economical resolution to evaluating

essential properties without compromising robustness. In this study, strategies of fiber reinforcement are evaluated with mechanical tests and compared to numerical predictions to find a correlation. Numerical simulation adopting the laminae simulation approach for 3D-printed composites can simplify the validation of the 3D-printed FRP composites part. The research aims to mimic the reinforcement strategies that could be implemented in engineering components with a combined fiber reinforcement of concentric, quasi-isotropic, and unidirectional layups. The tensile behavior of continuous fiber-reinforced thermoplastic composites is simulated with a rate-independent plasticity model. The tensile modulus on each configuration was compared between those determined by mechanical testing and from the simulated representative laminated structure. A pseudo-secant strain

limit is implemented to predict tensile strength. This research derived a methodology to simplify the validation route without sacrificing safety and freedom of design.

## MATERIALS AND METHOD

### Materials and Equipment

In this study, test coupons were 3D printed using a desktop material extrusion 3D printer, the Mark Two (Markforged Inc., MA, USA). A polyamide-based filament, trade-name Onyx®, was used as the matrix material of the 3D-printed composites. Two variants of continuous fiber filament were used as reinforcement: continuous carbon fiber (CCF) and high-strength-high-temperature glass fiber (HSHTG) filament. The fiber nozzle is equipped with a flattened ironing outlet and a cutting utility to accommodate the deposition of continuous fiber. Some specifications of the machine and the materials are listed in **Table 1**.

Table 1. Selected specifications and parameters for Mark Two 3D printer, Onyx, CCF, and HSHTG.

	Description	Nozzle dia.	Materials Specification	Layer height (Thickness)
Nozzle 1	Plastic nozzle for extrusion of matrix materials	0.4mm	Onyx: $E_T = 2.4 \text{ GPa}$ $\rho = 1.2 \text{ g/cm}^3$	0.1 mm, 0.125 mm, 0.2 mm (Options available for matrix-only prints)
Nozzle 2	Fiber nozzle for extrusion of continuous fiber filament	0.1mm	CCF: $E_T = 60 \text{ GPa}$ $\rho = 1.4 \text{ g/cm}^3$ HSHTG: $E_T = 21 \text{ GPa}$ $\rho = 1.5 \text{ g/cm}^3$	CCF: 0.125mm, HSHTG: 0.1mm (Not customizable, constraint by feedstock/machine dimension)
<p>* Manufacturer: Markforged Inc. (MA, USA) for the Mark Two 3D printer and all three filaments (Onyx, CCF, HSHTG)</p> <p>* Printer specification: Preset print speed, bed enclosure, filament dry box, Bowden tube + T-belt drive</p> <p>* Print Temperature: Preset, ~270-273°C for Onyx, CCF, HSHTG</p>				

Onyx® is a proprietary polyamide copolymer blend with an unknown amount of caprolactam and 10-20% chopped carbon fiber, based on the materials safety data sheet provided by the company [53]. Judging from the caprolactam presented, it is likely a blend of polyamide 6. The term “continuous fiber filament” used in the study refers to a kind of filament feedstock composed of yarns of continuous fiber impregnated with a thermoplastic matrix. The term “matrix” will be referred to as the Onyx matrix in the printed sample. The machine utilizes a dual-extrusion system; each nozzle is specifically designed to deposit the matrix or continuous fiber filament. Both filaments are composed of an outermost thermoplastic matrix and pre-impregnated continuous fiber reinforcement for processibility. The purposes of the designed configurations were in the result and discussion section. The model was created with Solidworks 2022R1 to include sectional details of different fiber-matrix compositions and subsequently loaded into the Eiger slicer software to generate the printing toolpath.

### Materials Characterization

Lower-than-expected mechanical properties [54] can be a result of voids introduced by the printing process. Therefore, microscopy analysis was done to quantify the void content using a set of dummy samples made of Onyx and continuous carbon filament with 100% infill. CCF and HSHTG filaments were also analyzed to understand the composition by measurement of fiber content, fiber size, and filament diameter. FVF of HSHTG filament was double-checked using a burn-off test in the air. Samples were carefully mounted in epoxy resin, followed by grinding and polishing on sandpaper from grid 80-120-180-240-400-600-800-1200 and imaged with a light microscope. All microscopic samples were imaged in the cross-sectional area perpendicular to the printed lamina surfaces, and the



acquired images were processed with ImageJ FiJi [55] software with contrast enhancement, edge sharpening, and binarization operations to obtain measurable pixels and a calibrated conversion to standard units. The robustness of the result was checked by comparing the void content characterized using density measurements following ASTM D2734 - Void Content of Reinforced Plastics [56]. The density was measured by the ASTM D792- Standard Test Methods for Density and Specific Gravity of Plastics by Displacement [57] procedures, with a Pioneer™ PX84 analytical balance (Ohaus, NJ, USA). Available data in the literature [58] were also compared and summarized. Baseline tensile properties for two types of CFRP samples were characterized with a series of tensile tests using a geometry adopted from ASTM D3039 [59], which is a rectangular beam with a dimension of 152 x 12.7 x 6.4 mm. A glass fiber-epoxy tabbing material was bonded to the sample clamp area to avoid stress concentration, according to ASTM D3039 suggestion. An MTS 810 testing system equipped with a 2 kN load cell was used for all tensile tests. Nearly 100% CCF and 100% HSHTG specimens were achieved by using an inserted pause after the floor matrix layer was completed. A thin FreeKote 770-NC mold release layer was applied using a laboratory wipe before resuming the printing of the continuous fiber layers. The floor layer and the walls were removed after the print was finished, and samples were subsequently tested.

### Sample Configurations

Reinforcing strategies were established with chosen fiber layup and materials in-fill using the Eiger cloud slicing system to determine their feasibility in practicality. Four objectives are specified in **Table 2**. The sample designations using A-E labels are specified in the Result section for clarity and ease of discussion. The purpose of the strategies

was two-fold – provide an assessment of specific reinforcing scenarios and the validity of the modeling method for validating such strategies. All solid infill Onyx are printed with an alternate 45°/-45° rectilinear infill.

Table 2. Designed reinforcing strategies set for ASTM D638 Type I sample configurations.

Set	Purpose	Description	Sample
M1	Baseline properties on short FRP with 100% rectilinear and 50% triangular infill.	Infill - 50% / 100%   Wall - 4 (1.6 mm) Infill Pattern - Triangular / Rectilinear	A1 - 50% A2 - 100%
M2	Synergistic effect for concentric CCF/HSHTG fiber rings CFRP with 50%/100% infill.	Infill - 50% / 100%   Wall - 4 (1.6 mm) Infill pattern - 6 concentric rings for 8/16/40 (CCF) and 8/16/52 (HSHTG) layers	B1, B2, B3-CCF C1, C2, C3-HSHTG
N1	Maximum available continuous fiber in unidirectional direction CFRP.	Infill - 100%   Wall - 2 (0.8 mm) Infill pattern - Unidirectional	A3-CF_Uni A4-HSHTG_Uni
N2	Reinforcing effectiveness on different CFRP walls on short FRP matrix.	Infill - 100%   Wall - 2 (0.8 mm) Infill pattern - Sandwich / Box / Perimeter	D1, D2, D3-CCF E1, E2, E3-HSHTG
Note: A gapping 100%-infilled layer between the triangular-50 and the continuous fiber			

Set M1 and M2 samples include a 50% triangular infill and 100% infill percentage, combined without or with continuous reinforcement, respectively. The M2 samples were configured with multiple concentric walls to evaluate the effect of an all-around reinforcing fiber shell on an engineering design anticipated to behave as described by the literature [60]. M samples have four enclosing bottom/top layers parallel to the print bed direction and 1.6 mm thick perpendicular walls. In opposition, two enclosing layers on the bottom/top and 0.8 mm thick perpendicular walls were configured for N samples. All configurations for varying fiber infill patterns are also illustrated in **Figure 1**. Subgroup A

also serves to validate the material properties input for all simulations. The white, gray, black, and yellow blocks represent the artificial triangular prism voids, Onyx matrix, CCF filament, and HSHTG filament.

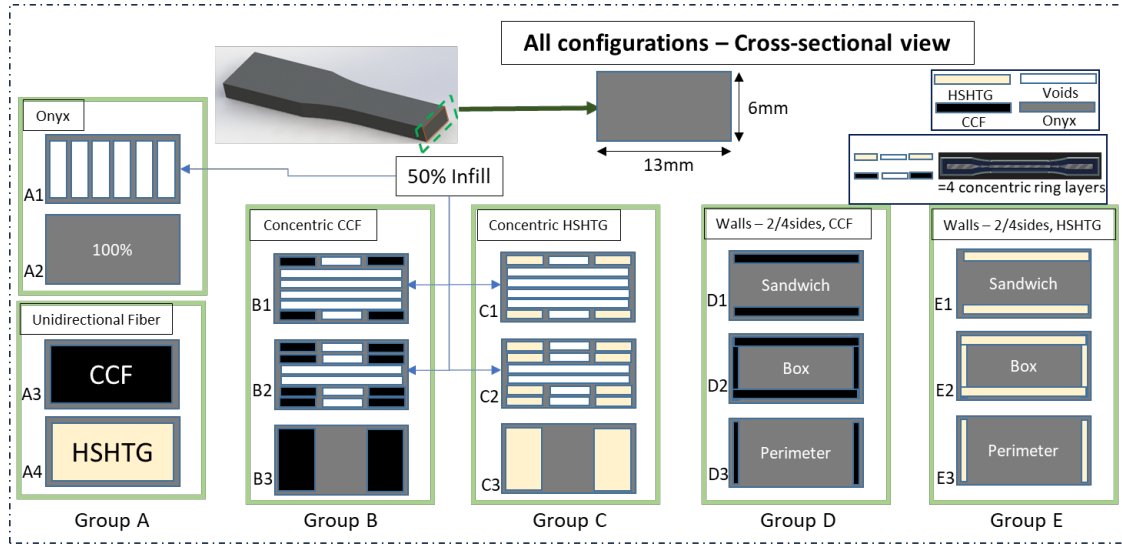


Figure 1. Reinforcement strategies on each configured specimen's group.

### Mechanical Test

The ASTM D638 [61] Type I “dogbone” specimens were adopted for evaluation of performance. The solid model was made with Solidworks, configured in Eiger, printed with the Mark Two printer, and tested. The contour and dimensional detail are illustrated in **Figure 2**. Three specimens were tested for each configuration, following ASTM D638 procedures; load, displacement, and strain were recorded using MTS-810 with a clipped-on extensometer. A displacement rate of 1 mm/min was prescribed until failure. Mechanical test results are compiled to assess the reinforcing effectiveness, including tensile modulus, failure strength, and strain at failure. The data was analyzed, compiled, and compared with analytical and numerical predictions. Failure mode was also analyzed to understand the weakness of each configuration.

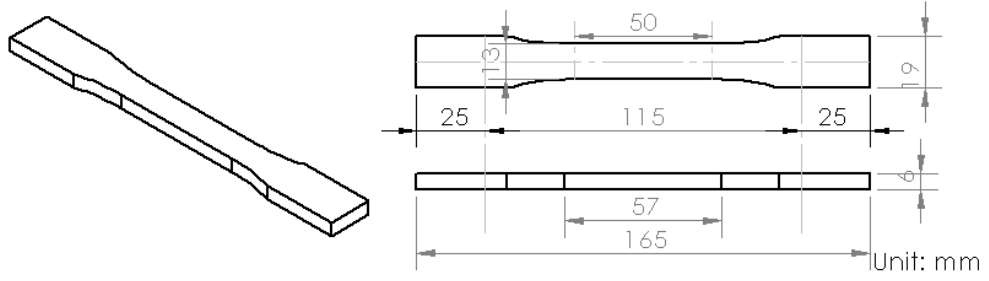


Figure 2. Engineering drawing and dimension of the tensile specimen.

### Finite Element Analysis

FEA simulation was configured and run with ANSYS Professional 2022R1. The solution was generated by ANSYS Mechanical APDL using a high-performance computing cluster, the Cheaha supercomputer. A homogeneous brick element was generated using ANSYS Composites PrePost (ACP) to implement nonlinear in-plane quasi-isotropic properties on Onyx® and orthotropic material properties on CCF and HSHTG [62], which also account for the off-axis fiber correction. The complete workflow is summarized in **Figure 3a**. A strain-and-stress continuum damage model was used to capture the multi-stage decohesion of Onyx layers regarding the systematic defects implemented by the printing process [63]. Three boundary conditions were applied on both ends and at the x-z surfaces, as shown in **Figure 3b**. **Figure 3c** shows an example of a perspective view of sample B1. The halved model was configured along with non-penetrative boundary conditions on the X-Z surface, as shown in **Figure 3b**, to conserve computing power. A pseudo-time-stepped tensile displacement was applied on one end with eight steps and 200 sub-steps to account for the effect of distortion on the mechanical responses. Materials properties were derived empirically and used in a plate element simulation, coupling with some value adopted from Iragi's [19] work. The major theme of the bulk behavior

was assumed to have a matrix-dominant multilinear elastic behavior for Onyx samples and a fiber-dominant linear elastic behavior for CFRP samples. Two simplifications were implemented to resolve the unconvergence issue caused by discontinuity: removal of the Onyx wall near both ends where boundary conditions were applied and simplification of the triangular unfilled area with infilled Onyx volume. The fill-up theme was only applied to B1, B2, C1, and C2, where fiber-dominant linear elasticity is expected.

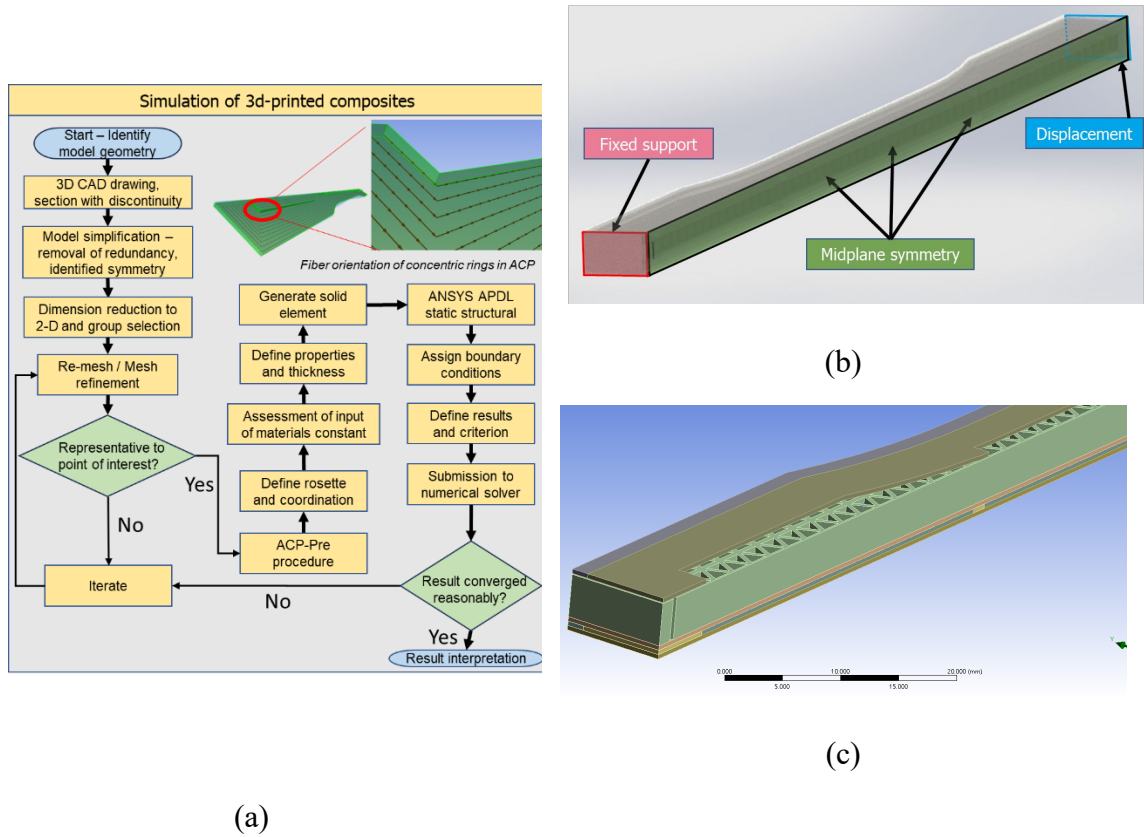


Figure 3. (a) Complete workflow to simulate 3d-printed composites using ANSYS (b) Boundary conditions applied in the numerical model, (c) Perspective view - the half model for CF-50-8.

The failure strength was estimated using a maximum longitudinal strain approximation:

$$\sigma_{sim} = \varepsilon_{est} * E_{sim} \quad (1)$$

where  $E_{sim}$  is the simulated modulus,  $\sigma_{sim}$  is the predicted strength,  $\varepsilon_{est}$  is the secant strain at failure calculated from linear extrapolation of the experimental data, using:

$$\varepsilon_{est} = \frac{\sigma_e}{E_e} \quad (2)$$

for which  $E_e$  and  $\sigma_e$  are modulus and failure stress from the experiment, respectively. A representative mesh size of 0.6 mm was chosen for most of the models, and a 0.2 mm refinement was configured on each triangular layer. The selection is based on a series of convergence studies and sufficient resolution on walls and triangular infills.

## RESULT AND DISCUSSION

### Materials Characterization

The density measurements regarding the ASTM D792 procedure show a density value of 1.11 g/cm<sup>3</sup> for Onyx material, using a 100% infill 15x15x5 mm block Onyx specimen. The direct comparison between the characterized density and the manufacturer data shows a void content of around 7.6%. **Figure 4** shows the images of the three types of characterized filament after enhancement by ImageJ software. The fiber volume fraction (FVF) results for all continuous filaments are listed in **Table 3**, along with some reference values from the literature for comparison. No FVF value was calculated for Onyx with image processing because of optical noise caused by fiber misalignment and voids from fiber pullout.

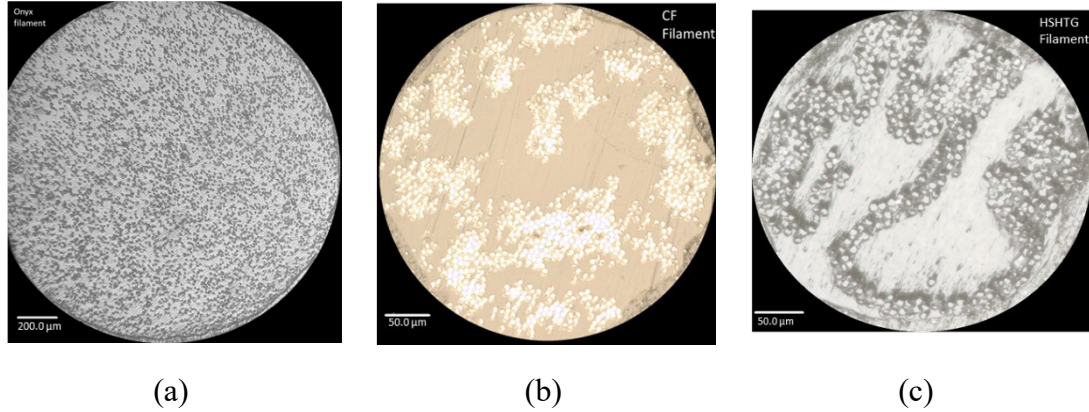


Figure 4. Cross-sectional microscopic images for fiber characteristics measurement of (a) Onyx filament, (b) CCF filament, (c) HSHTG filament.

Table 3. Fiber volume fraction of the feedstock filament material.

Fiber Character-istics	Methods \ Filament type	Onyx	CCF	HSHTG
<b>Fiber Volume Fraction (FVF)</b>	<b>Digestion</b>	10.9% <sup>(A)</sup>	33.9% <sup>(A)</sup>	30.6% <sup>(A)</sup>
	<b>Pyrolysis</b>	11% <sup>(A)</sup>	36% <sup>(A)</sup>	31% <sup>(A)</sup> , 27% <sup>(B)</sup>
	<b>Microscope</b>	-	27% <sup>(B)</sup>	27% <sup>(B)</sup>
	<b>TGA</b>	9.6% <sup>(A)</sup>	36.4% <sup>(A)</sup>	27.3% <sup>(A)</sup>
	<b>Evaporation</b>	-	34.5% <sup>(C)</sup>	-
<b>Fiber Dia.</b>	<b>Microscope</b>	-	5.8±0.2μm <sup>(B)</sup>	8±0.2 μm <sup>(B)</sup>
<b>Fiber count</b>	<b>Microscope</b>	-	1000 <sup>(B)</sup>	500 <sup>(B)</sup>
<b>Filament Dia.</b>	<b>Microscope</b>		375±2.6μm <sup>(B)</sup>	312±17μm <sup>(B)</sup>
Note: <sup>(A)</sup> : Data from [58], <sup>(B)</sup> : Data from analysis of this study, <sup>(C)</sup> : Data from [64]				

Void content was measured using a similar microstructural analysis methodology for printed Onyx-CCF samples, and the processed images are shown in **Figure 5**. Sections were selected from microscopy images of different magnifications and from different laminae combinations to calculate a void percentage in a statistical sense. Each image would include 2-3 printed layers to get a representative void content within the 3D-printed FRP. Images underwent proper edge sharpening, thresholding, and binarization to compute the compositional percentage for voids and non-void regions. The resulting void

content of  $6.52\% \pm 0.71\%$  shows a good correlation to the 7.6% from density measurement and the 7.5% reported in the literature [19]. It is observed that regardless of adsorption, density measurement on 3D printed composites using ASTM D2734 gives a close estimation of its density. Base lamina properties of the bulk filament (CCF, HSHTG) were characterized using the ASTM D3039 standard test method for tensile properties, as reported in previous work [24]. The results are shown in **Table 5**. The transverse properties of each continuous fiber filament were estimated by a ten-percent rule from [65], which takes one-tenth of the longitudinal properties for transversal direction.

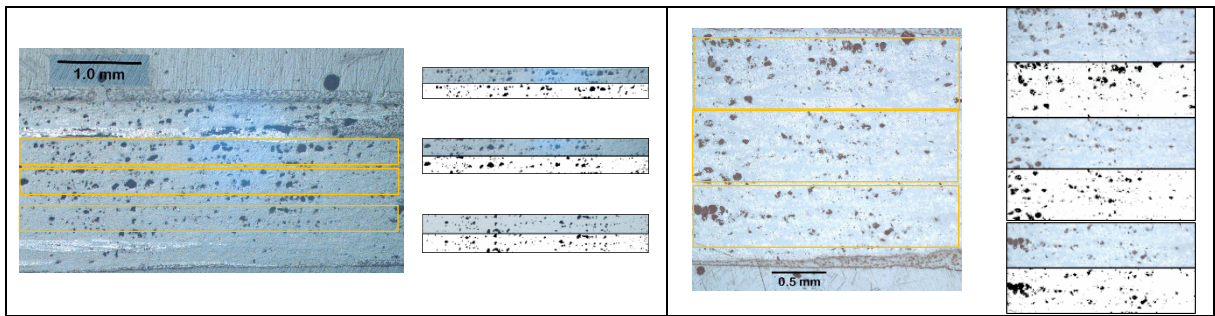


Figure 5. Cross-sectional images of printed CFRP specimen.

### Mechanical Test Result

This section discusses the mechanical testing data from the aforementioned reinforcing strategies. For ease of reading results, the detailed parameters for all configurations are listed in **Table 4**.

Table 4. Detailed configurations for all reinforcing strategies.

Configura- tion	Infill	Layer height (mm)	Reinforcement			Wall Thick- ness (mm) (Count x 0.4 mm)
			Type	# of cont- F Layer	Infill / Layout	



A1	Onyx-50	50%	0.1	Matrix	0	Triangular	4 x 0.4 = 1.6
A2	Onyx-100	100%	0.1	Matrix	0	Alternate 45°-135°	4 x 0.4 = 1.6
A3	CF-Uni	100%	0.125	CCF	44	Uni 0°	2 x 0.4 = 0.8
A4	HSHTG-Uni	100%	0.1	HSHTG	56	Uni 0°	2 x 0.4 = 0.8
B1	CF-50-8	50%	0.125	CCF	8	Six concentric rings	4 x 0.4 = 1.6
B2	CF-50-16	50%	0.125	CCF	16	Six concentric rings	4 x 0.4 = 1.6
B3	CF-100-40	100%	0.125	CCF	40	Six concentric rings	4 x 0.4 = 1.6
C1	HSHTG-50-8	50%	0.1	HSHTG	8	Six concentric rings	4 x 0.4 = 1.6
C2	HSHTG-50-16	50%	0.1	HSHTG	16	Six concentric rings	4 x 0.4 = 1.6
C3	HSHTG-100-52	100%	0.1	HSHTG	52	Six concentric rings	4 x 0.4 = 1.6
D1	CF-Sand	100%	0.125	CCF	4	Uni 0° roof/bottom	2 x 0.4 = 0.8
D2	CF-Box	100%	0.125	CCF	44	Uni 0° roof /bottom + Perimeter Wall	2 x 0.4 = 0.8
D3	CF-Peri	100%	0.125	CCF	44	Perimeter Wall	2 x 0.4 = 0.8
E1	HSHTG-Sand	100%	0.1	HSHTG	4	Uni 0° roof /bottom	2 x 0.4 = 0.8
E2	HSHTG-Box	100%	0.1	HSHTG	56	Uni 0° roof/bottom + Perimeter Wall	2 x 0.4 = 0.8
E3	HSHTG-Peri	100%	0.1	HSHTG	56	Perimeter Wall	2 x 0.4 = 0.8

“Matrix”: Onyx only, “CCF”: continuous carbon fiber filament, “HSHTG”: High-strength-high-temperature glass fiber filament, “Triangular”: A 50%-infill pattern with a matrix of triangular prism unfilled area.

“Roof/bottom”: The first/last several layers parallel to the print surface.

“Perimeter wall”: Two enclosing walls aside the outermost contour along the x-z direction.

The materials input for orthotropic fiber filament is listed in **Table 5**. A general trend of proportionality increase in modulus with fiber volume fraction was observed. Error bar was marked for each characterized result to illustrate the variability of the tested data. All available mechanical test results are sorted by material type and in descending fiber

fraction over cross-sectional area order, as presented in **Figure 6** and **Figure 7**. The characterized tensile modulus is listed in descending order as Unidirectional > All concentric layer > 16 concentric layers > 8 concentric layers > box > perimeter wall > sandwich. It is concluded that artificially unfilled volume, along with the use of concentric continuous fiber rings, is an effective strategy to get a high specific modulus, which is proportional to the fiber fraction over the cross-sectional area within the samples' gage regime. The reinforcement strategies push the materials' behavior to fiber-dominant linear elasticity while retaining proper toughness with triangular-infilled matrices.

Table 5. Tensile test results for fiber-only 3D-printed composites for modeling input.

Material	Modulus (GPa)	Strength (MPa)	Transverse E (GPa) (Ten-percent rule) [65]	Reference modulus/strength from datasheet	
CF lamina*	$66.5 \pm 0.7$	$811.0 \pm 18$	6.6	60 GPa	800 MPa
HSHTG lamina	25	670	2.5	21 GPa	600 MPa
* As reported in previous work [24]					

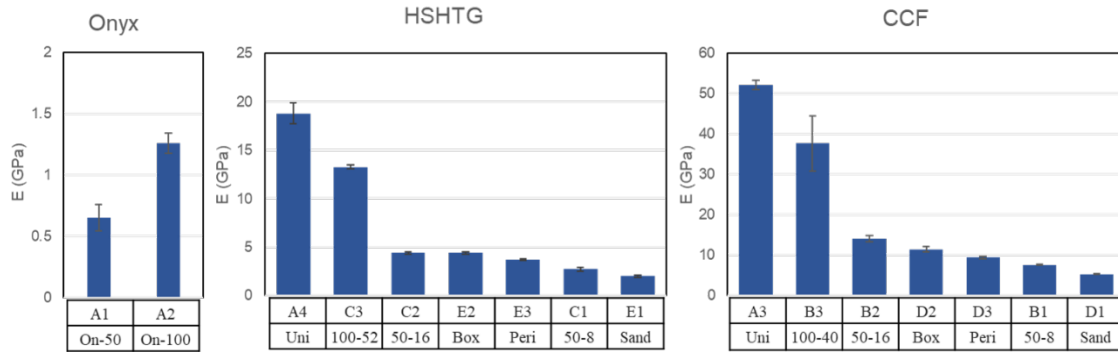


Figure 6. Tensile modulus of tested configurations by order of cross-sectional fiber fraction.

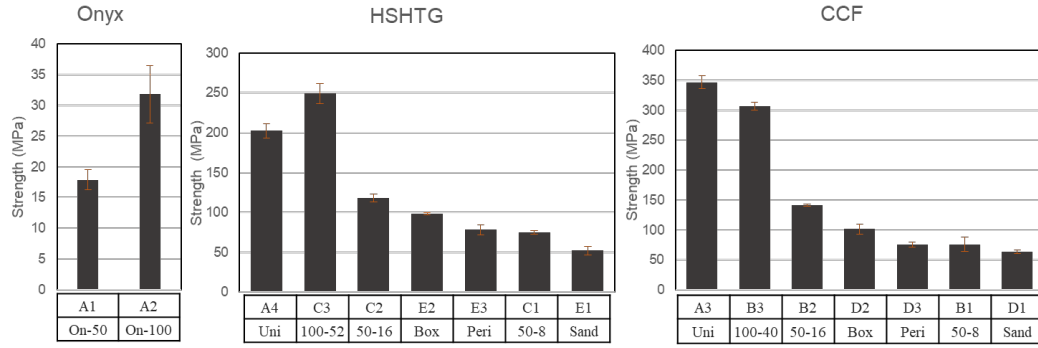


Figure 7. Tensile strength of tested configurations by order of cross-sectional fiber fraction.

The modulus is valid for all configurations as they were calculated within the first 0.1-0.5% strain regime, while the failure strain data were used to predict tensile failure on each configuration. It is worth mentioning that the strength result here does not reflect the actual tensile strength of said configuration in the gage area; instead, it provides an assessment point to evaluate the strengthening strategies on a tapered beam geometry. Concisely, the comparison of all strength data showcases the feasibility of engineering implementation of the strategies when a mixture of failure modes is possible. Elastic-plastic responses were observed in A1 and A2, while linear elastic responses were observed for all other specimens, for which the responses were dominated by continuous fiber reinforcement. A comparison of A1 and A2 shows a 94% and 78% increase in modulus and strength, respectively, comparing 100% infill Onyx to 50% infill Onyx. The effective tangent modulus was calculated and plotted against the total strain for two Onyx-only configurations, as shown in **Figure 8**. Those modulus were used as the modeling inputs. The tangent modulus for empirical A1 and A2 data was calculated for each 80-90 data point, or about 0.15 mm elongation for each data point was recorded at a frequency of 20hz. A consistent reduction of tangent modulus throughout straining was observed and replicated with a multilinear curve fit to

simulate the step-release of the 45/-45 rectilinear infill in the longitudinal direction. The initial modulus of Onyx was homogenized into 1260 MPa as opposed to the modulus of 2400 MPa given by the manufacturer's data [53]. The decohesion between printed layers at a laminae level was successfully replicated with the prescribed multilinear elastoplastic property.

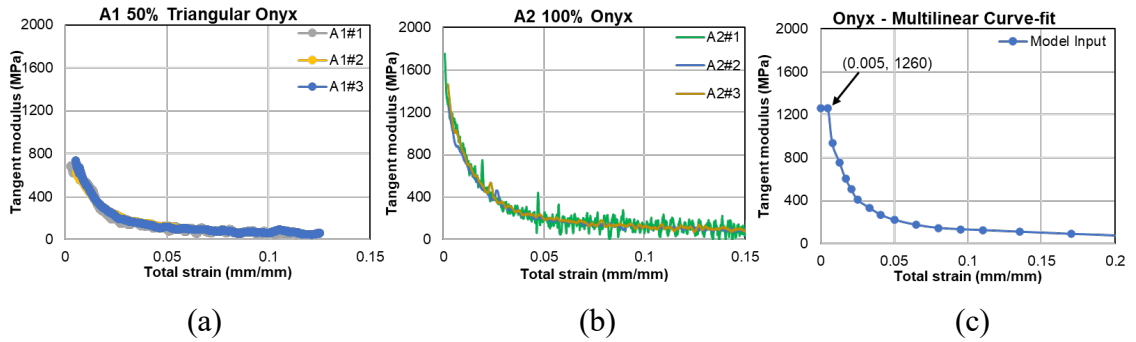


Figure 8. Effective tangent modulus to total strain for (a) A1, (b) A2, and (c) modeling input for Onyx.

Samples A3 and A4 were used to examine the highest-possible achieved reinforcement with maximized fiber content. These reinforcement strategies display the highest modulus, yet not necessarily higher strength, because of the premature failure due to fiber delamination. The failure morphologies of A3 and A4 are summarized in **Figure 9a**. Under the condition that a unidirectionally reinforced fiber was laid along the outermost contour surface, the failure due to interlaminar sliding in the yz-plane was observed due to composite stress of compression, shear, and tensile. **Figure 9b** shows the failure mode of groups B and C, where the slicer effectively generated a wedge-shaped contour to cause premature failure by stress concentration. That the scaling effect [66] on specimens' mechanical performance responses did not increase proportionally was observed and reported in [56]. The result was attributed to the more complex failure mode introduced by

the heterogeneous stress field resulting from higher anisotropy. It is also suspected that the stiffening effect of the fixture would vary by sample configurations. The results in groups D and E show effective fiber reinforcement as a function of fiber volume fraction. Although some modulus and strength increases were evident, the configured profile lacked sufficient fiber layers to achieve the desired mechanical performance. Those are a direct manifestation of the weaknesses of those reinforcing strategies to emphasize the outermost shell reinforcement on an irregularly shaped object. The result also shows a 20% lower tensile strength than expected results from irregularly turned fiber angles that would induce additional weaknesses.

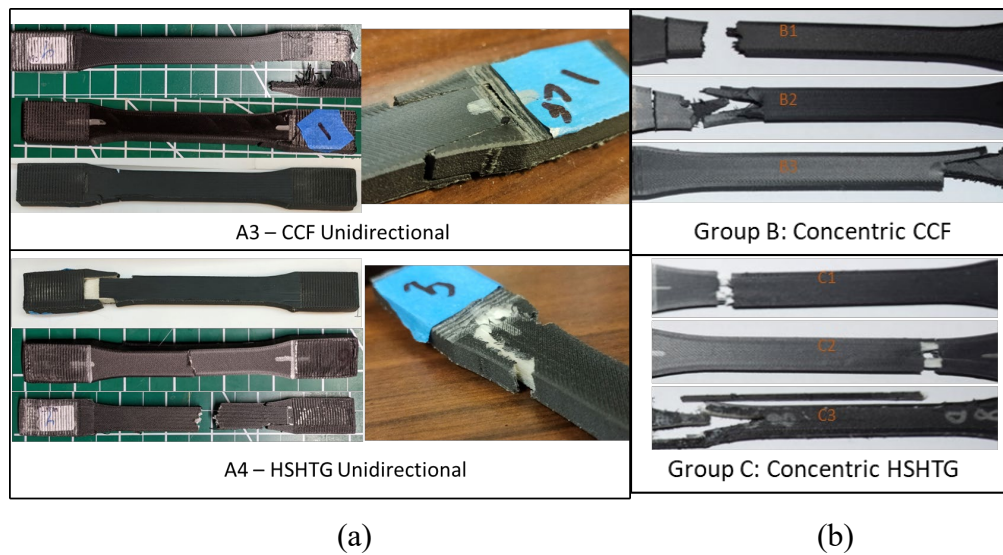


Figure 9. (a) Delamination over the x-z surfaces for samples A3 and A4 (b) Wedge failure over the neck-gauge region on group B and C samples.

B3 and C3 configuration with 16 concentric rings/50% infill shows a desirable modulus performance as they are at least 10% lighter than group D and E configurations and display as much as a 6-fold modulus compared to the sandwich configuration. However, lower-than-expected strength was also observed on B3/C3 due to delamination failure between the off-axis fiber and the matrix. The highest error margin was also observed

for configuration B3 with 40 layers of thick concentric walls, resulting from the property discontinuity of the same fiber-matrix interfaces. Accounting for various failure modes over the entire geometry is recommended when using a concentric reinforcement over a non-trivial geometry. Other recommendations to achieve optimal desirable performance are using enough fiber reinforcement and keeping the slicer away from creating anomaly discontinuities. The geometry should be adapted to fit the fiber reinforcement profile to avoid delamination-type failure. An additional strain limit regarding the product with lower fiber reinforcement and infill percentage was plotted in **Figure 10**, with fiber fraction corrected by the filament's FVF provided in the previous materials characterization section. Higher strength can be achieved with a higher fiber fraction while compromising the failure strain of the component. Even though the 3D-printed mesostructure allows the stagewise decohesion on the structural hierarchy, the irreversible yielding at a much lower stress level might not be as desirable.

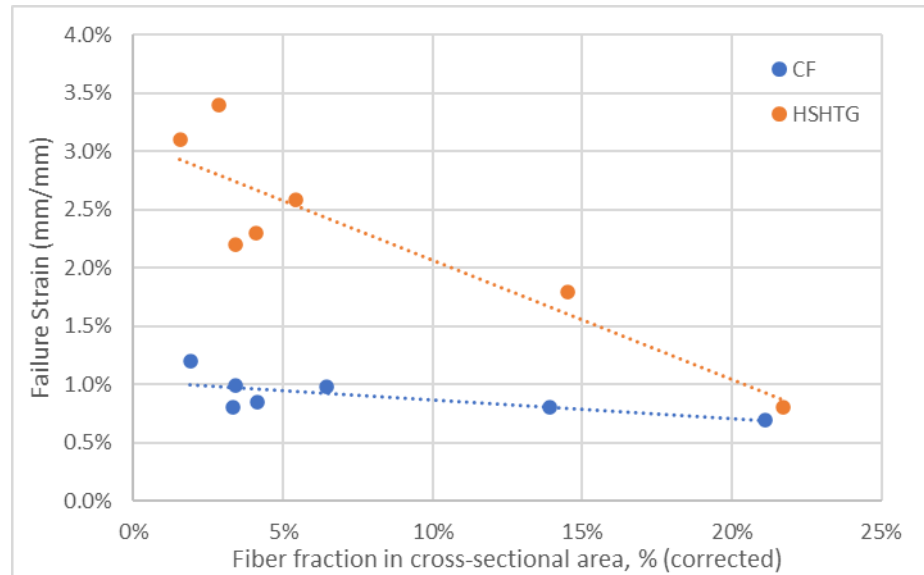


Figure 10. Corrected cross-sectional fiber fraction to failure strain for all specimens.

### Comparison of Modeling and Characterized Results.

A comparison of all groups between mechanical tests and FEA simulation is shown in **Figure 11**. A reasonably close correlation to the mechanical results of less than 10% was observed for most configurations. All elastic moduli were calculated using the simulated strain and the resulting stress over the gauge area within the 0.1%-0.5% strain range. The competency of the calibrated multilinear elastoplasticity model was shown in the low error margin (<1%) on modulus and strength prediction of A1 and A2 configurations, indicating that this approach can predict mechanical responses of matrix-dominated configurations. **Figure 12** shows the stress-strain responses correlation for A1 and A2. Modulus evolution throughout the straining of A1 and A2 was observed, as mentioned in **Figure 8**. The model captured the decohesion of deposited mesostructured composites, as mentioned in the previous section.

Near linear elasticity was observed in every other simulation result, for which their mechanical behavior is dominated by fiber reinforcement. The A3 and A4 are benchmarked as the input deviation of the materials data, showing a deviation of 1.5% and 10% for CCF and HSHTG, respectively. During the convergence study, shear properties input was found to be insensitive to the resulting tensile responses. A general trend in all series is that a slightly more conservative prediction was observed whenever an off-axis angle ply was present on the contour. A possible reason for this underestimation is the difference in geometrical distortion between the mechanical test and the FEA model caused by the defects in the actual AM samples. During the mechanical test, the fiber along the contoured neck is allowed to be stretched and aligned toward the loading direction by transverse plastic deformation of the matrix core due to defects such as the

embedded voids and loosely bonded interfaces. However, the FEA results were modeled with a continuously bonded interface between the bodies, resulting in a lower degree of freedom, which disallows fiber alignment to the loading direction. Therefore, slightly lower load responses were calculated for the numerical modeling. However, the assumptions here would require more empirical evidence for corroboration in further studies.

The numerically determined modulus for groups B and C, which are concentric CCF and HSHTG reinforcement, shows a -13% / -12% deviation for CCF in B1 and B2 and a -7.7% / -4.5% prediction for HSHTG in C1 and C2. Overall, the numerical model can have a conservative and valid prediction below an error margin of 10% for most configurations.

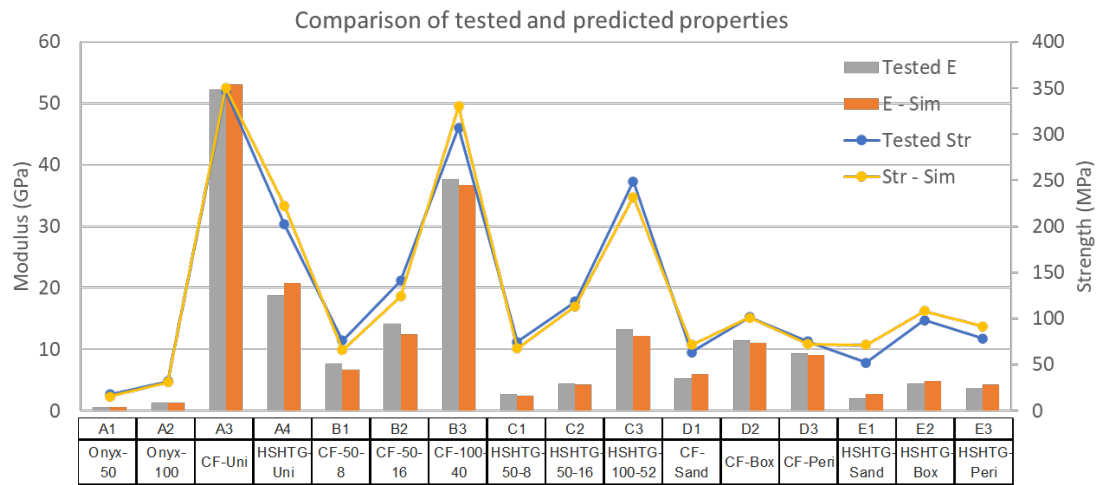


Figure 11. Comparison of empirical results and modeled tensile responses numerically.

Group D and E results show a general trend of overestimation when sandwich reinforcement is present in the model and underestimation when a perimeter wall is used. In cases when the discontinuity brought in by the 3D-printing process is significant due to insufficient fiber reinforcement (<10% continuous filament), the model is incapable of generating a prediction of less than 15% error margin. It is concluded that the current



modeling approach is suitable for two kinds of FRP: one behaves elastic-plastic responses with pure short FRP of  $45^{\circ}/-45^{\circ}$  matrix, and the other behaves near linear elastic with a meaningful amount of continuous reinforcement. Strategy-wise, sufficient continuous reinforcement to achieve linear elasticity is recommended to improve overall structural integrity. Insufficient continuous fiber would only provide minimal reinforcement yet possibly introduce more defects for different failure modes.

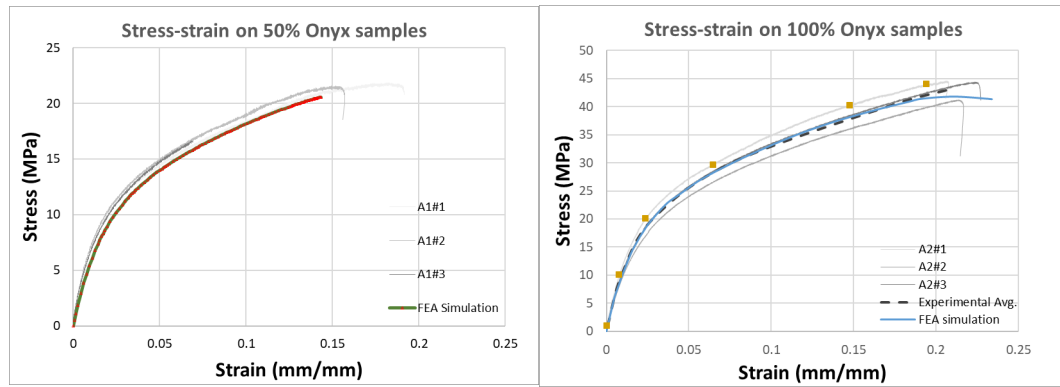


Figure 12. Stress-strain curve of tested and simulated 50%(left) and 100%(right) Onyx data.

## CONCLUSIONS

Theoretically, unidirectional fiber reinforcement can provide the highest performance in tensile loading. However, premature failure on several configurations was observed by delamination on curved areas, debonding of enclosing walls, and decohesion of wedges. In general, this is true whenever an extensive stiffness discontinuity is present. The concentrated stresses within a printed contour can undermine the load-bearing capacity of continuous fiber reinforcement under tensile loading. The configurations with triangular voids embedded have the potential to achieve higher specific modulus, but further investigation is needed to evaluate the corresponding structural integrity.

Tensile responses of all reinforcing strategies were modeled with lamina-based finite element analysis using ANSYS. A low error margin was observed in the model prediction for most reinforcement strategies, showing that the model is competent to give a correlated prediction with implementing material elastoplasticity, orthotropic properties, and contour-based non-linearity. As opposed to the morphological-based representative cell (RC), the homogenization of ACP builds stiffness matrices based on the plate theorem, which is more straightforward, computationally less costly, and equipped with more utility. The scheme is suitable for simple loading where only the monotonic stress is of interest. Results show a generally good correlation for the stress-strain responses on the gauge area. Based on empirical data, the strength prediction was made with a linearly extrapolated secant strain. Although the scheme relies on empirical data acquisition for laminae properties, the model provides an initial evaluation of the modulus and strain for interested strategies. The finite element analysis observed a consistent correlation regarding the material's behavior for the stress-strain relationship. Future work can be done to expand the method by implementing interface elements to account for raster/interfacial discontinuity at a lamina level.

Current results showcase the capability of less than 10% deviation for modulus predicted for most configurations. Reinforcing strategies aim to achieve the most effective fiber reinforcement on layout sequences in a functional part. However, in most practical cases, a thorough investigation of the stress field is challenging to commence during each iteration. This study has demonstrated a simple modeling approach to down-select between numerous additively manufactured composite designs with continuous reinforcements. The methodology can be extremely valuable for resource management by circumventing

redundant empirical verification, entailing printing, and testing numerous design alternatives. This is especially true when testing facilities may not be available, such as outposts in space or forward military facilities.

## REFERENCES

1. A. Gold, S., Strong, R. and N. Turner, B. (2014) A review of melt extrusion additive manufacturing processes: I. Process design and modeling. *Rapid Prototyping Journal*, **20**, 192-204. <https://doi.org/10.1108/rpj-01-2013-0012>.
2. Trachtenberg, J.E., Placone, J.K., Smith, B.T., Fisher, J.P. and Mikos, A.G. (2017) Extrusion-based 3D printing of poly(propylene fumarate) scaffolds with hydroxyapatite gradients. *J Biomater Sci Polym Ed*, **28**, 532-554. <https://doi.org/10.1080/09205063.2017.1286184>.
3. Jockusch, J. and Ozcan, M. (2020) Additive manufacturing of dental polymers: An overview on processes, materials and applications. *Dent Mater J*, **39**, 345-354. <https://doi.org/10.4012/dmj.2019-123>.
4. Leal, R., Barreiros, F.M., Alves, L., Romeiro, F., Vasco, J.C., Santos, M. and Marto, C. (2017) Additive manufacturing tooling for the automotive industry. *The International Journal of Advanced Manufacturing Technology*, **92**, 1671-1676. <https://doi.org/10.1007/s00170-017-0239-8>.
5. Cooper, D., Thornby, J., Blundell, N., Henrys, R., Williams, M.A. and Gibbons, G. (2015) Design and manufacture of high performance hollow engine valves by Additive Layer Manufacturing. *Materials & Design*, **69**, 44-55. <https://doi.org/10.1016/j.matdes.2014.11.017>.
6. Salifu, S., Desai, D., Ogunbiyi, O. and Mwale, K. (2022) Recent development in the additive manufacturing of polymer-based composites for automotive structures—a review. *The International Journal of Advanced Manufacturing Technology*, **119**, 6877-6891. <https://doi.org/10.1007/s00170-021-08569-z>.
7. Gradl, P.R., Greene, S.E., Protz, C., Bullard, B., Buzzell, J., Garcia, C., Wood, J., Osborne, R., Hulka, J. and Cooper, K.G. (2018) Additive Manufacturing of Liquid Rocket Engine Combustion Devices: A Summary of Process Developments and Hot-Fire Testing Results. <https://doi.org/10.2514/6.2018-4625>.
8. Turner, B.N. and Gold, S.A. (2015) A review of melt extrusion additive manufacturing processes: II. Materials, dimensional accuracy, and surface roughness. *Rapid Prototyping Journal*, **21**, 250-261. <https://doi.org/10.1108/rpj-02-2013-0017>.

9. Bahnini, I., Rivette, M., Rechia, A., Siadat, A. and Elmesbahi, A. (2018) Additive manufacturing technology: the status, applications, and prospects. *The International Journal of Advanced Manufacturing Technology*, **97**, 147-161. <https://doi.org/10.1007/s00170-018-1932-y>.
10. Ge, J., Pillay, S. and Ning, H. (2023) Post-Process Treatments for Additive-Manufactured Metallic Structures: A Comprehensive Review. *Journal of Materials Engineering and Performance*, 1-50. <https://doi.org/10.1007/s11665-023-08051-9>.
11. Liu, G., Zhang, X., Chen, X., He, Y., Cheng, L., Huo, M., Yin, J., Hao, F., Chen, S., Wang, P. *et al.* (2021) Additive manufacturing of structural materials. *Materials Science and Engineering: R: Reports*, **145**. <https://doi.org/10.1016/j.mser.2020.100596>.
12. Clausen, A. (2016) PhD Thesis, DTU Mechanical Engineering.
13. van de Werken, N., Tekinalp, H., Khanbolouki, P., Ozcan, S., Williams, A. and Tehrani, M. (2020) Additively manufactured carbon fiber-reinforced composites: State of the art and perspective. *Additive Manufacturing*, **31**, 100962. <https://doi.org/10.1016/j.addma.2019.100962>.
14. Goh, G.D., Yap, Y.L., Agarwala, S. and Yeong, W.Y. (2019) Recent Progress in Additive Manufacturing of Fiber Reinforced Polymer Composite. *Advanced Materials Technologies*, **4**, 1800271. <https://doi.org/10.1002/admt.201800271>.
15. Kabir, S.M.F., Mathur, K. and Seyam, A.-F.M. (2020) A critical review on 3D printed continuous fiber-reinforced composites: History, mechanism, materials and properties. *Composite Structures*, **232**, 111476. <https://doi.org/10.1016/j.compstruct.2019.111476>.
16. Pyl, L., Kalteremidou, K.-A. and Van Hemelrijck, D. (2018) Exploration of specimen geometry and tab configuration for tensile testing exploiting the potential of 3D printing freeform shape continuous carbon fibre-reinforced nylon matrix composites. *Polymer Testing*, **71**, 318-328. <https://doi.org/10.1016/j.polymertesting.2018.09.022>.
17. Chacón, J.M., Caminero, M.A., García-Plaza, E. and Núñez, P.J. (2017) Additive manufacturing of PLA structures using fused deposition modelling: Effect of process parameters on mechanical properties and their optimal selection. *Materials & Design*, **124**, 143-157. <https://doi.org/10.1016/j.matdes.2017.03.065>.
18. Hetrick, D.R., Sanei, S.H.R., Bakis, C.E. and Ashour, O. (2020) Evaluating the effect of variable fiber content on mechanical properties of additively

- manufactured continuous carbon fiber composites. *Journal of Reinforced Plastics and Composites*, **40**, 365-377. <https://doi.org/10.1177/0731684420963217>.
19. Iragi, M., Pascual-González, C., Esnaola, A., Lopes, C.S. and Aretxabaleta, L. (2019) Ply and interlaminar behaviours of 3D printed continuous carbon fibre-reinforced thermoplastic laminates; effects of processing conditions and microstructure. *Additive Manufacturing*, **30**, 100884. <https://doi.org/10.1016/j.addma.2019.100884>.
  20. Justo, J., Távara, L., García-Guzmán, L. and París, F. (2018) Characterization of 3D printed long fibre reinforced composites. *Composite Structures*, **185**, 537-548. <https://doi.org/10.1016/j.compstruct.2017.11.052>.
  21. Caminero, M.A., Chacón, J.M., García-Moreno, I. and Rodríguez, G.P. (2018) Impact damage resistance of 3D printed continuous fibre reinforced thermoplastic composites using fused deposition modelling. *Composites Part B: Engineering*, **148**, 93-103. <https://doi.org/10.1016/j.compositesb.2018.04.054>.
  22. Saeed, K., McIlhagger, A., Harkin-Jones, E., Kelly, J. and Archer, E. (2021) Predication of the in-plane mechanical properties of continuous carbon fibre reinforced 3D printed polymer composites using classical laminated-plate theory. *Composite Structures*, **259**, 113226. <https://doi.org/10.1016/j.compstruct.2020.113226>.
  23. Pascual-González, C., San Martín, P., Lizarralde, I., Fernández, A., León, A., Lopes, C.S. and Fernández-Blázquez, J.P. (2021) Post-processing effects on microstructure, interlaminar and thermal properties of 3D printed continuous carbon fibre composites. *Composites Part B: Engineering*, **210**, 108652. <https://doi.org/10.1016/j.compositesb.2021.108652>.
  24. Shih, Y.-C., Mohamed, M., Ge, J., Sen, S., Pillay, S. and Ning, H. (2023) Application of interlaminar shear strength and finite element modeling for failure analysis of 3D printed continuous fiber-reinforced composites. *Progress in Additive Manufacturing*. <https://doi.org/10.1007/s40964-023-00417-8>.
  25. Lin, W.-P. and Hu, H.-T. (2002) Nonlinear analysis of fiber-reinforced composite laminates subjected to uniaxial tensile load. *Journal of Composite Materials*, **36**, 1429-1450. <https://doi.org/10.1177/0021998302036012463>.
  26. Liu, P.F. and Zheng, J.Y. (2010) Recent developments on damage modeling and finite element analysis for composite laminates: A review. *Materials & Design*, **31**, 3825-3834. <https://doi.org/10.1016/j.matdes.2010.03.031>.
  27. Kaddour, A.S., Hinton, M.J., Smith, P.A. and Li, S. (2013) The background to the third world-wide failure exercise. *Journal of Composite Materials*, **47**, 2417-2426. <https://doi.org/10.1177/0021998313499475>.

28. Bourell, D., Kruth, J.P., Leu, M., Levy, G., Rosen, D., Beese, A.M. and Clare, A. (2017) Materials for additive manufacturing. *CIRP Annals*, **66**, 659-681. <https://doi.org/10.1016/j.cirp.2017.05.009>.
29. Meyers, M.A. and Chawla, K.K. (2008) *Mechanical behavior of materials*. Cambridge university press.
30. Gorelik, M. (2017) Additive manufacturing in the context of structural integrity. *International Journal of Fatigue*, **94**, 168-177. <https://doi.org/10.1016/j.ijfatigue.2016.07.005>.
31. Li, S. and Sitnikova, E. (2018) A critical review on the rationality of popular failure criteria for composites. *Composites Communications*, **8**, 7-13. <https://doi.org/10.1016/j.coco.2018.02.002>.
32. Melenka, G.W., Cheung, B.K.O., Schofield, J.S., Dawson, M.R. and Carey, J.P. (2016) Evaluation and prediction of the tensile properties of continuous fiber-reinforced 3D printed structures. *Composite Structures*, **153**, 866-875. <https://doi.org/10.1016/j.compstruct.2016.07.018>.
33. Al Abadi, H., Thai, H.-T., Paton-Cole, V. and Patel, V.I. (2018) Elastic properties of 3D printed fibre-reinforced structures. *Composite Structures*, **193**, 8-18. <https://doi.org/10.1016/j.compstruct.2018.03.051>.
34. Naranjo-Lozada, J., Ahuett-Garza, H., Orta-Castañón, P., Verbeeten, W.M.H. and Sáiz-González, D. (2019) Tensile properties and failure behavior of chopped and continuous carbon fiber composites produced by additive manufacturing. *Additive Manufacturing*, **26**, 227-241. <https://doi.org/10.1016/j.addma.2018.12.020>.
35. Yu, T., Zhang, Z., Song, S., Bai, Y. and Wu, D. (2019) Tensile and flexural behaviors of additively manufactured continuous carbon fiber-reinforced polymer composites. *Composite Structures*, **225**, 111147. <https://doi.org/10.1016/j.compstruct.2019.111147>.
36. Chacón, J.M., Caminero, M.A., Núñez, P.J., García-Plaza, E., García-Moreno, I. and Reverte, J.M. (2019) Additive manufacturing of continuous fibre reinforced thermoplastic composites using fused deposition modelling: Effect of process parameters on mechanical properties. *Composites Science and Technology*, **181**, 107688. <https://doi.org/10.1016/j.compscitech.2019.107688>.
37. Polyzos, E., Katalagarianakis, A., Polyzos, D., Van Hemelrijck, D. and Pyl, L. (2020) A multi-scale analytical methodology for the prediction of mechanical properties of 3D-printed materials with continuous fibres. *Additive Manufacturing*, **36**, 101394. <https://doi.org/10.1016/j.addma.2020.101394>.

38. Wang, F., Zhang, Z., Ning, F., Wang, G. and Dong, C. (2020) A mechanistic model for tensile property of continuous carbon fiber reinforced plastic composites built by fused filament fabrication. *Additive Manufacturing*, **32**, 101102. <https://doi.org/10.1016/j.addma.2020.101102>.
39. Lupone, F., Padovano, E., Venezia, C. and Badini, C. (2022) Experimental Characterization and Modeling of 3D Printed Continuous Carbon Fibers Composites with Different Fiber Orientation Produced by FFF Process. *Polymers*, **14**, 426. <https://doi.org/10.3390/polym14030426>.
40. Wu, Y., Wang, K., Neto, V., Peng, Y., Valente, R. and Ahzi, S. (2022) Interfacial behaviors of continuous carbon fiber reinforced polymers manufactured by fused filament fabrication: A review and prospect. *International Journal of Material Forming*, **15**. <https://doi.org/10.1007/s12289-022-01667-7>.
41. Mankins, J.C. (2009) Technology readiness assessments: A retrospective. *Acta Astronautica*, **65**, 1216-1223. <https://doi.org/10.1016/j.actaastro.2009.03.058>.
42. David Muzel, S., Bonhin, E.P., Guimaraes, N.M. and Guidi, E.S. (2020) Application of the Finite Element Method in the Analysis of Composite Materials: A Review. *Polymers (Basel)*, **12**. <https://doi.org/10.3390/polym12040818>.
43. Sun, C.-T. and Vaidya, R.S. (1996) Prediction of composite properties from a representative volume element. *Composites science and Technology*, **56**, 171-179. [https://doi.org/10.1016/0266-3538\(95\)00141-7](https://doi.org/10.1016/0266-3538(95)00141-7).
44. Kanit, T., Forest, S., Galliet, I., Mounoury, V. and Jeulin, D. (2003) Determination of the size of the representative volume element for random composites: statistical and numerical approach. *International Journal of Solids and Structures*, **40**, 3647-3679. [https://doi.org/10.1016/s0020-7683\(03\)00143-4](https://doi.org/10.1016/s0020-7683(03)00143-4).
45. Sun, C. and Chen, J. (1989) A simple flow rule for characterizing nonlinear behavior of fiber composites. *Journal of Composite materials*, **23**, 1009-1020.
46. Weeks, C. and Sun, C. (1998) Modeling non-linear rate-dependent behavior in fiber-reinforced composites. *Composites Science and Technology*, **58**, 603-611. [https://doi.org/10.1016/S0266-3538\(97\)00183-8](https://doi.org/10.1016/S0266-3538(97)00183-8).
47. Peirce, D., Shih, C.F. and Needleman, A. (1984) A tangent modulus method for rate dependent solids. *Computers & structures*, **18**, 875-887.
48. Bhandari, S., Lopez-Anido, R.A., Wang, L. and Gardner, D.J. (2019) Elasto-Plastic Finite Element Modeling of Short Carbon Fiber Reinforced 3D Printed Acrylonitrile Butadiene Styrene Composites. *Jom*, **72**, 475-484. <https://doi.org/10.1007/s11837-019-03895-w>.



49. Fu, Y.-T., Li, J., Li, Y.-Q., Fu, S.-Y. and Guo, F.-L. (2023) Full-process multi-scale morphological and mechanical analyses of 3D printed short carbon fiber reinforced polyetheretherketone composites. *Composites Science and Technology*, **236**. <https://doi.org/10.1016/j.compscitech.2023.109999>.
50. Polyzos, E., Van Hemelrijck, D. and Pyl, L. (2022) Modeling elastic properties of 3D printed composites using real fibers. *International Journal of Mechanical Sciences*, **232**. <https://doi.org/10.1016/j.ijmecsci.2022.107581>.
51. Ostoja-Starzewski, M. (2006) Material spatial randomness: From statistical to representative volume element. *Probabilistic Engineering Mechanics*, **21**, 112-132. <https://doi.org/10.1016/j.pro bengmech.2005.07.007>.
52. Deng, S., Li, X., Lin, H. and Weitsman, Y.J. (2004) The non-linear response of quasi-isotropic composite laminates. *Composites Science and Technology*, **64**, 1577-1585. <https://doi.org/10.1016/j.compscitech.2003.11.011>.
53. Markforged Inc. (2022) Materials Datasheet - Composites. <https://web-objects.markforged.com/craft/materials/CompositesV5.2.pdf>.
54. Wickramasinghe, S., Do, T. and Tran, P. (2020) FDM-Based 3D Printing of Polymer and Associated Composite: A Review on Mechanical Properties, Defects and Treatments. *Polymers (Basel)*, **12**. <https://doi.org/10.3390/polym12071529>.
55. Schindelin, J., Arganda-Carreras, I., Frise, E., Kaynig, V., Longair, M., Pietzsch, T., Preibisch, S., Rueden, C., Saalfeld, S., Schmid, B. *et al.* (2012) Fiji: an open-source platform for biological-image analysis. *Nat Methods*, **9**, 676-682. <https://doi.org/10.1038/nmeth.2019>.
56. ASTM. (2016), ASTM D2734-16 *Standard Test Methods for Void Content of Reinforced Plastics*. ASTM International, West Conshohocken, PA. <https://doi.org/10.1520/D2734-16>. [www.astm.org](http://www.astm.org).
57. ASTM. (2020), ASTM D792-20 *Standard Test Methods for Density and Specific Gravity (Relative Density) of Plastics by Displacement*. ASTM International, West Conshohocken, PA. <https://doi.org/10.1520/D0792-20>. [www.astm.org](http://www.astm.org).
58. Pascual-González, C., Iragi, M., Fernández, A., Fernández-Blázquez, J.P., Aretxabaleta, L. and Lopes, C.S. (2020) An approach to analyse the factors behind the micromechanical response of 3D-printed composites. *Composites Part B: Engineering*, **186**, 107820. <https://doi.org/10.1016/j.compositesb.2020.107820>.
59. ASTM. (2017), ASTM D3039/D3039M-17 *Standard Test Method for Tensile Properties of Polymer Matrix Composite Materials*. ASTM International, West Conshohocken, PA. [https://doi.org/10.1520/D3039\\_D3039M-17](https://doi.org/10.1520/D3039_D3039M-17). [www.astm.org](http://www.astm.org).



60. Berenbaum, R. and Brodie, I. (1959) Measurement of the tensile strength of brittle materials. *British Journal of Applied Physics*, **10**, 281.
61. ASTM. (2015), ASTM D638-14 *Standard Test Method for Tensile Properties of Plastics*. ASTM International, West Conshohocken, PA.  
<https://doi.org/10.1520/d0638-14>. [www.astm.org](http://www.astm.org).
62. ANSYS, I. (2020) ANSYS Mechanical APDL, Release 2020 R1, Help system, Theory Reference.
63. Simo, J.C. and Ju, J. (1987) Strain-and stress-based continuum damage models—I. Formulation. *International journal of solids and structures*, **23**, 821-840.  
[https://doi.org/10.1016/0020-7683\(87\)90083-7](https://doi.org/10.1016/0020-7683(87)90083-7).
64. Koga, Y., Van Der Klift, F., Todoroki, A., Ueda, M., Hirano, Y. and Matsuzaki, R. (2016), *SAMPE Long Beach 2016 Conference and Exhibition*. Soc. for the Advancement of Material and Process Engineering.
65. Hart-Smith, L. (2002) Expanding the capabilities of the Ten-Percent Rule for predicting the strength of fibre-polymer composites. *Composites science and technology*, **62**, 1515-1544. [https://doi.org/10.1016/S0266-3538\(02\)00092-1](https://doi.org/10.1016/S0266-3538(02)00092-1).
66. Carrillo, J.G. and Cantwell, W. (2007) Scaling effects in the tensile behavior of fiber-metal laminates. *Composites Science and Technology*, **67**, 1684-1693.  
<https://doi.org/10.1016/j.compscitech.2006.06.018>.

APPLICATION OF INTERLAMINAR SHEAR STRENGTH AND FINITE ELEMENT  
MODELING FOR FAILURE ANALYSIS OF 3D PRINTED CONTINUOUS  
FIBER-REINFORCED COMPOSITES

by

YU-CHAO SHIH, MAHMOUD MOHAMED, JUN GE, SUBHAYU SEN, SELVUM  
PILLAY, AND HAIBIN NING

*Progress in Additive Manufacturing*, Vol. 8: pages 1501-1516,

Copyright

2023

by

Springer Nature Switzerland AG

Used by permission.

Format adapted and errata corrected for dissertation.

## ABSTRACT

Continuous fiber-reinforced plastic composite materials are being increasingly used in material extrusion additive manufacturing, typically fused filament fabrication, because it enables unprecedented freedom to manufacture high-performance parts on demand and on-site. Interlayer weaknesses of CFRP made by additive manufacturing need to be addressed to assure the structural integrity of a design that is inherently anisotropic, commonly determined by the characterization of interlaminar shear strength. In this study, ILSS of 3D-printed CFRP composites was characterized with a single-lap joint specimen. It was observed that the ILSS and failure mode changes as a function of the fiber orientation. The layup sequences were found to affect the stress distribution over the joint area, causing non-tensile failure regarding the eccentric load. The bonding quality data was compared to finite element analysis results to map the effective load transfer to the interlaminar area between each printed laminated structure. Stress distribution of the 3D-printed laminated structure under tension loading can be complex, and the results from such tests can be misinterpreted. Based on the present investigation, it is recommended that the layup design should incorporate a balanced stiffness to take advantage of continuous fiber reinforcement.

## INTRODUCTION

Additive manufacturing (AM) has demonstrated the potential to revolutionize manufacturing and enable the deployment of novel materials for advanced applications [1]. AM technology enables performance-driven design [2-4] and an integration-friendly environment to aid the implementation of novel materials into new applications, such as

aerodynamically-enhanced jet engines printed with laser powder bed AM [5], tissue engineering using a hybrid bioprinting method [6], and the unmanned vehicle made of FFF composites [7,8], to name a few. Fused filament fabrication (FFF) is one of the most popular material-extrusion AM technologies, which is capable of utilizing an array of filament feedstock, including continuous fiber-reinforced plastic (CFRP), to form solid object based on its layer-by-layer extrusion process. CFRP composites possess high specific strength and modulus. Continuous fiber reinforcement (CFR) [9-12] technology is the frontrunner for additively manufactured composites for their simplicity, flexibility of architecture design, and tailored performance. AM of CFR utilizes a dual extrusion system to deposit multiple materials alternatively, one of which is the continuous fiber-reinforced plastic composite.

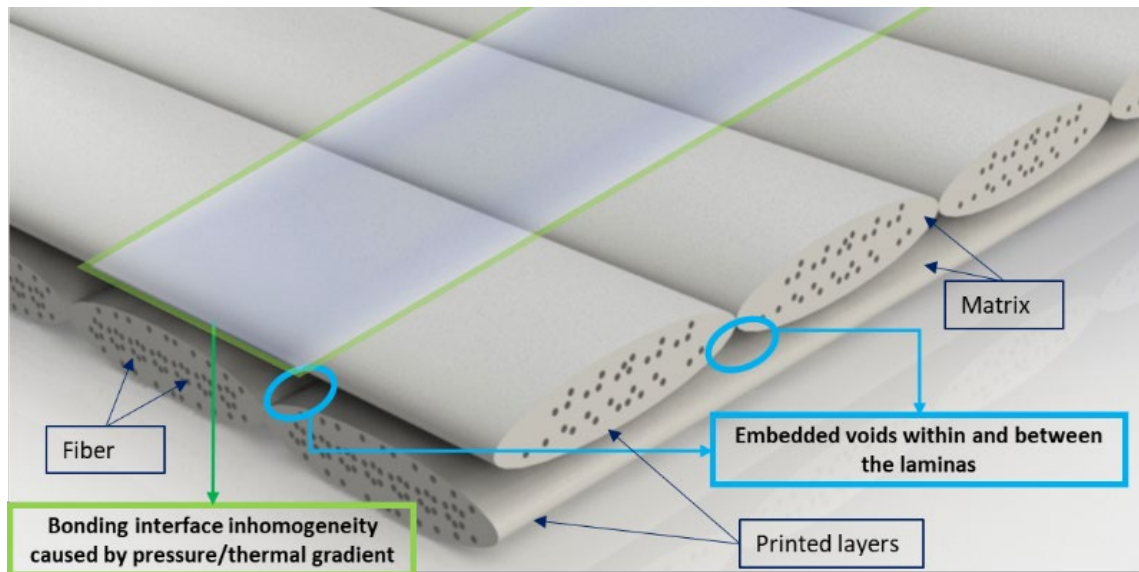


Figure 1. Physical defects in continuous fiber-reinforced plastic composite fabricated with extrusion-based additive manufacturing.  
(Adapted from [13,14])

In spite of the advantages cited above, due to the layered deposition, the main shortcoming of the AM process is the systematic defects embedded within the laminae

and interfacial regions [15], as illustrated in **Figure 1**. The typical void content of a 3D-printed CFRP is reported in the literature to be around 5% [12,16]. Insufficient consolidation could cause poor adhesion or interfacial bonding issues [17]. This is a direct manifestation of the gradient solidification during the extrusion-deposition procedure. Based on the inherent interfacial defects within the structure, the primary composite failure modes are shown in **Figure 2**. The similarities of these failure modes between conventional composites and AM structures have been previously discussed elsewhere [13,18,19]. The most straightforward criterion to predict such failure is the interlaminar shear strength (ILSS), which prescribes the failure to occur upon reaching a critical threshold. One of the standard ILSS characterization methods is the short beam shear (SBS) test, which applies a flexural load on a thick specimen to monitor the shear strength of the neutral layer upon delamination. Many authors have investigated the ILSS of 3D printed composites with SBS samples as a function of fiber type, layer thickness, and fiber orientations. [20-22] SBS test results from the literature suggest a low ILSS value for 3D-printed composites compared to commercial composites, concluding that the embedded voids are the primary contributing factor. Iragi et al. [16] went one step further to characterize the mechanical properties at the lamina level, including mode I and mode II fracture toughness. The inefficiency of the reinforcement was evidenced by several studies [20,22-24] showing that ILSS and tensile properties do not increase proportionally with higher fiber volume fraction. Despite the apparent use of the SBS test for quantifying ILSS, the method is limited to unidirectional and symmetrical ply.

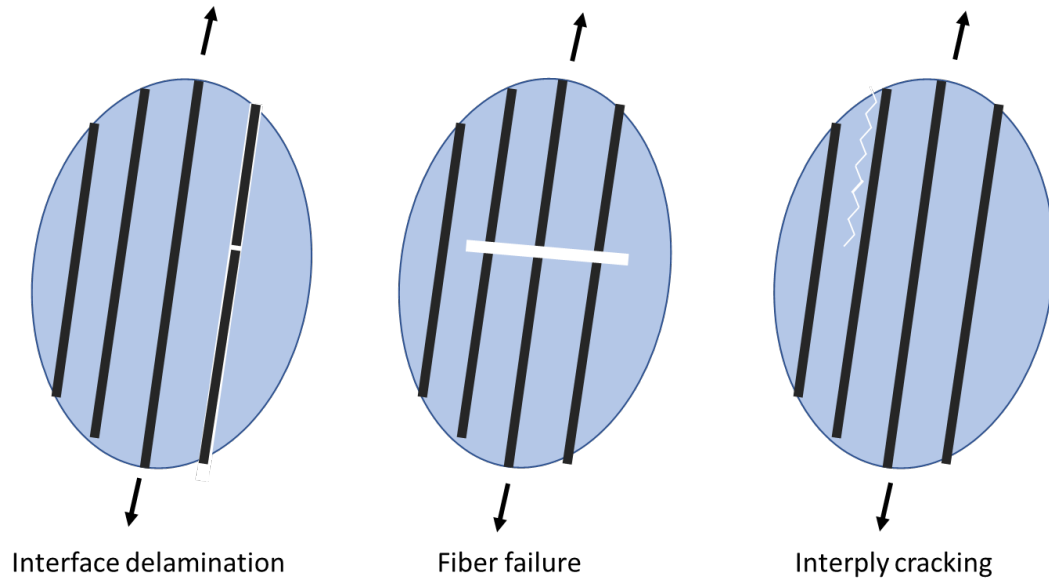


Figure 2. Typical failure modes of conventional additively manufactured continuous fiber-reinforced plastic composites.  
(Adapted from [25])

Characterization of the bonding quality of an adhesive-bonding system is highly specialized as load transfer between dissimilar materials and bonding geometry can be nontrivial, resulting in complex stresses. Single-lap joint (SLJ) test is widely used to compare adhesion strength for varying conditions due to its simplicity in design and application [26]. The SLJ sample is composed of two lapped bodies bonded with a layer of adhesive [27], and tension is applied to induce shear stress at the joint. Despite the simplicity of manufacturing the testing specimens, caution must be exercised to prevent misuse of the SLJ stress as allowable design stress because of the complex stress in the system [28]. Milestone SLJ stress field analysis includes the Goland and Reissner analysis, accounting for load eccentricity and beam bending [29] and Volkersen's differential shear treatment [30]. A representative sandwich element of two adherend bodies and a layer of adhesives is usually used in the analysis based on the formulations of plate theories [31].

Analytical models for bonded joints were reviewed, implemented, and compared by da Silva [32,33] as to provide an accurate prediction of SLJ strength. A lap shear test is usually conducted to examine the interlaminar bonding of adhesives between bonded surfaces on a quantitative and comparative basis [27,29,34]. Other than the intended use of functional evaluation of a designed bonded joint, the growing popularity of using the SLJ specimen for characterizing the interfacial bonding strength of fiber-reinforced laminate or 3D-printed structure has been discussed elsewhere in the literature [35-40]. A considerable sum of analytical treatments for SLJ specimens is available to be implemented in the analytical and numerical analysis [32,41]. However, the nature of the prescribed adhesive thickness and mostly plane stress simplification does not necessarily apply to AM FRP specimens due to its complex laminate blending profile and structural integrity within the laminae. From the material standpoint, the AM FRP differs from conventional beam samples as it is highly anisotropic and possesses weaker bonding among layers.

This study aims to develop a novel methodology to analyze the fracture behavior of the SLJ specimen in relation to continuous fiber orientation and stacking sequences. The coupling of voids and the inherent anisotropic nature of an AM composite material can further complicate its structural integrity assessment. It is demonstrated that a combination of experimental results and a simulation approach can be used to optimize the performance. Interlaminar bonding quality assessment of AM FRP composites, including unbalanced laminated SLJ specimens, was further advanced using a physics-based observation of the failure of SLJ specimens. Finite element analysis (FEA) was implemented to analyze the stress distribution profile over the lapped length, which accounts for

geometric deflection on the laminated SLJ specimens. The fracture morphologies and load were recorded and correlated to the stress field results from the simulation.

## MATERIALS AND METHODS

### Materials and Equipment

All CFRP samples were fabricated with the Mark Two 3D printer (Markforged, MA, USA). Mark Two is a desktop composite 3D printer using the principle of material extrusion-based additive manufacturing technologies of FFF and continuous fiber reinforcement (CFR). Onyx, a chopped carbon fiber reinforced PA6 composite filament, and continuous carbon fiber (CCF) composite filament were used to manufacture specimens. Printing parameters were pre-set at a printing temperature of 270°C on both extrusion outlets and a layer height of 0.125 mm. A 100% infill matrix, labeled as solid infill, was chosen to fabricate the specimen in this study based on a rectangular infill pattern of alternate +45°/-45° raster angle. The specimen geometry was made with the commercial CAE software Solidworks 2021 (Solidworks, Dassault Systems, Tennessee). Tensile tests following the procedure specified by ASTM D3039 were used to get a baseline property for composites made from 100% Onyx and 100% continuous carbon fiber composite filaments, respectively. All mechanical tests were conducted on an MTS 810 system with a 2 kN load cell. The result would be used in further analysis to generate baseline lamina parameters in FEA.

### Single-lap Shear Test

All SLJ specimens were manufactured with the Mark Two 3D printer. The specimens would be subjected to a 2 mm/min constant crosshead rate until failure, for which



the load-displacement relationship was recorded. The maximum length of the overlapping area to ensure failure at the bonded joint region was determined by the equation [42],

$$L < F_{ty}T/\tau \quad (1)$$

in which  $L$  is the overlap length,  $T$  is the adherend thickness,  $F_{ty}$  is the yield strength of the adherend, and  $\tau$  is 50% of the estimated average shear strength in the bonded joint [43]. The overlapped length of  $L = 6.4$  mm was conservatively chosen for all configurations to avoid undesired tensile failure on the adherend based on the properties from the literature [16] and this study. The SLJ specimens are dimensionally symmetric, and each adherend beam is dimensioned at  $82.55 \times 12.7 \times 3$  mm with an overlapping area of  $6.4 \times 12.7$  mm, as shown in **Figure 3a**. **Figure 3b** shows the engineering drawing of the specimen with detailed dimensions. The formulation suggested by ASTM standard to calculate the single-lap joint strength considers the load fully applied on a simplified interfacial area over the bonded adhesive joint [28,42,43]. Under this context, the average shear strength is:

$$\tau = \frac{P}{bl} \quad (2)$$

where  $P$  is the load at failure,  $b$  is the width of the joint, and  $l$  is the single-lap length.

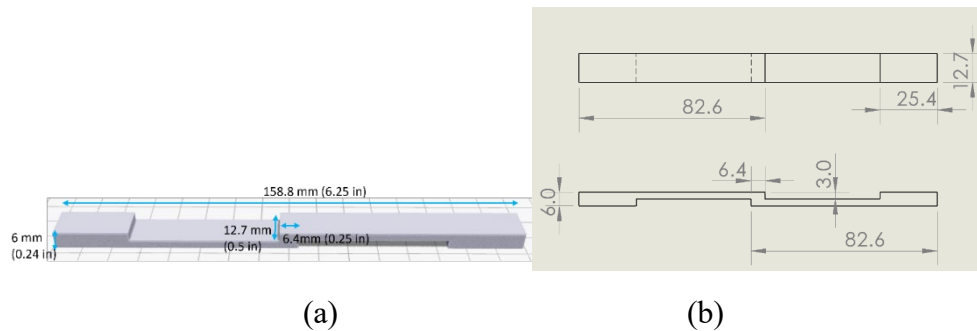


Figure 3. Single-lap joint specimen design, (a) isometric view, (b) engineering drawing. (Unit: mm)

**Table 1** shows the fiber layout orientation and purposes of each SLJ specimen design variant. Three specimens were printed and tested for each variant. Designed configurations are summarized below in **Figure 4**. Additional baseline samples B1 for pure Onyx and B2 for 4-ply Onyx interface reinforced with four 0°-ply outside of the bonded joint were configured. B1 and B2 compare the SLJ strength of the Onyx interface with and without stiffener plies outside of the load path. Each specimen was printed with an automatically generated support structure under the upper adherend. The support structure was removed before being tested.

Table 1. Experiment design on single-lap joint shear test for FRP composites.

<b>Designation</b>	<b>Purpose</b>	<b>Description</b>
<b>M</b>	Evaluate the effect of fiber layups between interfacial bonded areas.	Orientation of a 4-ply laminated structure Five different layer sequences at the lap joint: (0° - 0°; 0° - 90°; 90° - 90°; 0° - 45°; 45° - 135°)
<b>N</b>	Evaluate the effect on the extensional stiffness and asymmetry on the adherend beam	Orientation of an 8-ply laminated structure Three different layer sequences at the lap joint: (0°/45° - 135°/0°; 0°/90° - 90°/0°; 0°/90° - 0°)
<b>O</b>	Evaluate the effect of a buffer layer between unidirectional CF reinforcement	Orientation of 1 or 2 plies between the 4-ply 0°CF Three different layer sequences at the lap joint: (45°; 90°; Onyx-45°)

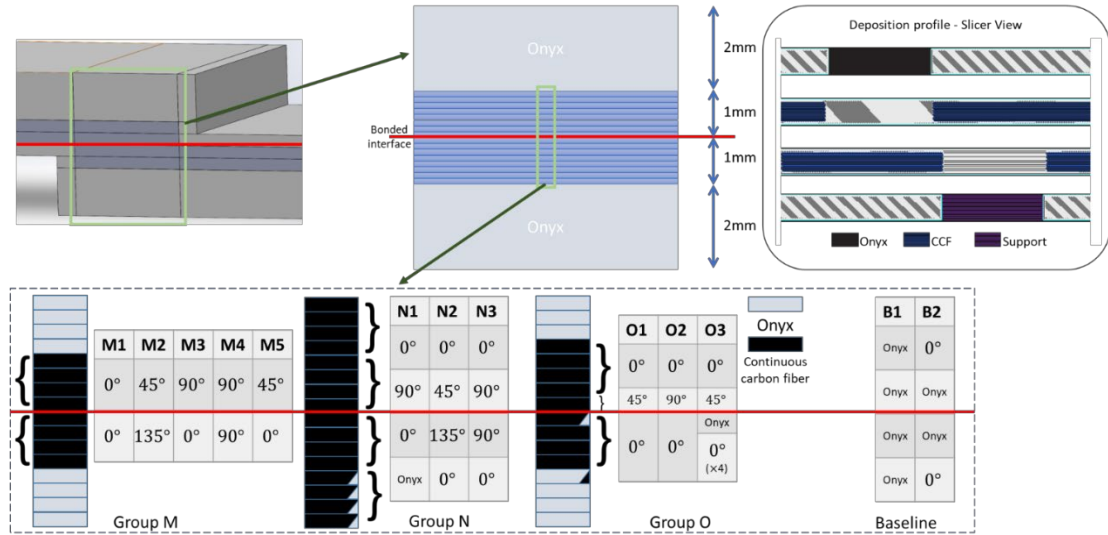


Figure 4. Schematics of fiber layout sequences over the bonded joint for the SLJ specimen design.

### Fracture Surface Analysis

Morphological observation of the fracture surface is the centerpiece of identifying the onset of the fracture and the failure mode itself. The structural integrity of an interlaminar area between two adherends can be assessed by matching a specific fracture pattern defined by the corresponding type of stress. Failure mode recognition of the AM composite SLJ samples was performed with a modified figure similar to the ASTM D5573 (Standard Practice for Classifying Failure Modes in Fiber-Reinforced-Plastic (FRP) Joints) [44]. Images of the fracture surface specimens were taken with DinoLite AM3111 digital microscopy with 0.3-megapixel image resolution. Side images were also taken to identify the location of the fracture onset. The fracture mode can be a manifestation of a combination of stresses, namely longitudinal tensile stress, through-thickness peel stress, and interlaminar shear stress.

## Finite Element Analysis

Finite element analysis (FEA) has been used extensively in modeling laminated composites to provide accurate stress fields at a laminate level [45]. Using an engineering FEA suite, ANSYS professional 2022R1, a three-dimensional FEA was conducted to simulate the stress field of the SLJ specimen. Material properties were calibrated with the tensile test results, such that the simulation of nonlinear Onyx softening behavior was permitted throughout straining. The ten-percent rule [46] was used as an approximation tool for required out-of-plane properties, assuming the transverse modulus as one-tenth of the longitudinal modulus. The solid model was constructed with geometrical detail, including all walls and other configured features. The laminated composition was configured with the ANSYS Composites PrePost (ACP) using orthotropic material properties and element SOLID185, nominally known as a homogeneous brick element. The SOLID185 has eight nodes, each with 3 degrees of freedom (DoF). The enforced load of failure on each configuration was set on one side of the adherend and fixed support on the other. Non-slide boundary conditions were applied to the tabbed surfaces to constrain the models as in the experiment. The interfaces were assumed to be perfectly bonded since the interlaminar shear strain is minor compared to the extensional strain of the adherend until joint failure by sudden debonding. Twenty-four sub-steps were implemented with a 6-second pseudo-time to capture the nonlinearity of the model. The through-thickness peel, tensile, and interlaminar shear stress were recorded, plotted, and compared to the experimental data. A set of convergence studies was conducted to ensure sufficient mesh discretization with the prescribed element size [47] to avoid stress singularity and improve precision. Trials have been conducted with element sizes of 8 mm, 4 mm, 3 mm, 2

mm, 1.2 mm, 0.8 mm, 0.5 mm, 0.4 mm, 0.2 mm, and 0.15 mm within the lamina, while the thickness remains unchanged. It was determined that the element size of 0.2 mm is sufficient for a valid result.

## RESULT AND DISCUSSION

### Feedstock Material Characterization

The tensile specimen was dimensioned at  $152 \times 12.7 \times 6.4$  mm, with the gage length set to 76.2 mm. The outer wall layers of the CCF specimen have been removed to achieve the composition of 100% CCF filaments. The characterized tensile modulus and strength are shown in **Table 2**. The nonlinear plasticity on the stress-strain relationship of the matrix Onyx was calibrated, and the result was used in the simulation as material properties. The elastic and plastic segments of the tensile stress-strain data of Onyx were input into the model to develop proper responses of the AM printed samples.

Table 2. Tensile test results for continuous fiber-only and Onyx-only 3D-printed composites.

Material	Modulus (GPa)	Strength (MPa)
Laminated Carbon fiber	$66.5 \pm 0.7$	$811.0 \pm 18$
Laminated Onyx	$1.26 \pm 0.1$	$34.4 \pm 1.6$

Each SLJ specimen was measured before the tests to assess the dimensional deviation. The width and length of the overlapped area were recorded and compiled. The average dimensional deviation of the overlapping area was found to be minimal (around 2%).

## Lap Shear Results

SLJ results from all M, N, and O specimens were summarized in **Figure 5**. The baseline SLJ strength of pure Onyx specimen B1 and stiffened Onyx B2 are also included. Group M data shows the highest shear stress for  $0^\circ$ - $0^\circ$  (M1) at 28.5 MPa, and the lowest at 10.2 MPa for  $90^\circ$ - $90^\circ$  specimens. The peeling force on the edge of the joint induced by beam bending under tensile load weakens the structural integrity of the 3D-printed single-lap joint, resulting in a 12.3% lower strength of 25 MPa for  $0^\circ$ - $45^\circ$  (M5), a 48.5% lower strength of 14.7 MPa for  $0^\circ$ - $90^\circ$  (M3), 53.7% lower strength of 13.2 MPa for  $45^\circ$ - $135^\circ$  (M2), and a 64.2% lower strength of 10.2 MPa for  $90^\circ$ - $90^\circ$  (M4). It is observed that although the presence of an imbalanced beam of greater stiffness would induce additional bending, the overall structural strength of M3/M5 is still larger than those without  $0^\circ$  plies (M2, M4).

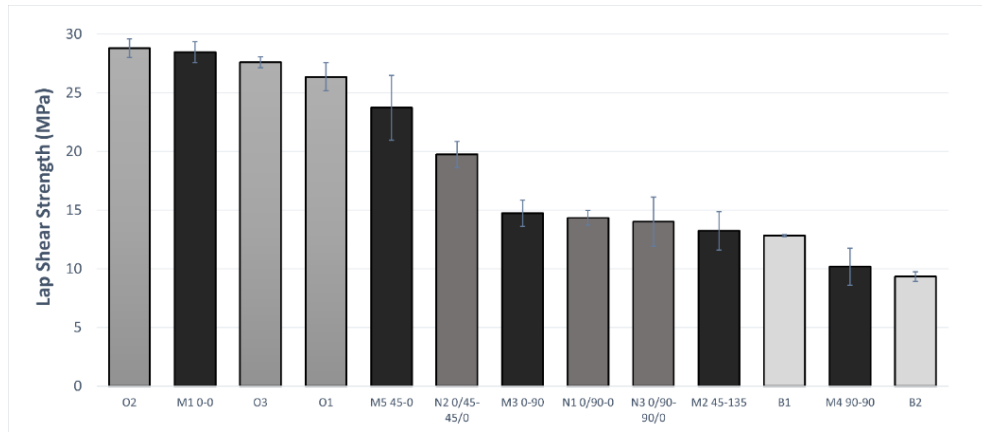


Figure 5. Comparison of all SLJ results by group.

All group M results were plotted in **Figure 6**. The  $0^\circ$ - $0^\circ$  specimen shows the lowest strain-to-failure while the  $90^\circ$ - $90^\circ$  shows the highest strain-to-failure. The other configurations have the strain-to-failure in between. It was found that a lower strain-to-failure showed the highest failure load, and a higher strain-to-failure showed a lower failure

load. The relationship implies that the bonded structure could bear more loads with a higher beam modulus by reducing load eccentricity. The ILSS from the literature suggests  $\sim 30\text{MPa}$  for CF-Onyx composites with the SBS test [16], which is consistent with the result in this study. The SLJ result gives a more conservative estimation because of the presence of additional bending from the geometry's free edges. The stress concentration over the free edges was alleviated by the enclosure walls and layered structures. The enclosure constituted of the base material was configured to protect the integrity of the samples as well as prevent failure on free edges by stress concentration, permitting strain energy to be released by straining. The mechanism is similar to a mixed-adhesive joint (MAJ) [48,49], for which the adhesively bonded lapped region consists of a rigid adhesion in the middle section and two flexible adhesion on the sides. The effect of eliminating the excessive interlaminar shear stresses on the unsupported free edges under tensile loading was evident in this study and is consistent with that stated in [50]. Group N shows that the N2 specimen has an average strength of  $19.5\text{ MPa}$ , which is 35% higher than the  $14.4\text{ MPa}$  of the N3 specimen. The failure mode of mixed intralaminar failure on N3 stiffened  $90^\circ$ - $90^\circ$  also differs from the cohesive interlaminar debonding on a stiffened  $45^\circ$ - $135^\circ$  of N2. The result confirms that the  $90^\circ$  layer is more susceptible to a composite shear-peel loading. Although the N1 and N3 differ by four unidirectional  $0^\circ$  layer layers, the resulting SLJ shear strength does not result in a significant difference. It is reasonable as the fiber orientation around the section of stiffness centroid is identical and prone to a lamina failure on the  $90^\circ$  layer.

Group O result shows the effect of an additional off-axis buffer layer on specimens with similar structural bending stiffness. The O2 specimen has the highest strength

of 28.8 MPa for the additional 90° layer, which gives extra flexibility on the stress-concentrated x-direction. It is followed by 27.6 MPa for the O3 specimen that was buffered with a 45°-Onyx bilayer over the interlaminar centroid region, and the lowest of 26.4 MPa for O1, which has an additional 45° layer. The comparable SLJ strength of group O result confirms the previous assumption that structural stiffness in the loading direction is the primary factor in SLJ strength. The additional buffer layer in the O specimens does not improve the shear strength significantly compared to the M1 0°-0°. The boxplot of the groups M and N results are shown in **Figure 7**, which also displays the variability on each configuration. Similarity was found in the plateaued trend in M3-N1-N3 for the presence of the 0-90 interface. It is evident that the reinforced 0°-90° configuration is prone to lamina failure on the 90° layer. Comparing these two groups shows that the fiber orientation type is the most important parameter, followed by the beam stiffness. The interval plot for the 95% confidence interval (CI) result of all continuous FRP specimens is listed in **Figure 8**.



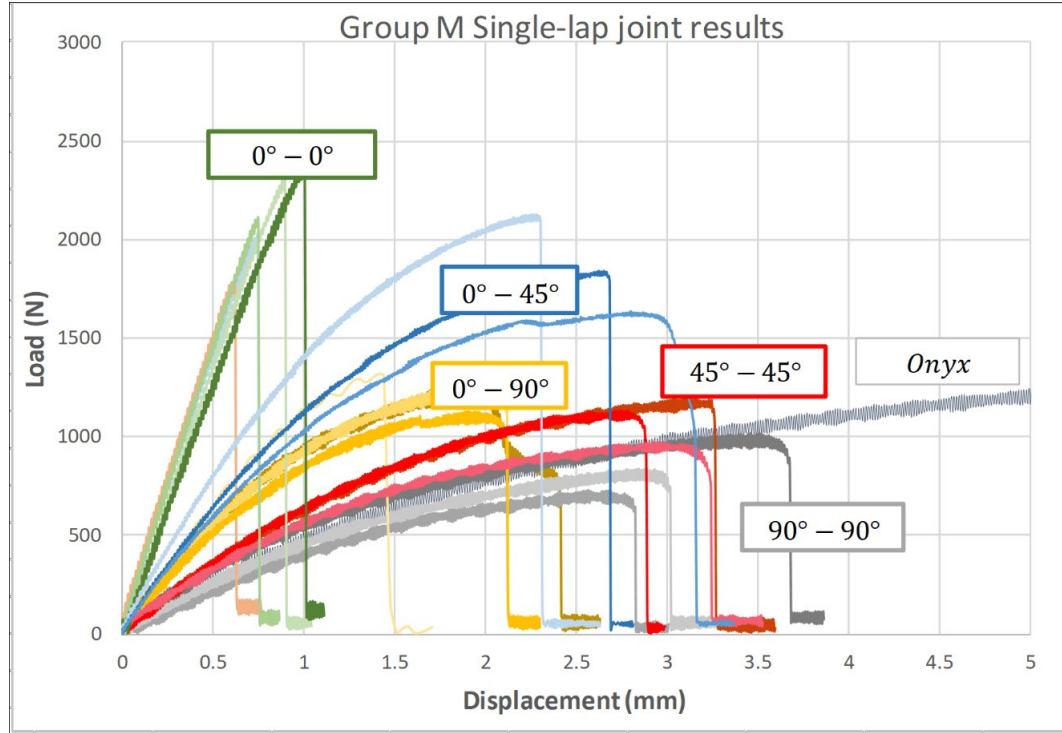


Figure 6. Load-displacement curves of all group M results with Onyx baseline.

The result shows that as the stiffness of the weaker adherend increases, the SLJ strength increases drastically. A greater lap shear strength was observed when both adherends had higher longitudinal stiffness. A significant peel effect was observed on those with higher bending angles, which could be subsequently exacerbated by low flexural stiffness on symmetrical samples and the degree of stiffness difference between two adherends on asymmetrical samples. From the SLJ strength in descending order 0-0 (M1) > 0-45(M5) > 45-135(M3) > 0-90(M2) > 90-90(M4), it can be surmised that an important parameter that affects the SLJ strength is the interface type at the interlaminar region. The 0° layers near the stiffness centroid can decrease load eccentricity with the increased flexural stiffness, resulting in higher effective shear stress on the beam. In contrast, the bending effect would result in greater peel stress if the stiffness centroid has lower flexural rigidity. This was also evidenced in the B2 samples, which had the lowest SLJ strength due

to the off-axis load that causes peel-dominant delamination. It is concluded that the stress composition resulting from the load situation would play an essential role in the structural assessment.

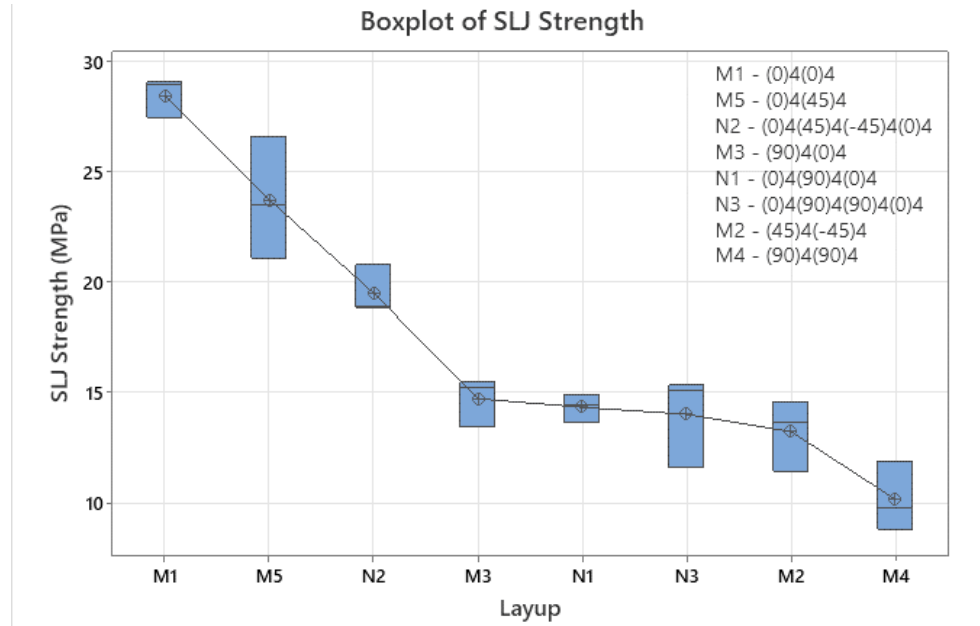


Figure 7. Result of SLJ strength of continuous FRP composites on groups M and N.

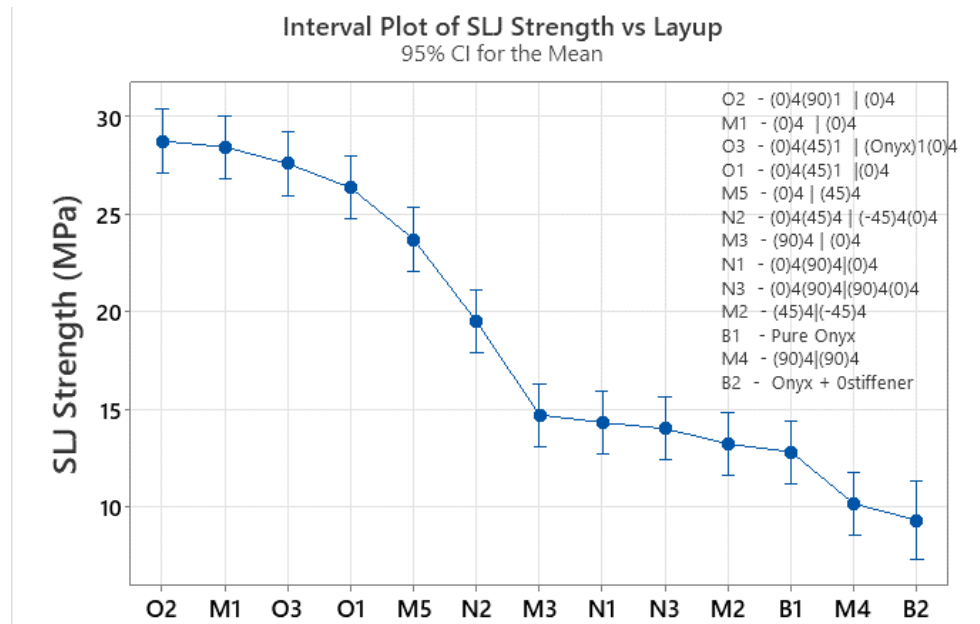


Figure 8. 95% confidence interval of the mean on all CFRP composites (M, N, O).

## Fracture Analysis

The primary fracture types of the SLJ samples are summarized in **Figure 9**. Type A shows a shear-dominant failure mode as the fracture propagates through the interlaminar region. Type B is associated with concentrated peel stress along the edges of the lapped joint. Type C displays a lamina failure by tensile stresses, in which the failure scheme is almost certain to be the result of a combination with A or B. Type D displays an invalid test result where adherend tensile failure occurs. Fracture morphologies on the side of all SLJ specimens were identified and listed in **Figure 10**. Detailed recognition schematics were made regarding the proposed identification scheme in **Figure 9**.

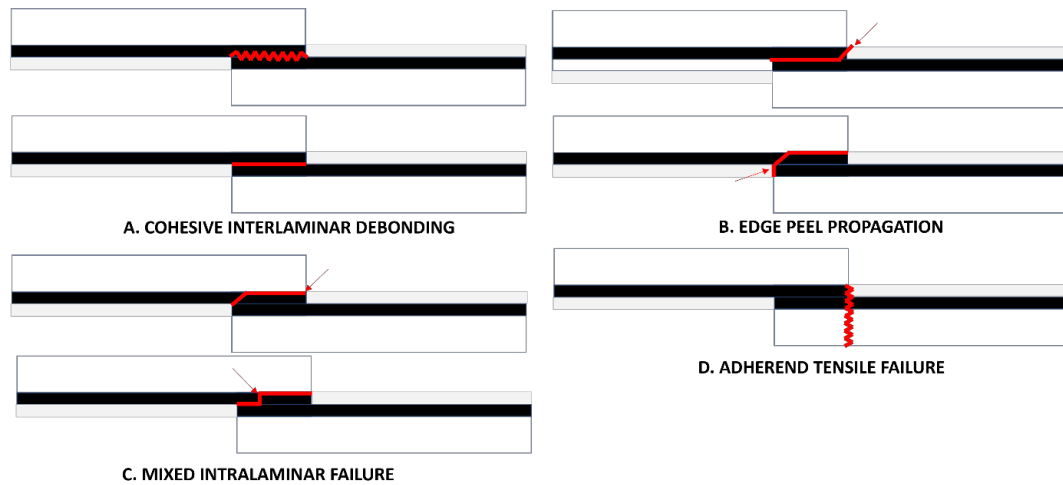


Figure 9. Failure mode determination of SLJ specimen.  
(Adapted from [44])

Configurations of M1, N2, O1, and O3 have been recognized to fail within the centroid layer as they possess a balanced adherend stiffness, and the edges are not prone to mode II shearing as opposed to the specimens with a  $90^\circ$  ply. Configurations M2 and M4 were found to undergo intralaminar fracture within the four off-direction plies region, which could result from a combination of peel and shear. The lack of extensional stiffness

would incur higher peel stresses, as corroborated by the simulated stress field. Configuration M3, M5, N1, N3, and O2 all have a failure occurring within the interlaminar 45°/90 layers, potentially caused by the mixed loading of concentrated peel/shear stresses on the off-axis lamina. It is also possible that the modulus mismatch between the off-axis ply and the adjacent 0-degree layer induced additional interlaminar shear stress that promoted fracture.

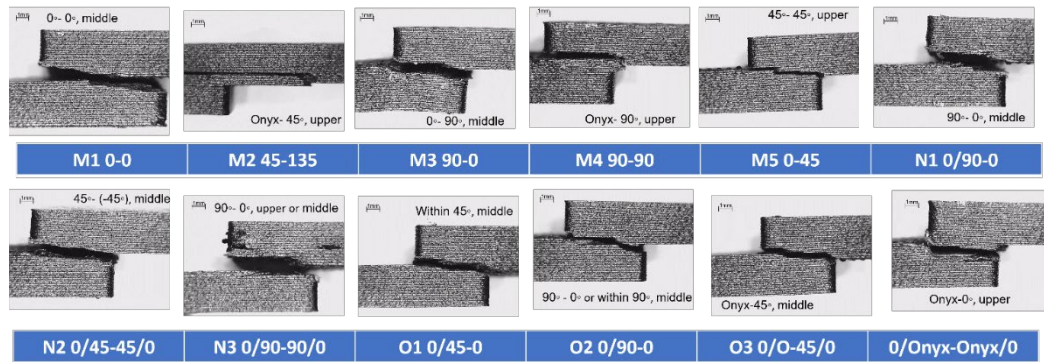


Figure 10. Interlaminar fracture identification for all SLJ specimens.

The results of SLJ strength and failure mode recognition for group M, N, O, and B2 specimens were plotted in **Figure 11**. Failure modes of the samples were determined according to **Figure 9**. The result is consistent with the shear strength value when the failure occurs within a non-0° layer. Decreased properties were observed when a layer of weak tensile strength was presented, namely in the 45° and the 90° layers. The failure on those specimens was caused by inadequate intralaminar bonding between each linear placement of directional fiber. Comparing the strength and fracture mode in M3, N1, and N3 shows an identical pattern for their similar composition of mismatched 0°-90° interface. Statistical treatment reveals that the variation among these three configurations is non-significant, which supports the claim that additional 0° stiffeners would not

effectively reinforce the beam if the shear-dominated failure occurs. M2 and M4 specimens displayed the lowest SLJ strength amongst all the M, N, and O configurations. It is to say that a successive off-axis layer without unidirectional reinforcement could spur a structural weakness, especially when the off-axis load encounters them. The B2 sample of the Onyx at the interlaminar area with an additional  $0^\circ$  stiffener displays the lowest SLJ strength, resulting from failure between the Onyx and unidirectional  $0^\circ$ . It is concluded that delamination occurs on the B2 while undergoing eccentric loading.




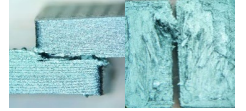

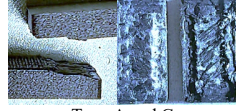




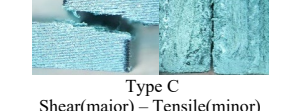
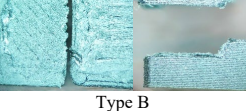
Sample	$\sigma_{avg}$ (MPa)	Fracture surface morphology	Sample	$\sigma_{avg}$ (MPa)	Failure surface morphology
M1 (0) <sub>4</sub> – (0) <sub>4</sub>	28.5 ± 0.9	 Type A and B Shear(major) – Tensile(minor)	N2 (0) <sub>4</sub> (45) <sub>4</sub> – (45) <sub>4</sub> (0) <sub>4</sub>	19.5 ± 1.1	 Type A Shear(major) – Peel(minor)
M2 (45) <sub>4</sub> – (45) <sub>4</sub>	13.2 ± 1.6	 Type C Tensile(major) – Peel(minor)	N3 (0) <sub>4</sub> (90) <sub>4</sub> – (90) <sub>4</sub> (0) <sub>4</sub>	14.0 ± 2.1	 Type B and C Shear(major) – Tensile(minor)
M3 (0) <sub>4</sub> – (90) <sub>4</sub>	14.7 ± 1.1	 Type A and B Shear(major) – Tensile(minor)	O1 (0) <sub>4</sub> (45) <sub>1</sub> – (0) <sub>4</sub>	26.4 ± 1.2	 Type A and C Tensile(major) + Shear(minor)
M4 (90) <sub>4</sub> – (90) <sub>4</sub>	10.2 ± 1.6	 Type C Tensile(major) – Peel(minor)	O2 (0) <sub>4</sub> (90) <sub>1</sub> – (0) <sub>4</sub>	28.8 ± 0.8	 Type A and B Tensile(major) + Shear(minor)
M5 (0) <sub>4</sub> – (45) <sub>4</sub>	25.0 ± 2.2	 Type B and C Tensile(major) – Shear(minor)	O3 (0) <sub>4</sub> (Onyx) <sub>1</sub> – (45) <sub>1</sub> (0) <sub>4</sub>	27.6 ± 0.5	 Type A Tensile(major) – Shear(minor)
N1 (0) <sub>4</sub> (90) <sub>4</sub> – (0) <sub>4</sub>	14.3 ± 0.6	 Type C Shear(major) – Tensile(minor)	B2 Onyx + stiffener (0) <sub>4</sub> (Onyx) <sub>4</sub> – (Onyx) <sub>4</sub> (0) <sub>4</sub>	9.3 ± 0.4	 Type B Peel(major) – Shear(minor)

Figure 11. Single-lap shear results for continuous fiber-reinforced composites with different fiber layups between adjacent interlaminar layers.

Fracture propagation was observed to jump to the adjacent layer in specimens M1, M3, M5, N3, O2, and stiffened Onyx. Other than the weakness of interlaminar debonding, another probable reason is the defects embedded systematically along the extrusion tool path. The type B failure of crack propagation through the gap between the continuous fiber and the wall enclosures weakened the strength. The propagation might also be attributed to other intralayer defects induced by the printing process, such as void and unfilled regions. General fracture modes in SLJ specimens are cohesion, adhesive, or adherend failure, which can apply to the 3D printed composite sample within the scope of **Figure 9** for types A, C, and D, respectively. The fracture could occur along the eccentric load path, defined by the EC, to the intersection of the interlaminar bonding area. The resulting stresses might also cause intralaminar failure upon encountering a weaker lamina. Identical failure modes were observed in N1 and N3. The additional 0° layer did not improve the structural integrity. Instead, it introduced more bending moments on the unsupported edges, which caused type B fracture propagation. Group O specimens were designed to test the interfacial strength between fiber layups with a near-symmetrical stiffened beam. Failure morphologies on the group O specimens show that the stiffened beam can effectively resist peel-induced bending, keeping the load transfer properly on the single-lap joint. Although the additional interlaminar buffer layer of 45°, 90°, and 45° - Onyx were expected to provide an additional strain energy-releasing effect, the difference between the O specimens and M1 0-0 is not significant.

#### Stress Field from FEA

The simulated results were grouped according to their characteristics, namely symmetric, semi-symmetric, and asymmetric. The stress field data were probed at the

interfacial element surfaces within the middle section of the overlap area between the two sets of the 4-ply laminated structure. The data presented are of the shear stresses acting along the shear-loaded XZ surfaces, as x is the longitudinal direction and z is the through-the-thickness direction. The flexible Onyx outermost walls were excluded from the probed region to avoid stress singularity, abrupt straining at the free edges, and the plastic spew effect stated in the previous section. The nonlinear mechanical response of the matrix materials was modeled using an isotropic multilinear plasticity model by curve-fitting of the plasticity zone over the stress-strain curve of pure Onyx samples. The calibration process was done using the tensile data, following the instructions in the ANSYS manual [51]. The normalized stress distribution on configuration N3 using a 0.2 mm element size was plotted in **Figure 12**, and the resulting trend is identical to the distribution generated by analytical models [28,32].

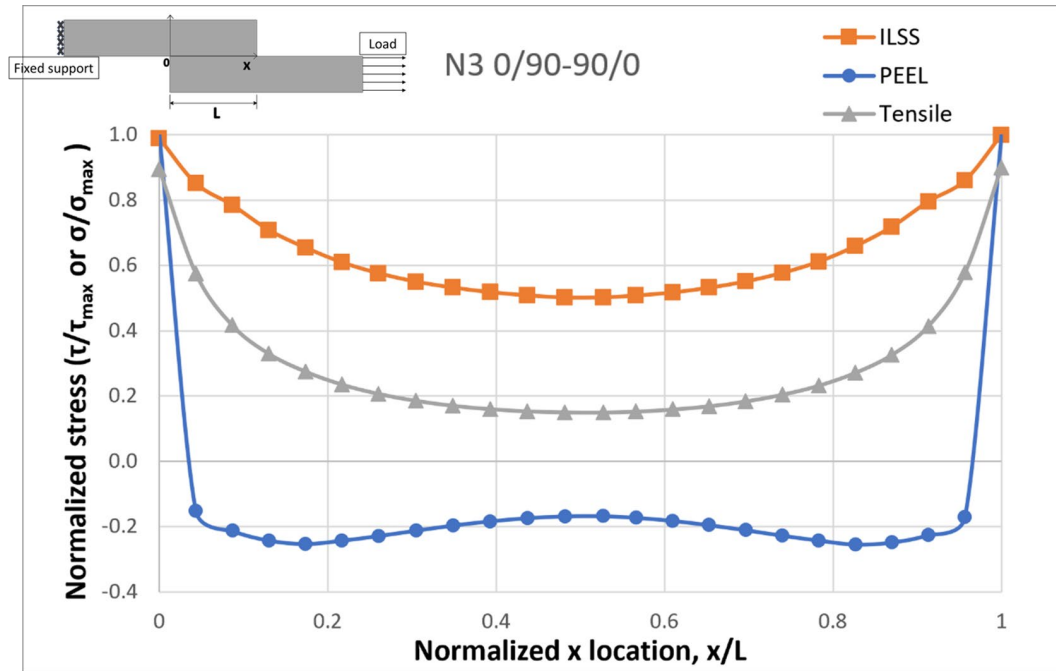


Figure 12. The simulated normalized stress distribution along the normalized x location.



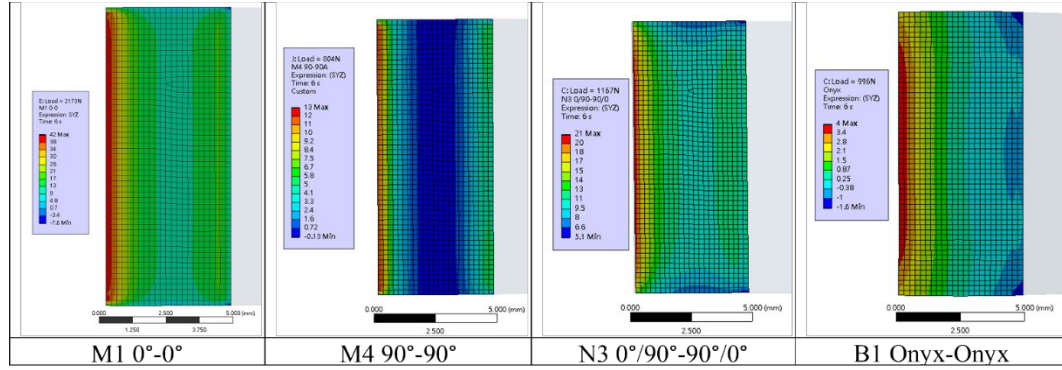


Figure 13. FEA result of shear stress distribution - symmetrical adherends (unit: MPa).

Four configurations were marked as symmetrical samples, including M1, M4, N3, and B1. The simulated shear stress distributions are presented in **Figure 10**. The ILSS and peel stress distribution profile along the normalized distance from the interlaminar bonded lap between two configured fiber laminae were plotted in **Figure 14**. The stress concentration factor was calculated by dividing the stress resultant at each location by the simulated average SLJ strength. It is observed that by introducing 0° unidirectional ply as reinforcement, the additional bending stiffness would allow the structure to reduce the stress concentration on the edges of the bonded region. The result of the N3 also shows that the shear stress distribution could be more homogeneous by blending the lamina layout with 0°-90° along the loading line. Although N3 has more evenly distributed shear stress, the concentrated peel stresses on the free edges result in structural weakness, and the corresponding SLJ shear stress of N3 is only at 30% of the M1 configuration. The results of asymmetrical and semi-symmetrical adherends were compiled and plotted in **Figure 15** and **Figure 16**, respectively. The maximum shear stresses were observed in the vicinity of the interlaminar bonding edges, which are of opposite directions on two sides for some of the samples.



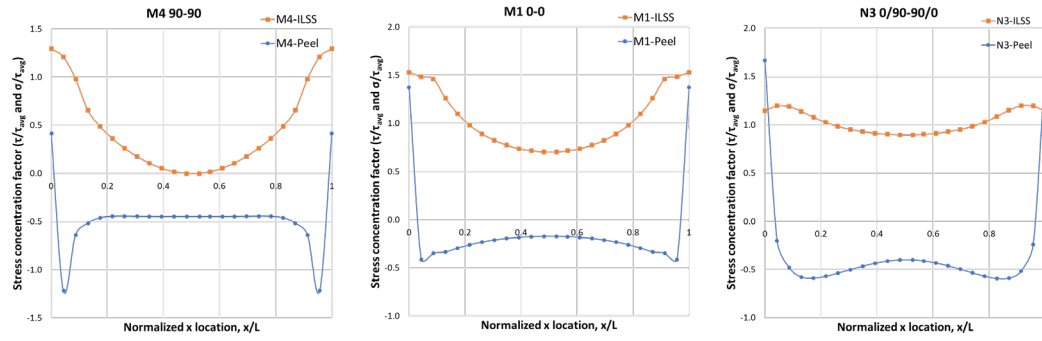


Figure 14. Normalized stress distribution on CFRP samples with symmetrical adherends for ILSS and peel.

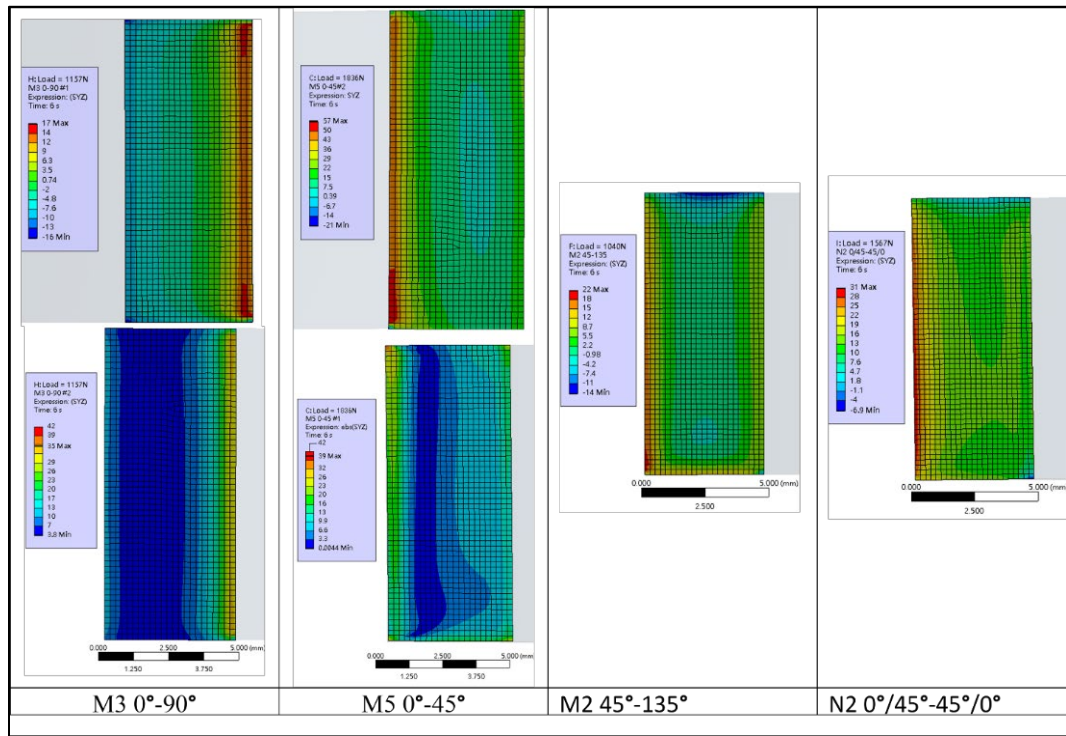


Figure 15. FEA result of shear stress distribution – asymmetrical adherends (unit: MPa).

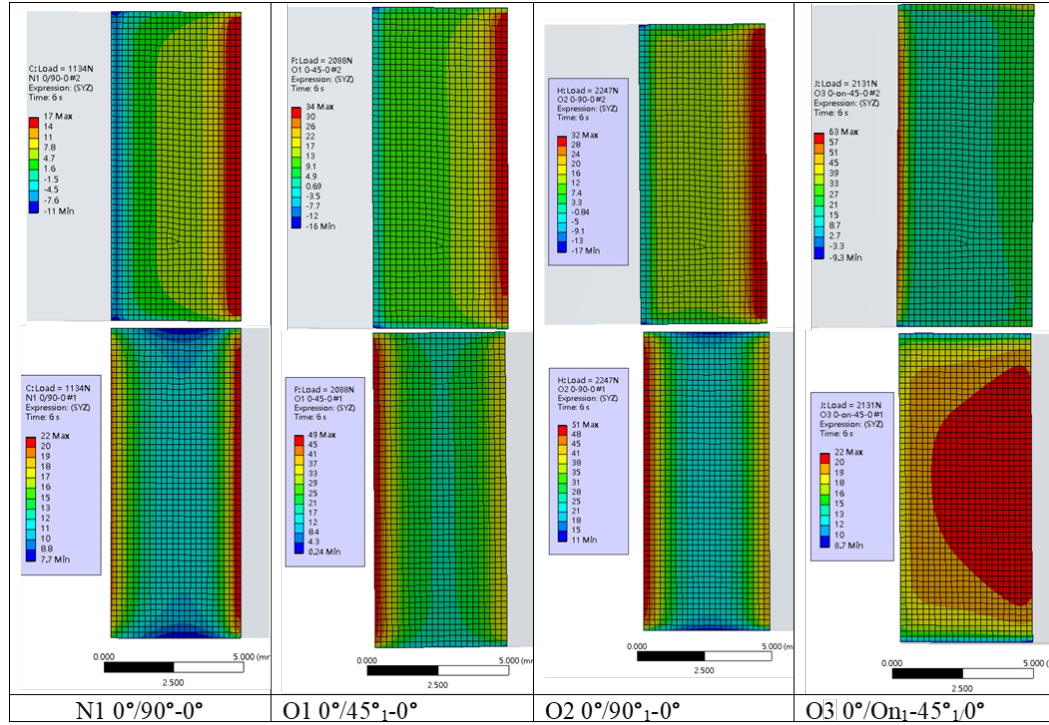


Figure 16. FEA result of shear stress distribution – semi-symmetrical adherends (unit: MPa).

A comparison of the simulated and calculated SLJ ILSS is plotted in **Figure 17**. As the introduction mentions, SLJ failure is a combination of peel, shear, and tensile stresses resulting from the enforced tensile load. A good correlation between the simulated and experimental results can be found when the fracture is caused by shear-dominant stresses. Shear-dominant failure is shown in N1, O1, and O2, for which the simulated average shear stresses at failure are almost identical to the estimated SLJ strength. For configurations where failure was not shear dominant, the calculated SLJ strength based on the average of an evenly distributed shear stress exceeded the simulated average. Examination of the stress components reveals the mixed stress failure behavior on each configuration, either tensile-peel dominant (M2, M4, N2, O3), tensile-shear

dominant (M1, M3, M5, N1, N3), peel-shear dominant (N2, Onyx) or a mixture of the three (O1, O2).

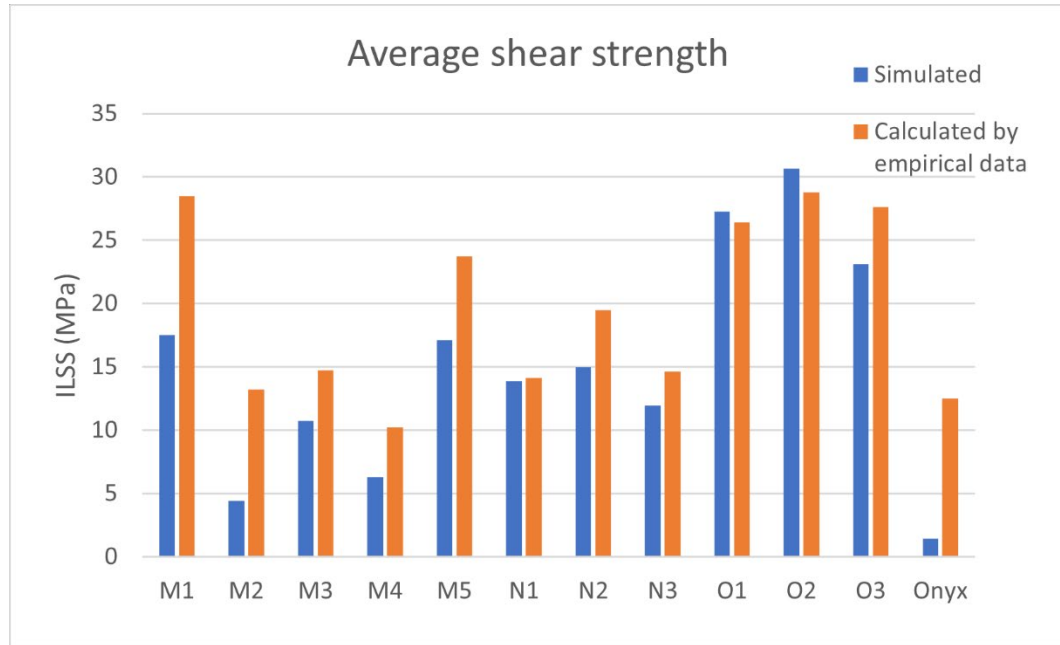


Figure 17. Comparison of calculated and simulated average interlaminar shear stresses.

## CONCLUSIONS

The interlaminar shear strength of FFF composite samples and their failure behaviors were studied. A comparison of the results confirms that for additively manufactured CFRP, the structural inefficiency of the single-lap joint is still severe when the stiffer reinforcement is configured along the lap joint. This results from the peel stress introduced by the asymmetric stiffness, especially when interlaminar stresses are introduced by adjacent dissimilar plies resulting from the stiffness mismatch. This study has provided insight into the performance and primary modes of failure resulting from continuous reinforcement configurations on a 3D-printed functional part. Simply introducing unidirectional reinforcement of  $0^\circ$  increases the SLJ shear strength by more than twofold

compared to the unreinforced Onyx specimens. It is also concluded that the consecutive directional 4-ply reinforcement seems insufficient to bear the off-axis load for the induced risk of delamination and heterogeneous stress distribution. It is recognized that the tested lap strength is a manifestation of a complex stress field for most configurations. The method presented here can be used to determine the interlaminar bonding quality of different 3D-printed reinforced configurations.

Fracture morphologies were identified as a function of the corresponding dominant stress, namely shear, peel, and tensile stresses. It is essential to recognize the mode and to address a proper interpretation of the resulting SLJ stress accordingly. In addition, the structural asymmetry of the lapped bodies is yet another factor that could cause unbalanced flexing. While comparing the lap shear strength of group M and group N, it became evident that the effect of the stiffness of the beam was more significant than the effect of fiber layups between directional plies. It is also found that the additional buffer layer cannot significantly strengthen the single-lap shear strength. Comparison within group O shows the strength differences with the trend of  $90^\circ > \text{Onyx-}45^\circ > 45^\circ$ . The result confirms that the implemented  $45^\circ$  layers are susceptible to composite loading of the shear-peel dominant condition. The trend also confirmed that a  $90^\circ$  layer could compensate for more property mismatch than a  $45^\circ$  layer. Inadequate bonding was identified between the Onyx- $0^\circ$  layer, Onyx- $90^\circ$  layer, and  $45^\circ$ - $45^\circ$  interfaces, as failure occurs in a low load in configurations M2, N2, N3, and B2. For FRPs, fiber layups between a near-symmetrical stiffened beam show a minor effect on the strength.  $45^\circ$  ply is not recommended because of weak inter-bead bonding that negatively affects the structural integrity of the printed composites and induces its susceptibility to shear and peel failure. It

was established that limitations occur when the fulcrum-like edges and free edges cause stress concentration and a low-angle peel force.

This paper has demonstrated that the combination of results from a diversified experimental matrix and FEA simulation approach can provide a path for optimizing and ranking different reinforced AM configurations to achieve the best performance. FEA analysis was used to provide valid stress field information and details related to the failure mode for the AM composites. It is concluded that the load eccentricity can be precisely modeled with semi-implicit static structural FEA and provide relevant information on how the specimens were affected by the vertical stresses (peel stress) introduced by the flexing of the adherends and imbalanced stiffness. The overall trend suggests that characteristic printing pattern configurations can improve AM continuous fiber composite shear strength. Inserting a buffer layer of  $90^\circ$  or Onyx can improve the shear resistance of a unidirectional CFRP. A  $45^\circ$  layer may be included if the part undergoes off-axis direction loading to give a larger strain limit, while a consecutive 4-ply  $45^\circ$  or  $90^\circ$  laminate does not provide desirable strength under the SLJ setup. If applicable, an alternate layup sequence may provide a desired combination of shear strength and strain limit on the structure at the cost of ineffective tensile reinforcement. Examining the loading condition over an AM laminated composite is crucial because the highly nonuniform stress field could create unknown weaknesses if not carefully assessed. It is observed that even without considering the adhesive material in FEA, the stress profile is identical to the classical analytical treatment on the SLJ geometry.

## REFERENCES

1. Ford, S.L. (2014) Additive manufacturing technology: potential implications for US manufacturing competitiveness. *J. Int'l Com. & Econ.*, **6**, 40.
2. ASTM. (2015), ISO / ASTM52900-15, Standard Terminology for Additive Manufacturing – General Principles – Terminology. ASTM International, West Conshohocken, PA. <https://doi.org/10.1520/F3177-21>.
3. Hopkinson, N., Hague, R. and Dickens, P. (2006) *Rapid manufacturing: an industrial revolution for the digital age*. John Wiley & Sons.
4. Ngo, T.D., Kashani, A., Imbalzano, G., Nguyen, K.T.Q. and Hui, D. (2018) Additive manufacturing (3D printing): A review of materials, methods, applications and challenges. *Composites Part B: Engineering*, **143**, 172-196. <https://doi.org/10.1016/j.compositesb.2018.02.012>.
5. Han, P. (2017) Additive Design and Manufacturing of Jet Engine Parts. *Engineering*, **3**, 648-652. <https://doi.org/10.1016/j.Eng.2017.05.017>.
6. Wragg, N.M., Burke, L. and Wilson, S.L. (2019) A critical review of current progress in 3D kidney biomanufacturing: advances, challenges, and recommendations. *Renal Replacement Therapy*, **5**. <https://doi.org/10.1186/s41100-019-0218-7>.
7. Klippstein, H., Diaz De Cerio Sanchez, A., Hassanin, H., Zweiri, Y. and Seneviratne, L. (2018) Fused Deposition Modeling for Unmanned Aerial Vehicles (UAVs): A Review. *Advanced Engineering Materials*, **20**, 1700552. <https://doi.org/10.1002/adem.201700552>.
8. Goh, G.D., Toh, W., Yap, Y.L., Ng, T.Y. and Yeong, W.Y. (2021) Additively manufactured continuous carbon fiber-reinforced thermoplastic for topology optimized unmanned aerial vehicle structures. *Composites Part B: Engineering*, **216**, 108840. <https://doi.org/10.1016/j.compositesb.2021.108840>.
9. Der Klift, F.V., Koga, Y., Todoroki, A., Ueda, M., Hirano, Y. and Matsuzaki, R. (2016) 3D Printing of Continuous Carbon Fibre Reinforced Thermo-Plastic (CFRTP) Tensile Test Specimens. *Open Journal of Composite Materials*, **06**, 18-27. <https://doi.org/10.4236/ojcm.2016.61003>.
10. Melenka, G.W., Cheung, B.K.O., Schofield, J.S., Dawson, M.R. and Carey, J.P. (2016) Evaluation and prediction of the tensile properties of continuous fiber-reinforced 3D printed structures. *Composite Structures*, **153**, 866-875. <https://doi.org/10.1016/j.compstruct.2016.07.018>.

11. Dickson, A.N., Barry, J.N., McDonnell, K.A. and Dowling, D.P. (2017) Fabrication of continuous carbon, glass and Kevlar fibre reinforced polymer composites using additive manufacturing. *Additive Manufacturing*, **16**, 146-152. <https://doi.org/10.1016/j.addma.2017.06.004>.
12. Blok, L.G., Longana, M.L., Yu, H. and Woods, B.K.S. (2018) An investigation into 3D printing of fibre reinforced thermoplastic composites. *Additive Manufacturing*, **22**, 176-186. <https://doi.org/10.1016/j.addma.2018.04.039>.
13. Polyzos, E., Katalagarianakis, A., Polyzos, D., Van Hemelrijck, D. and Pyl, L. (2020) A multi-scale analytical methodology for the prediction of mechanical properties of 3D-printed materials with continuous fibres. *Additive Manufacturing*, **36**, 101394. <https://doi.org/10.1016/j.addma.2020.101394>.
14. van de Werken, N., Tekinalp, H., Khanbolouki, P., Ozcan, S., Williams, A. and Tehrani, M. (2020) Additively manufactured carbon fiber-reinforced composites: State of the art and perspective. *Additive Manufacturing*, **31**, 100962. <https://doi.org/10.1016/j.addma.2019.100962>.
15. Kabir, S.M.F., Mathur, K. and Seyam, A.-F.M. (2020) A critical review on 3D printed continuous fiber-reinforced composites: History, mechanism, materials and properties. *Composite Structures*, **232**, 111476. <https://doi.org/10.1016/j.compstruct.2019.111476>.
16. Iragi, M., Pascual-González, C., Esnaola, A., Lopes, C.S. and Aretxabaleta, L. (2019) Ply and interlaminar behaviours of 3D printed continuous carbon fibre-reinforced thermoplastic laminates; effects of processing conditions and microstructure. *Additive Manufacturing*, **30**, 100884. <https://doi.org/10.1016/j.addma.2019.100884>.
17. A. Gold, S., Strong, R. and N. Turner, B. (2014) A review of melt extrusion additive manufacturing processes: I. Process design and modeling. *Rapid Prototyping Journal*, **20**, 192-204. <https://doi.org/10.1108/rpj-01-2013-0012>.
18. Herakovich, C.T. (2012) Mechanics of composites: A historical review. *Mechanics Research Communications*, **41**, 1-20. <https://doi.org/10.1016/j.mechrescom.2012.01.006>.
19. Chawla, K.K. (2012) *Composite materials: science and engineering*. Springer Science & Business Media.
20. Yavas, D., Zhang, Z., Liu, Q. and Wu, D. (2021) Interlaminar shear behavior of continuous and short carbon fiber reinforced polymer composites fabricated by additive manufacturing. *Composites Part B: Engineering*, **204**, 108460. <https://doi.org/10.1016/j.compositesb.2020.108460>.

21. Yang, C., Tian, X., Liu, T., Cao, Y. and Li, D. (2017) 3D printing for continuous fiber reinforced thermoplastic composites: mechanism and performance. *Rapid Prototyping Journal*, **23**, 209-215. <https://doi.org/10.1108/rpj-08-2015-0098>.
22. Caminero, M.A., Chacón, J.M., García-Moreno, I. and Reverte, J.M. (2018) Interlaminar bonding performance of 3D printed continuous fibre reinforced thermoplastic composites using fused deposition modelling. *Polymer Testing*, **68**, 415-423. <https://doi.org/10.1016/j.polymertesting.2018.04.038>.
23. He, X., Ding, Y., Lei, Z., Welch, S., Zhang, W., Dunn, M. and Yu, K. (2021) 3D printing of continuous fiber-reinforced thermoset composites. *Additive Manufacturing*, **40**, 101921. <https://doi.org/10.1016/j.addma.2021.101921>.
24. Ghiasi, H., Fayazbakhsh, K., Pasini, D. and Lessard, L. (2010) Optimum stacking sequence design of composite materials Part II: Variable stiffness design. *Composite Structures*, **93**, 1-13. <https://doi.org/10.1016/j.compstruct.2010.06.001>.
25. Meyers, M.A. and Chawla, K.K. (2008) *Mechanical behavior of materials*. Cambridge university press.
26. Banea, M.D. and da Silva, L.F. (2009) Adhesively bonded joints in composite materials: an overview. *Proceedings of the Institution of Mechanical Engineers, Part L: Journal of Materials: Design and Applications*, **223**, 1-18.
27. Tsai, M.Y. and Morton, J. (1994) An evaluation of analytical and numerical solutions to the single-lap joint. *International Journal of Solids and Structures*, **31**, 2537-2563. [https://doi.org/10.1016/0020-7683\(94\)90036-1](https://doi.org/10.1016/0020-7683(94)90036-1).
28. ASTM. (2016), D4896-01 Standard Guide for Use of Adhesive-Bonded Single Lap-Joint Specimen Test Results. ASTM International, West Conshohocken, PA. <https://doi.org/10.1520/d4896-01r16>.
29. Goland, M. and Reissner, E. (1944) The stresses in cemented joints.
30. Volkersen, O. (1938) Die Nietkraftverteilung in zugbeanspruchten Nietverbindungen mit konstanten Laschenquerschnitten. *Luftfahrtforschung*, **15**, 41-47.
31. Hart-Smith, L.J. (1973) *Adhesive-bonded single-lap joints*. (No. NASA-CR-112236)
32. da Silva, L.F.M., das Neves, P.J.C., Adams, R.D. and Spelt, J.K. (2009) Analytical models of adhesively bonded joints—Part I: Literature survey. *International Journal of Adhesion and Adhesives*, **29**, 319-330. <https://doi.org/10.1016/j.ijadhadh.2008.06.005>.



33. da Silva, L.F.M., das Neves, P.J.C., Adams, R.D., Wang, A. and Spelt, J.K. (2009) Analytical models of adhesively bonded joints—Part II: Comparative study. *International Journal of Adhesion and Adhesives*, **29**, 331-341. <https://doi.org/10.1016/j.ijadhadh.2008.06.007>.
34. Kendall, K. (1975) Crack propagation in lap shear joints. *Journal of Physics D: Applied Physics*, **8**, 512.
35. Kupski, J., Teixeira de Freitas, S., Zarouchas, D., Camanho, P.P. and Benedictus, R. (2019) Composite layup effect on the failure mechanism of single lap bonded joints. *Composite Structures*, **217**, 14-26. <https://doi.org/10.1016/j.compstruct.2019.02.093>.
36. Kupski, J., Teixeira de Freitas, S., Zarouchas, D. and Benedictus, R. (2020) On the influence of overlap topology on the tensile strength of composite bonded joints: Single overlap versus overlap stacking. *International Journal of Adhesion and Adhesives*, 102696. <https://doi.org/10.1016/j.ijadhadh.2020.102696>.
37. Peng, X., Zhang, M., Guo, Z., Sang, L. and Hou, W. (2020) Investigation of processing parameters on tensile performance for FDM-printed carbon fiber reinforced polyamide 6 composites. *Composites Communications*, **22**, 100478. <https://doi.org/10.1016/j.coco.2020.100478>.
38. Kovan, V., Altan, G. and Topal, E.S. (2017) Effect of layer thickness and print orientation on strength of 3D printed and adhesively bonded single lap joints. *Journal of Mechanical Science and Technology*, **31**, 2197-2201.
39. Falck, R., Goushegir, S.M., dos Santos, J.F. and Amancio-Filho, S.T. (2018) AddJoining: A novel additive manufacturing approach for layered metal-polymer hybrid structures. *Materials Letters*, **217**, 211-214. <https://doi.org/10.1016/j.matlet.2018.01.021>.
40. Parandoush, P., Tucker, L., Zhou, C. and Lin, D. (2017) Laser assisted additive manufacturing of continuous fiber reinforced thermoplastic composites. *Materials & Design*, **131**, 186-195. <https://doi.org/10.1016/j.matdes.2017.06.013>.
41. da Silva, L.F.M. and Campilho, R.D.S.G. (2012) Advances in Numerical Modelling of Adhesive Joints. 1-93. [https://doi.org/10.1007/978-3-642-23608-2\\_1](https://doi.org/10.1007/978-3-642-23608-2_1).
42. ASTM. (2014), Standard D3165-07 *Standard test method for strength properties of adhesives in shear by tension loading of single-lap-joint laminated assemblies*. ASTM International, West Conshohocken, PA. <https://doi.org/10.1520/D3165-00>.
43. ASTM. (2004), Standard D1002-01 *Standard Test Method for Apparent Shear Strength of Single-Lap-Joint Adhesively Bonded Metal Specimens by Tension*

*Loading (Metalto-Metal)*. ASTM International, West Conshohocken, PA.  
<https://doi.org/10.1520/D1002-01>.

44. ASTM. (2012), Standard D5573 Standard practice for classifying failure modes in fiber-reinforced-plastic (FRP) joints. ASTM International, West Conshohocken, PA, Vol. 15, pp. 2002. <https://doi.org/10.1520/D5573-99R19>.
45. Reddy, J. and Robbins Jr, D. (1994) Theories and computational models for composite laminates.
46. Hart-Smith, L. (2002) Expanding the capabilities of the Ten-Percent Rule for predicting the strength of fibre-polymer composites. *Composites science and technology*, **62**, 1515-1544. [https://doi.org/10.1016/S0266-3538\(02\)00092-1](https://doi.org/10.1016/S0266-3538(02)00092-1).
47. Díaz, J., Romera, L., Hernández, S. and Baldomir, A. (2010) Benchmarking of three-dimensional finite element models of CFRP single-lap bonded joints. *International Journal of Adhesion and Adhesives*, **30**, 178-189. <https://doi.org/10.1016/j.ijadhadh.2009.12.005>.
48. Silva, M.R.G., Marques, E.A.S. and Silva, L.F.M.d. (2016) Behaviour under Impact of Mixed Adhesive Joints for the Automotive Industry. *Latin American Journal of Solids and Structures*, **13**, 835-853. <https://doi.org/10.1590/1679-78252762>.
49. Marques, E.A.S., da Silva, L.F.M. and Flaviani, M. (2015) Testing and simulation of mixed adhesive joints for aerospace applications. *Composites Part B: Engineering*, **74**, 123-130. <https://doi.org/10.1016/j.compositesb.2015.01.005>.
50. Pipes, R.B. and Pagano, N. (1994), *Mechanics of composite materials*. Springer, pp. 234-245.
51. ANSYS, I. (2020) *ANSYS Mechanical APDL*, Release 2020 R1, Help system, Theory Reference.

COMPARISON OF MECHANICAL BEHAVIORS OF FLEXURAL AND MODE I  
FRACTURE ON ADDITIVELY MANUFACTURED CONTINUOUS  
FIBER-REINFORCED THERMOPLASTIC COMPOSITES

by

YU-CHAO SHIH, SUBHAYU SEN, SELVUM PILLAY, AND HAIBIN NING

In preparation for *Additive Manufacturing*

Format adapted for dissertation.

## ABSTRACT

Fiber-reinforced plastic (FRP) composite structures produced via additive manufacturing (AM) offer excellent mechanical properties and unprecedented design freedom for research and development of lightweight aeronautic components. However, it is challenging to determine their structural integrity during the components' lifecycle, which could factor into the cost structure and jeopardize its proclaimed benefits. Multiple failure modes can be observed due to the combined anisotropy resulting from the FRP's anisotropic properties and the mesostructured defects from AM's layer-by-layer process. The mechanical behaviors of AM-made FRP are determined by the interfacial bonding between constituents and their interlaminar interfaces. Characterization of bonding qualities between layers in AM-made FRP is crucial in quantifying the effect of parameters in manufacturing processes to achieve higher mechanical properties. Structural integrity can typically be assessed with fracture mechanics studies, based on which the damage tolerance of a system undergoing specific load can be evaluated with material and geometry-specific parameters, both available empirically or analytically. The mode I fracture toughness is frequently used to quantify the interfacial bonding quality for their resistance to crack propagation when the pre-existing crack undergoes perpendicular opening load. Empirical characterization of mode I fracture toughness for laminated structure uses double cantilever beam (DCB) samples with data reduction schemes derived by simple beam analysis. Extensive beam flexure can occur, and the accumulated deviation from the analysis can be accounted for by introducing an associated correction factor.

In this study, the mechanical responses of additively manufactured fiber-reinforced plastic (AMFRP) composites with various fiber contents were characterized and

compared. Mode I fracture and flexural responses were characterized, and the process-structure-property relationship was evaluated using three-point bending and double cantilever beam (DCB) testing. The fluctuation of propagation fracture toughness manifests the occurrence of fracture incidents during the beam flexure. Different failure modes were identified using microscopic images to relate the material morphologies and the stagewise decohesion to the mechanical responses. The results were compiled and reported to guide practical design and prevent premature material failure.

## INTRODUCTION

Material failure is a phenomenon that occurs when materials undergo a multiscale decohesion in molecular bonding by external or internal driving energies within material phases, both of which result in loss of load-bearing properties [1]. Evolution and nucleation of voids and defects are believed to be the first principal phenomenon that governs the structural failure of the materials [2-4], which can be solved analytically on a microscopic scale with respect to the matter's morphologies. However, a deviation between the prediction of material responses from analytical molecular models and the mechanical responses of a bulk object are magnitudes away. There is active research to bridge the gaps between theoretical energy balance and physics-based mechanistic models [4]. Fracture mechanics [2,5,6] was first recognized by Griffith's pioneering work on linear elastic fracture mechanics (LEFM), conceptualized by Irwin and Rice, coming to be of engineering usefulness and formalized as an essential tool in structural integrity assessment. In short, fracture mechanics aim to find a practical approximation of characterizable material constants using an intermediate approach combining assumptions of a mechanistic model and a pan-thermodynamics energy balance at a topological level. The fracture mechanics approach aims to resolve difficulties in the characterization of geometry- and material-dependence conditions with practical characterizable parameters to be used in assessing structural integrity [6]. Although most of the tools developed within practical fracture mechanics are based on linear elastic materials systems, implementing such tools for failure analysis on objects with systematic anisotropy proves helpful in practicality [6] with proper correction factors incorporated.

Determination of the fracture properties is crucial for structural validation on the engineering materials used, providing a lower limit of mechanical failure threshold, as opposed to the upper limit prescribed by the failure criteria of monotonic strength. Two material properties for quantifiable fracture resistance are referred to as fracture toughness: strain energy release rate,  $G$ , and stress intensity factor,  $K$ . The two essential fracture parameters were widely used in engineering practice to assess the structural integrity and determine the components' damage tolerance at prescribed loading conditions. Empirical characterization of the fracture toughness is based on LEFM using the energy conservation assumptions with continuum mechanics models such as beam theorem and plate theorem. The mode I fracture toughness can be used to calculate the residual load-bearing capability of a structure with a pre-existing crack undergoing an opening mode and can be characterized by a variety of techniques, such as compact tension (CT), single-edge notched bending (SEB) [3,6], and double cantilever beam [7] (DCB). DCB is popular in testing laminated fiber-reinforced plastic (FRP) composite plates as prescribed by ASTM D5528 to quantify the interlaminar bonding [8], considering structural anisotropy. Multiple correction factors were proposed and implemented to account for the coupling effect from the change of boundary conditions due to bending and rotation of the arm [9-12].

Continuous fiber-reinforced plastic (CFRP) composites are well known to have high specific strength, adequate toughness, and outstanding environmental resistance [13,14], combining the advantages of highly aligned fibrous materials and tough polymeric matrices. As a result, CFRP composites are competitive in applications across transportation, sporting goods, and energy industries as reliable structural components.

The composite is also economical and efficient because of the low maintenance cost throughout the operational life cycle of the product. An increasing trend was observed in the interest of analysis in FRP made of modular additive manufacturing (AM) technologies, citing its capability to enable functional prototyping to small-batch production with lower cost and higher throughput. The design and applications for AM-made FRP are used for various applications in energy, aerospace, defense, and automobile industries to meet the performance demand on strength, modulus, and environmental durability [15]. AM object's structural integrity and reliability assessment are paramount as the cost structure has to include the safety evaluation, cycle of operations, and disposal of decommissioned components. Design for additive manufacturing (DfAM) is an emerging field of research aiming to develop an efficient workflow to produce high-performance objects by additive manufacturing to innovate structural design, enable novel materials, and build objects otherwise impossible to build [16-19]. The principle of DfAM also promotes sustainable engineering and manufacturing, requiring the realization of resource and waste management with respect to the use of reliable structural integrity assessment and the 3R – reduce, recycle, and reuse. The decision to replace a component relies on the knowledge-based failure criteria for each possible failure mode, including interfacial debonding, matrix cracking, interlaminar or intralaminar decohesion, and fiber breakage. In laminated composites, interlaminar delamination can be detrimental to their structural performance as premature failure can occur when they undergo drastic load or impact due to their anisotropic property [20].

Efforts to quantify the interlaminar bonding in AM-made FRP using a fracture mechanics approach are well-documented [21-35]. The morphology of the extruded



materials is influenced by procedural parameters, resulting in different failure mechanisms compared to conventional parts. The mechanical behavior of FRP made of extrusion-based additive manufacturing (EBAM) technology can be affected by many factors. EBAM features a sturdy mechanical architecture, ease of maintenance, and broad compatibility with materials selection [36,37], while the product is also susceptible to delamination-type failure identical to laminated composites. The multiscale anisotropy on additively manufactured fiber-reinforced plastic composites can be categorized in the form of interfaces, including fiber-matrix, intralayer in-between raster, interlaminar regions, wall-infill, and geometric-induced discontinuities.

This research investigated the mechanical responses of 3D-printed FRP composite beams with three-point bending and double cantilever beam (DCB) tests. Flexural samples were designed to understand the AM-made CFRP's flexural responses and their correlation to the fiber fraction. Six DCB samples for carbon-carbon and glass-glass interface were designed, manufactured, and tested using an alternative precrack method to improve geometrical symmetry. Three variants of beams were developed for each interface type to evaluate the effects of different bending stiffness on the mode I fracture toughness  $G_{IC}$ . Flexural responses were compiled, and a minimal effective reinforcing fiber fraction was given. The evolution of strain energy release rate directly manifests the significance of the compositional difference of the beam within each interface type with high in-group variability, indicating that incidental fracture propagation  $G_{IC}$  is geometry-specific as opposed to the geometry-independence initial  $G_{IC}$ .

## METHODOLOGY

### Material and Equipment

All CFRP samples were manufactured using an extrusion-based desktop 3D printer, the Mark Two (by Markforged, MA, USA). The Mark Two printer has an extrusion hot end equipped with two nozzles, one for printing a discontinuous fiber composite and the other one for a continuous fiber composite. The closed-source nature of the Mark Two provides convenience for functional prototyping without parameter tryouts at the expense of inadaptability to third-party materials that require alternative parameters. All geometries were designed in Solidworks 2023 regarding the required geometry for each mechanical test and subsequently submitted to the cloud-slicing software Eiger to configure the printing parameters. An mfp file extension format was then generated to fabricate the FRP composites. A polyamide-based thermoplastic, with the tradename Onyx, was the discontinuous carbon fiber composite material used to fabricate all samples. The Onyx was a proprietary polyamide blend reinforced with a 10% volume fraction of chopped carbon fiber [38]. Two reinforcement materials, i.e., continuous carbon fiber (CCF) filament and high-strength-high-temperature glass fiber (HSHTG) filament, were used for reinforcement. The CFRP feedstocks were reported to be pre-impregnated thermoplastic composite filaments with around 25-35% fiber volume fraction (FVF) [15-20] and a polyamide matrix. The void content of 3D-printed CFRP with a setup of 100%-infilled was reported to be around 7-15% [28,32,39,40], resulting from ununiform cooling and unfilled volume. The specifications for the machine and materials used in this research are

outlined in **Table 1**. All samples were printed in the x-y direction as ISO/ASTM 52900 specified [41].

Table 1. Materials specifications used in this research.

<b>Materials</b>	<b>Type</b>	<b>Properties</b>
Onyx Filament (Onyx)	Polyamide 6-based thermoplastic with chopped carbon fiber reinforcement	$E_T = 2.4 \text{ GPa}$ $\rho = 1.2 \text{ g/cm}^3$ FVF = 10%
Continuous carbon fiber Filament (CCF)	Pre-impregnated continuous carbon fiber	$E_T = 60 \text{ GPa}$ $\rho = 1.4 \text{ g/cm}^3$ FVF = 30%
High-strength-high-temperature glass filament (HSHTG)	Pre-impregnated continuous glass fiber	$E_T = 21 \text{ GPa}$ $\rho = 1.5 \text{ g/cm}^3$ FVF = 30%
Note: * Nomenclature: $E_T$ : Tensile modulus, $\rho$ : Density, both from manufacturer's data [42]. * FVF: Fiber volume fraction, from [43]. * All materials were supplied by Markforged Inc., MA, USA.		

## Sample Configurations and Characteristics

### *Flexural samples*

The three-point bending samples were printed according to procedure A from ASTM D790 - standard test methods for flexural properties of unreinforced and reinforced plastics and electrical insulating materials [44]. The dimension of the sample is set with a length (L) of 35 mm, a width (b) of 12.5 mm, and a depth (d) of 2 mm, which results in a span-to-depth ratio greater than the recommended 16:1, according to the standard [44]. The engineering drawing and illustration of the flexural behavior are shown in **Figure 1**. The instantaneous load,  $P_i$ , and the instantaneous deflection,  $D_i$ , are recorded for further analysis.

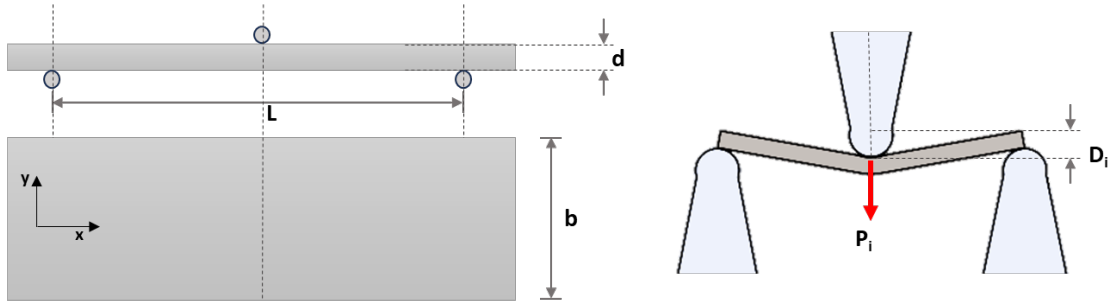


Figure 1. Engineering drawing of the three-point-bending test and schematics.

Sample configurations were designed as outlined below in **Table 2** to investigate the effect of fiber percentage on the resulting flexural responses. The proportionality of fiber composite filament in cross-sectional was used to denote the volume percentage using continuous filament fraction (CFF) content, calculated using the equation adapted from [45,46], as below:

$$CFF \text{ Content} = \frac{\text{depth of fiber layers} \times \text{width of fiber layers}}{\text{depth of sample} \times \text{width of sample}} = \frac{(t \times N_f) \times (b - 0.4 \times N_w)}{d \times b} \quad (1)$$

in which  $t$  is the layer height on each deposited layer,  $N_f$  is the number of continuous layers,  $N_w$  is the number of walls count, and 0.4 mm is the thickness of the walls bounded by nozzle diameter. The  $0^\circ$  direction reinforcement fiber was aligned along the  $x$  direction as specified in **Figure 1**.

Table 2. Designed configurations of all three-point bending flexural samples.

Configuration	Layer height, $t$ (mm)	Reinforcement			Wall Thickness (mm) (Count $N_w$ x 0.4 mm)	Cross-sectional continuous fiber filament (CFF) content
		Type	Layer counts for Onyx Floor/Roof	Fiber Lay-out		

On	Onyx	0.125	Matrix	4	$[\pm 45]_s$	$4 \times 0.4 = 1.6$	0%
CF#1	CCF	0.125	CCF	4	$[0]_8$	$4 \times 0.4 = 1.6$	44%
CF#2	CCF	0.125	CCF	2	$[0]_{12}$	$4 \times 0.4 = 1.6$	65%
CF#3	CCF	0.125	CCF	1	$[0]_{14}$	$2 \times 0.4 = 0.8$	82%
GF#1	HSHTG	0.1	HSHTG	4	$[0]_{12}$	$4 \times 0.4 = 1.6$	52%
GF#2	HSHTG	0.1	HSHTG	2	$[0]_{16}$	$4 \times 0.4 = 1.6$	70%
GF#3	HSHTG	0.1	HSHTG	1	$[0]_{18}$	$2 \times 0.4 = 0.8$	82%

FVF is the primary variable between samples to find a correlation between the material's flexural modulus and strength. For clarity, the FVF content is a volume fraction of continuous fiber, which is commonly simplified with the areal proportionality of continuous fiber in a cross-sectional area. In this work, CCF was defined as the fractional content of the continuous filament used. A conversion of the CFF content to FVF content ( $\text{CFF} = \text{FVF} \times 30\%$ ) was made regarding the literature value reported in the last section [43].

#### *DCB samples*

Double cantilever beam samples were designed to characterize the mode I fracture toughness of AMFRP composites for CCF-CCF interfaces and HSHTG-HSHTG interfaces and their variation under different beam compositions. The engineering drawing, dimension details, and schematic representation of the DCB test are shown in **Figure 2**. Symmetric flexural rigidity of the bending arms was ensured to avoid complex mixed-mode bending induced by the tilted beam, as suggested in [23,47], which could introduce

the non-negligible  $G_{II}$  term during the data reduction. A 3 mm thickness was selected to avoid excessive fiber bridging between the laminae.

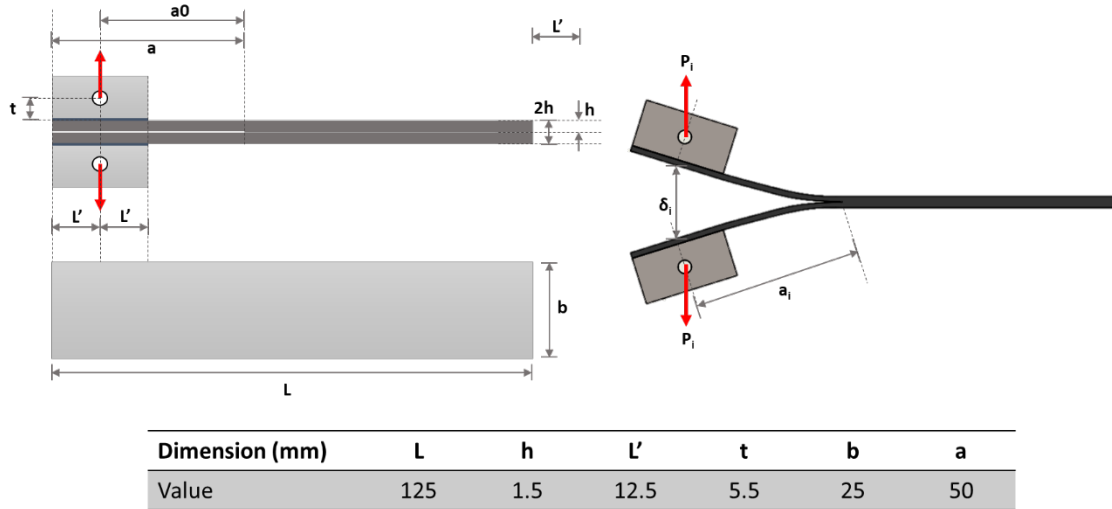


Figure 2. Engineering drawing of the double cantilever beam sample and schematics.

Each CCF beam comprised 24 layers of 0.125 mm thick layers, as opposed to 30 layers of 0.1 mm thick layers for HSHT glass specimens, both resulting in two arms of 1.5 mm thickness undergoing loading. A preliminary trial was conducted using a nonadhesive insert as suggested by the ASTM standard and literature. However, the unbalanced flexural rigidity from the artifacts introduced by the printing procedure causes nonuniform mixed-mode bending. Alternatively, a mold release solution, Loctite Freekote 770-NC, was used to introduce the precrack over the central surfaces. Printing was paused once the lower half of the layer was finished to allow 770-NC to be applied on the desired separation interfacial surface. A tweezer was used to apply a thin layer of the mold release from a slightly dipped quadri-folded laboratory wipe. A proper time interval between each application was timed to allow the solution to dry fully to form a thin layer. The print was then resumed until the desired sample thickness was reached. The mold

release solution was also applied on the interfaces between unwanted bottom Onyx layers for easy removal. The use of the method can prevent a tilted opening resulting from the artifacts that make flexural rigidity asymmetric.

All sample configurations are listed in **Table 3**. The number of reinforcing continuous fiber composite layers was used as an additional parameter to create sample variants for the evaluation of the effect of beam stiffness differences. Concisely, we want to verify that the approximated  $G_{IC}$  and the associated elastic constant calculated by simplified analysis prescribed by LEFM are adequately correlated. The CFF content was calculated using **Equation 1**. One side of the wall was also removed to overcome side wall detachment for some configurations, specifically the 12C and 15G samples that do not have an Onyx enclosure on the upper and bottom surfaces to maintain structural integrity, while the other was retained. One side of the samples was coated with correction fluid, a  $TiO_2$ -based opacifying suspension fluid, to create a thin layer of contrast for observation and marked with a black marker on each 1 mm length on the first 10 mm, 5 mm length on the rest of the sample for easy observation of the crack propagation, as suggested in ASTM D5528.

Table 3. Designed double cantilever beam samples and associated beam compositions.

Configura- tion	Layer height, t (mm)	Reinforcement			Cross-sec- tional con- tinuous fi- ber filament (CFF) con- tent	Longitudi- nal elastic constant (GPa)
		Type	Layer counts for Onyx Wall/Roof, $N_r$	Fiber Layout of a sin- gle can- tilever		
CCF-8C	0.125	CCF	4	$[0]_8$	62.4%	34.8
CCF-10C	0.125	CCF	2	$[0]_{10}$	78.0%	43.2
CCF-12C	0.125	CCF	0	$[0]_{12}$	93.6%	66

HSHTG-10HG	0.1	HSHTG	4	[0] <sub>10</sub>	62.4%	11.5
HSHTG-12HG	0.1	HSHTG	2	[0] <sub>12</sub>	74.9%	13.2
HSHTG-15HG	0.1	HSHTG	0	[0] <sub>15</sub>	93.6%	21
Properties below were used for calculation: Onyx: E= 1.26 GPa, CCF: E= 66 GPa, HSHTG: E= 21 GPa (From the literature [39] and manufacturer's datasheet)						

### Mechanical Testing

Both mechanical tests were conducted using an Instron 1331 system with a 22kN force load cell and a suitable testing fixture prescribed by associated ASTM standards.

The machine is equipped with the capability to record data at a frequency of 100 Hz.

#### *Flexural tests*

Three samples were printed for each configuration to verify the statistical significance and to reduce error. A proper fixture with a 5 mm diameter nose, as required by ASTM D790, was used for all the three-point bending tests, as shown in **Figure 1**. The samples were marked on the edges of the support span and the center line to ensure that they were aligned with the loading fixture and that the loading was applied correctly. The load-deflection (Pi, Di) data were collected for further analysis of flexural properties. Based on the ASTM D790 formulation, a proper load speed is to be calculated as:

$$R = \frac{ZL^2}{6d} \quad (2)$$

in which L is the length of the support span, d is the depth of the beam, and Z is the straining rate. After plugging in the desired straining rate  $Z = 0.01$  mm/mm per minute,  $L = 35$  mm,  $d = 2$  mm, the crosshead rate was calculated to be 1 mm per minute.

The experiment followed the ASTM D790 procedure A, which is only applicable to the



limited strain of 5% in determining flexural strength, and the allowable midspan deflection  $D$  was calculated according to the equation below:

$$D = \frac{rL^2}{6d} \quad (3)$$

in which  $r$  is the strain limit of 5%,  $L$  is the span length, and  $d$  is the span depth.

Based on the sample dimension used, the calculation shows that a valid data reduction for flexural properties is within the deflection range until a maximum of 5.1 mm concerning the sample dimension.

#### *DCB tests*

All DCB samples were opened carefully with a thin blade to ensure the crack followed the prescribed middle interface before each test. The sample was then bonded with a loading block using Loctite 414 over the AMFRP surface and Loctite 496 on the loading block to create a thin buffer layer on both surfaces. Two adhesive layers were then bonded with compression for at least 30 minutes to ensure enough strength to withstand the tensile and rotational loading. All samples were first loaded onto the fixture for a precrack stage until a 50 mm uncorrected precrack was reached. Afterward, the sample was unloaded from the first precrack procedure to the original position and reloaded until failure. Tests were recorded with multiple moving microscopes, and the video was synced with the data retrieved from the tensile tester with the open-source software OBS Studio. Traction length was monitored and documented to correlate to the machine-logged opening load and separation displacement. Two moving microscopes, namely the Dino-Lite 0.8 MP and the Jiusion endoscope up to 1000x magnification, were used to record the crack opening with a moving fixture that has mobility in both X- and Z- directions for crack propagation and longitudinal loading, respectively. A horizontal free end, which

indicates a proper load transfer toward the crack front from the central plane, is expected for a valid test, and incidents of undesired responses, such as asymmetric opening or flexural failure of the beam, were recorded and analyzed separately. The fixture to apply tensile load and the recorder setup for crack length acquisition are shown in **Figure 3a** and **Figure 3b**, respectively.

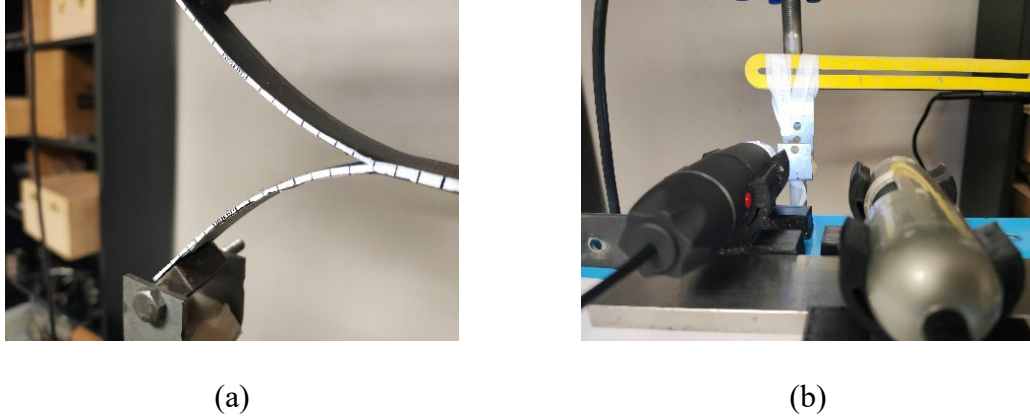


Figure 3. (a) Testing fixture and load blocks for DCB test, (b) the moving microscope recording DCB test.

#### *Data Reduction*

The flexural data were recorded in pairs of (deflection  $D_i$ , load  $P_i$ ) and processed regarding ASTM D790 for the flexural modulus and flexural strength of three-point bending tests following the equations below:

$$\varepsilon_f = \frac{6Dd}{L^2} \quad (4)$$

$$\sigma_f = \frac{3PL}{2bd^2} \quad (5)$$

$$E_B = \frac{L^3m}{4bd^3} \quad (6)$$

in which  $\varepsilon_f$  is outer-surface strain,  $\sigma_f$  is flexural stress,  $P$  is the load at a given data point,  $E_B$  is the flexural modulus, and  $m$  is the slope of the tangent to the initial linear portion of the load-deflection curve [44]. Data were also processed using statistics recommended by ASTM D790 to assess variation and significance between groups. The data of three-point bending serves as a baseline reference for DCB testing to determine the flexural rigidity and responses of the 3D-printed beam, as the LEFM formulations also utilize a simple beam analysis. In order to calculate the  $G_{IC}$  for FRP using LEFM formulations, various corrections were implemented to account for the geometrical nonlinearity.

Three parameters were recorded for the DCB tests - load  $P_i$ , displacement  $\delta_i$ , and the crack length  $a_i$ . The modified beam theorem (MBT) was chosen as the data reduction to calculate mode I fracture toughness based on a displacement method [12]. The MBT is based on a simple beam theorem with several corrections and simplifications. The mode I strain energy release rate based on Irwin-Kiels equation is written as:

$$G_{IC} = \frac{P^2}{2b} \frac{dC}{da} \quad (7)$$

in which  $P$  is the load,  $b$  is the width,  $C$  is the compliance, and  $a$  is the crack length. The compliance  $C$  can be calculated from a simple beam theory by:

$$C = \frac{\delta}{P} = \frac{2a^3}{3EI} = \frac{8a^3}{bEh^3} \rightarrow \frac{dC}{da} = \frac{2a^2}{EI} \quad (8)$$

for which  $E$  is the axial modulus, and  $I$  is the second moment of area. For a rectangular beam  $I = bh^3/12$ , after plugging in equation 8 in equation 7, we get:

$$G_{IC} = \frac{P^2}{2b} \times \left( \frac{2a^2}{EI} \right) = \frac{P^2 a^2}{bEI} = \frac{3P\delta}{2ba} \quad (9)$$

Further derivation of some of the corrections can be found in [9-11]. The full MBT formulation is:

$$G_{IC} = \frac{3P_i\delta_i}{2b(a_i + |\Delta|)} \cdot \left(\frac{F_i}{N_i}\right), \text{ which } \left\{ \begin{array}{l} P_i = \text{load} \\ \delta_i = \text{load point displacement} \\ b = \text{specimen width} \\ a_i = \text{delamination length} \\ \Delta = \text{Crack length correction} \\ F_i = \text{Correction for large displacement} \\ N_i = \text{Correction of rotation} \end{array} \right. \quad (10)$$

which would result in a series of  $G_{ICs}$  throughout the crack propagation process. According to the specification from ASTM D5528, proper corrections should be made to account for the beam's flexure, end-block rotation, effect of the elastic foundation for the fracture process zone, and the toughening effects [6,11]. The crack length correction parameters were introduced to offset the nonlinear effect imposed by the load block rotation and stiffening as suggested by ASTM D5528:

$$F = 1 - \frac{1}{10} \left(\frac{\delta}{a}\right)^2 - \frac{3}{2} \left(\frac{\delta t}{a^2}\right)^2 \quad (11)$$

$$N = 1 - \left(\frac{L'}{a}\right)^3 - \frac{9}{8} \left[1 - \left(\frac{L'}{a}\right)^2\right] \left(\frac{\delta t}{a^2}\right) - \frac{9}{35} \left(\frac{\delta}{a}\right)^2 \quad (12)$$

in which F and N are used to correct for the rotation of the loading block and large displacement [9,12]. An investigation of the deviation of the centroid of the flexural rigidity within the arms shows a negligible difference in the calculated  $G_{IC}$  (<1%). Therefore, correction for this effect is not needed in this case by changing the formulation of t, replacing the distance between the load block bond line and the centroid of flexural rigidity from 0.75 mm to 1 mm, 0.875 mm, and 0.9 mm for 8C/10G, 10C, and 12G,

respectively. The crack length  $[a_i]$  was replaced by  $[a_i+|\Delta|]$ , in which  $|\Delta|$  was calculated as the absolute of the x-intercept using a least-square-plot of the cube root of the compliance  $C$  as a function of delamination length  $a_i$ . Results calculated from the other methods listed in ASTM D5528 were also analyzed but not reported to avoid redundancy, as the result indicates no significant deviations. The initial mode I fracture toughness can be found with a nonlinearity point in the load-displacement curve (NL), a 5% offset intersection (5%), or a visible crack onset (VIS). Due to the consistency and conservative nature of the NL method, it is used to analyze the fracture toughness in this study. The evolution of flexural modulus can be monitored with the following equation to identify flaws and anomalies:

$$E_{if} = \frac{64(a+|\Delta|)^3 P}{\delta b h^3} \left( \frac{1}{N} \right) \quad (13)$$

## RESULT AND DISCUSSION

### Flexural Test Result

The flexural properties of AMFRP samples were compiled in **Figure 4**. The flexural modulus and strength both show a positive correlation with higher CFF content. Due to the non-monotonic stress composition that is constituted by shear, compression, and tension within the stress field, the lower flexural modulus compared to the tensile modulus was observed as expected. The flexural stress-strain curves for both CCF and HSHTG samples are shown in **Figure 5**. CCF samples were observed with a multi-stage load drop, possibly caused by stagewise decohesion from lamina failure throughout the flexure. The first load drop is a direct manifestation of in-plane shear failure caused by

delamination, evident by the following plateau region of plastic yielding enabled by the layer-by-layer construct and the stochastic void distribution. The second and following load drops showcase the catastrophic lamina failure, likely initiated by the failure of the uppermost CCF layer by a combination of compression, flexure, and in-plane shear. In contrast, no load drops were observed in the flexural response of HSHTG samples, indicating that HSHTG is less susceptible to delamination and has a higher strain limit than the CCF. A plateau of plastic deformation was also observed in the HSHTG groups as an indication of materials yielding and stagewise hardening caused by densification between the layers. The oscillation of the flexural responses also comes with the geometrical change induced by the three-point bending design.

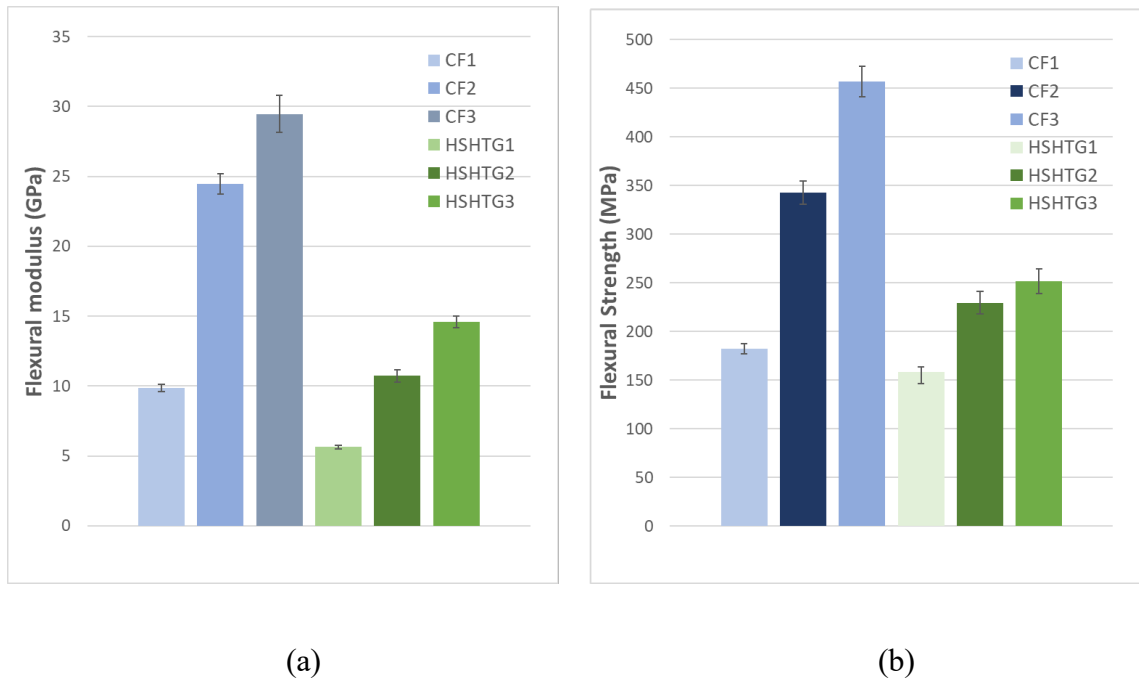


Figure 4. Flexural (a) modulus and (b) strength for CCF and HSHTG samples.

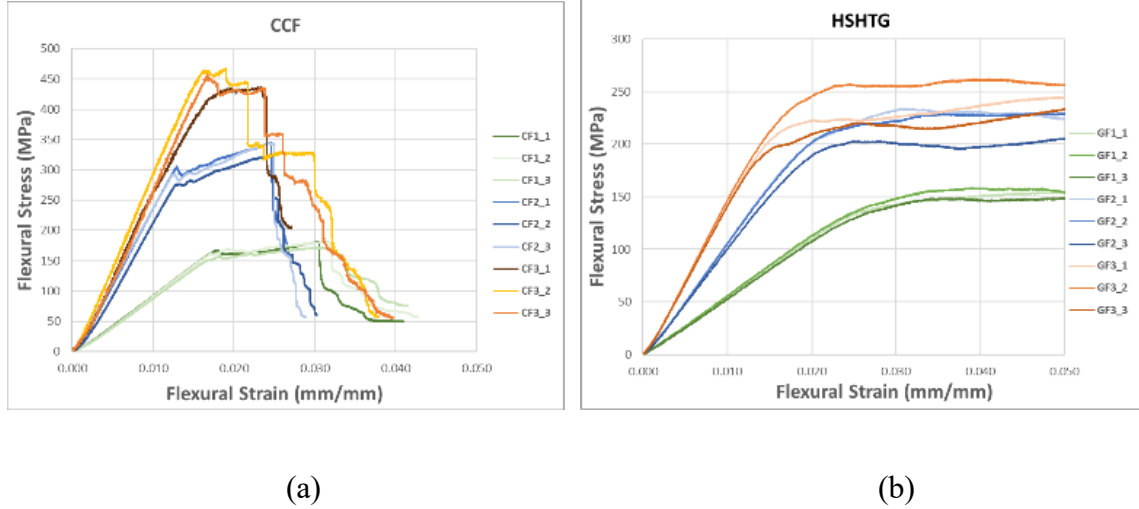


Figure 5. Flexural stress-strain curve for (a) CCF and (b) HSHTG samples.

To establish the correlation between flexural modulus and the CFF content, data from this study were graphed with available values from the literature in **Figure 6**. A proportional increase of the flexural modulus with a higher CFF content is evident. A similar graph was not constructed to compare flexural strength as variations of compared results can be of different geometry that were not comparable. The stiffness of a 3D-printed composite beam can be associated with the interlaminar properties when the bending equation does not consider compression over the surface, interlaminar shear over the mid surface of beams, and tensile extensional load on the bottom surfaces.

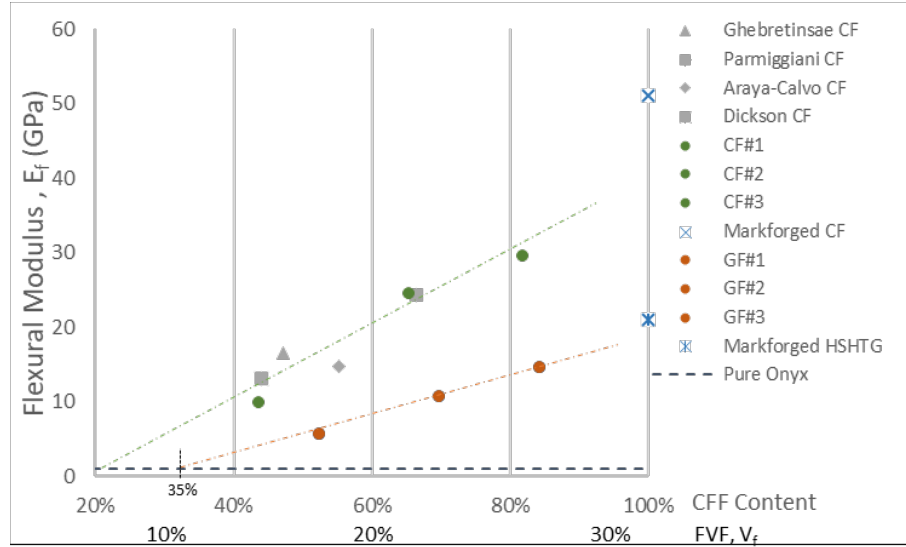


Figure 6. Flexural modulus to CFF content relationship with available data from the literature. [48-51]

An extrapolation of the CCF and HSHTG data shows an effective reinforcing effect in flexural modulus with a minimum CFF content for 20% CCF or 35% HSHTG. However, the added continuous reinforcement can also introduce additional failure modes between interfaces and laminae. Therefore, considerations on using a minimum CCF need not be of strengthening effect for a higher failure strength. The prediction is valid for composite beams with symmetrical fiber layout through the thickness direction of the 3D-printed composites, with at least one wall enclosure to preserve the structural integrity. A second axis is constructed below the CFF content for convenience to compare the performance of conventional FRP composites, using an estimated 30% FVF for both CFF and HSHTG, as stated in the literature. Compared to the conventional CFRP composites, the strain limit for flexure of 3D-printed CFRP has a much higher capacity, resulting from the elastoplastic matrix, the voids that act as plasticizers, and a much lower FVF. However, the performance of the 3D-printed CFRP is also limited by a maximum of 30-35%



FVF, as prescribed by the raw filament feedstock, showing an upper limit of around 50% of the flexural properties compared to a 50-60% FVF conventional continuous FRP [52].

### Result of Mode I Fracture Toughness

A compilation of the characterized mode I fracture toughness between the 3D-printed CF-CF and HSHTG-HSHTG interfaces is shown in **Figure 7**. Initial fracture toughness of 1015 J/m<sup>2</sup> and 1100 J/m<sup>2</sup> were consistent for CCF and HSHTG samples, regardless of the differences in flexural rigidity by configurations. It was found that there was a lower deviation in the initial fracture toughness on 8C samples compared to 10C and 12C. Conversely, the HSHTG samples display a reversed trend with a steadier crack initiation on 15G than the others. The average  $G_{IC}$  values were retrieved without cycles of loading-unloading between each data, resulting in a pre-strain flexure arm to promote steady crack propagation at a later stage. An increasing strain energy release rate was observed concerning the crack length, possibly due to geometrical nonlinearity for a shortened beam and stiffening of the interfaces by fiber bridging.

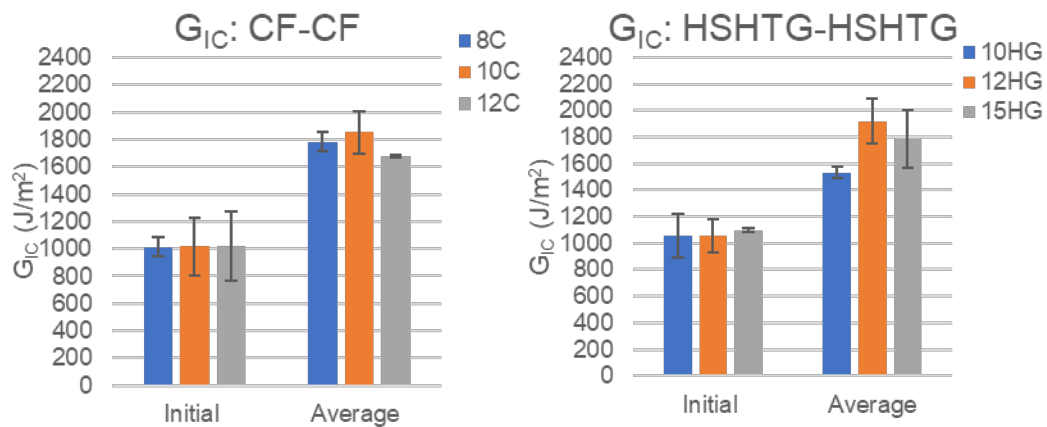


Figure 7. Mode I fracture toughness for crack initiation and crack propagation for (a) CCF-CCF and (b) HSHTG-HSHTG interfaces.

ANOVA tests were conducted to verify the statistical significance of beams of different flexural rigidity by varying fiber layouts. Each data series was first reduced into three representative  $G_{IC}$ s before ANOVA treatment: the NL crack initiation  $G_{IC}$ , the average  $G_{IC}$  from nominal crack length 50-80 mm, and a median  $G_{IC}$  from each series. The results are shown below in **Table 4** and **Table 5**. The initial  $G_{IC}$  does not show a significance between the three configurations for both CCF and HSHTG ( $P > 0.05$ ). Understandably, the behavior indicates a close approximation to the scheme in a simple beam under small deflection. The initial  $G_{IC}$  value is sought to be the design guideline value as suggested by ASTM D5528 for conservation to a higher safety factor. Additional ANOVA tests were conducted throughout the average and median values of the  $G_{IC}$ s separately for CCF and HSHTG. The result suggests that a statistical significance was evident in the series between each configuration, namely 8C/10C/12C and 10G/12G/15G, for the average  $G_{IC}$  value from a nominal crack length 50-80 mm ( $P < 0.1$ ), and the median ( $P < 0.05$ ) of each series. The result indicates that the evolution of the calculated mode I fracture toughness differs from the flexural stiffness used for the beam and possibly results from differences in the geometrical changes. The deviation of the  $G_{IC}$  propagation value also manifests the nonlinear effect caused by beam bending and arm shortening by rotation, even though the introduced correction factor has corrected some.

Table 4. Single-factor ANOVA analysis for 8C, 10C, and 12C for initial, averaged, and Median  $G_{ICS}$ .

ANOVA - $G_{IC,CCF}$ Ini.						
Source of Variation	SS	df	MS	F	P-value	F crit
Between Groups	0.00	2	0.00	0.03	0.97	5.14
Within Groups	0.22	6	0.04			
Total	0.22	8				
ANOVA - $G_{IC,CCF}$ Avg.						
Source of Variation	SS	df	MS	F	P-value	F crit
Between Groups	0.09	2	0.04	5.07	0.05	5.14
Within Groups	0.05	6	0.01			
Total	0.14	8				
ANOVA - $G_{IC,CCF}$ Med.						
Source of Variation	SS	df	MS	F	P-value	F crit
Between Groups	0.12	2	0.062	5.248	0.048	5.143
Within Groups	0.07	6	0.012			
Total	0.20	8				

Table 5. Single-factor ANOVA analysis for 10G, 12G, and 15G for initial, averaged, and Median  $G_{ICS}$ .

ANOVA - $G_{IC,HSTG}$ Ini.						
Source of Variation	SS	df	MS	F	P-value	F crit
Between Groups	0.00	2	0.00	0.11	0.90	4.46
Within Groups	0.13	8	0.02			
Total	0.13	10				
ANOVA - $G_{IC,HSTG}$ Avg.						
Source of Variation	SS	df	MS	F	P-value	F crit
Between Groups	0.25	2	0.12	4.15	0.07	5.14
Within Groups	0.18	6	0.03			
Total	0.43	8				
ANOVA - $G_{IC,HSTG}$ Med.						
Source of Variation	SS	df	MS	F	P-value	F crit
Between Groups	0.20	2	0.10	6.18	0.03	5.14
Within Groups	0.10	6	0.02			
Total	0.30	8				

Some available mode I fracture toughness data related to this study is listed in **Table 6** below.

Table 6. Comparison of  $G_{IC}$  data from literature and this research.

Source	Configuration	$G_{IC}$ initial	Method	$G_{IC}$ propagation
Iragi et al. [25]	CCF-CCF 9 mm	-	MBT	2000 J/m <sup>2</sup>
He et al. [32]	CCF-CCF 3 mm	118.5 ± 10.8 J/m <sup>2</sup>	MBT	1467 ± 20.3 J/m <sup>2</sup>
Goh et al. [30]	CCF-CCF 4 mm	-	CC	943 J/m <sup>2</sup>
Polyzos et al. [29]	CCF-CCF 3.55 mm	1320 ± 310 J/m <sup>2</sup>	MBT / CC / MCC	1320 ± 310 J/m <sup>2</sup>
Kong et al. [22]	CCF-CCF 4 mm	1120 ± 90 J/m <sup>2</sup>	MBT	1120 ± 90 J/m <sup>2</sup>
Aranda et al. [24]	Wavy fiberglass	-	J-integral	111~464 J/m <sup>2</sup>
Santos et al. [26]	CCF-CCF 3 mm CCF-CCF 5 mm	1497 ± 85 J/m <sup>2</sup> 1064 ± 125 J/m <sup>2</sup>	J-integral	1720 ± 116 J/m <sup>2</sup> 1265 ± 57 J/m <sup>2</sup>
Kat-alagaria-nakis et al. [27]	CCF-CCF 7.2mm	1442 ± 374 J/m <sup>2</sup> 1472 ± 352 J/m <sup>2</sup>	MBT MCC	1853 ± 408 J/m <sup>2</sup> 1821 ± 407 J/m <sup>2</sup>
Luke et al. [28]	Onyx-Onyx 5mm	220 ± 137 J/m <sup>2</sup>	MBT	332 ± 170 J/m <sup>2</sup>
Tou-chard et al. [33]	CCF-CCF 3 mm CCF-CCF 3 mm 45°/-45°	1228 ± 114 J/m <sup>2</sup> 1600 J/m <sup>2</sup>	Area method	1228 ± 114 J/m <sup>2</sup> 2150 ± 525 J/m <sup>2</sup>
Santos et al. [34]	CCF-CCF 4 mm 0°/15° CCF-CCF 4 mm -15°/15° CCF-CCF 4 mm -30°/30°	1763 ± 159 J/m <sup>2</sup> 870 ± 71 J/m <sup>2</sup> 960 ± 655 J/m <sup>2</sup>	J-integral	2146 ± 100 J/m <sup>2</sup> 1720 ± 251 J/m <sup>2</sup> 1758 ± 345 J/m <sup>2</sup>
Dong et al. [23]	CCF-CCF 4 mm CCF-Kevlar 4.125 mm Kevlar-Kevlar 4 mm	163 J/m <sup>2</sup> 101 J/m <sup>2</sup> 108 J/m <sup>2</sup>	-	889.8 J/m <sup>2</sup> 2705.8 J/m <sup>2</sup> 3101.9 J/m <sup>2</sup>
This study	CCF-CCF 3 mm HSHTG-HSHTG 3 mm	1017± 168 J/m <sup>2</sup> 1079± 119 J/m <sup>2</sup>	NL / MBT	1806 ± 139 J/m <sup>2</sup> 1457± 238 J/m <sup>2</sup>

## Fracture Analysis and Sample Variability

All load-displacement data points accounted for crack initiation and propagation were compiled and graphed in **Figure 8** and **Figure 9** below. Several sudden crack propagation incidents can be observed from the graphed data. The observation of jumping cracks shows an unsteady crack growth due to the presence of voids as plasticizers and the in-plane inconsistency between each deposited material trace.

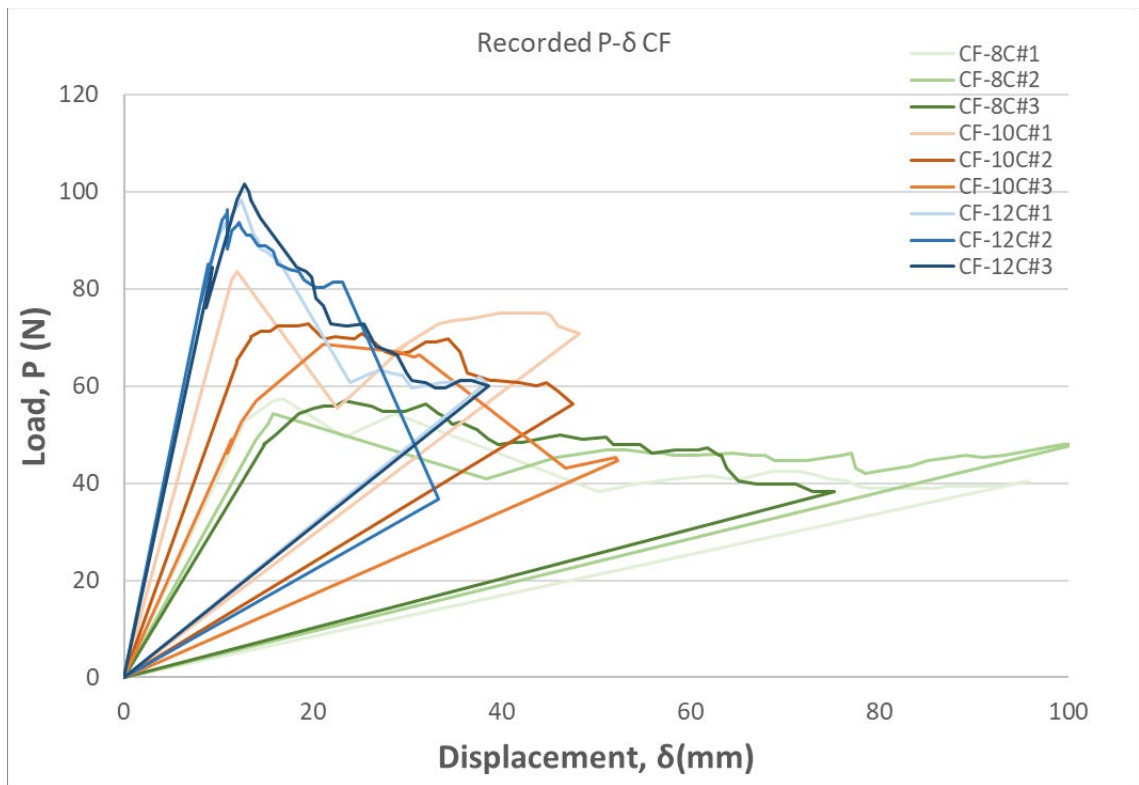


Figure 8. Reduced load-displacement data points for crack propagation in CCF samples.

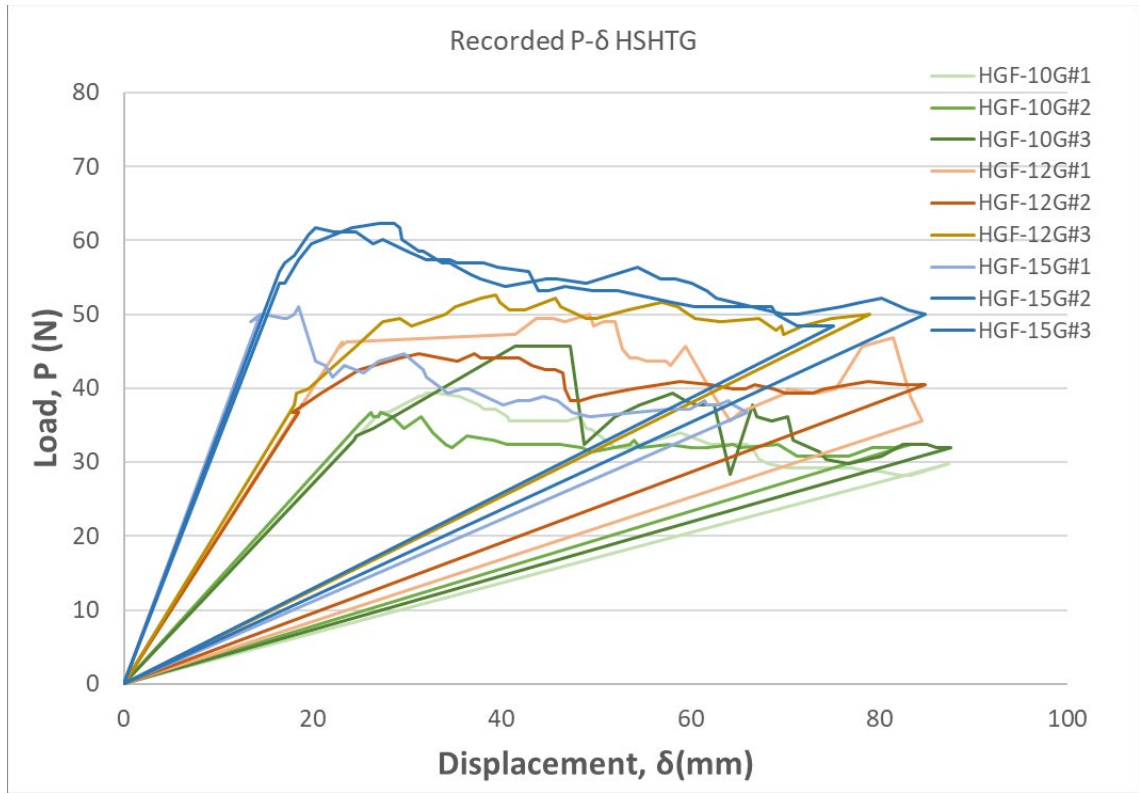


Figure 9. Reduced load-displacement data points for crack propagation in HSHTG samples.

Although not a representative curve throughout all samples, the randomness of the fracture behavior under mode I loading is evident. Due to structural inhomogeneity, the beam can undergo various events that could increase the load capacity for interfacial debonding, resulting in effects unaccounted for that could affect the calculated  $G_{IC}$  throughout the crack propagation cycle, including asymmetric bending, decohesion of the side wall, flexure top lamina, and extensive bridging. In the case of any of the incidents listed above, the data points have been removed to prevent undesired stiffening factors that cause imprecise  $G_{IC}$ . The occurrence of bridging of single fiber yarn, partial damage to the top layer, and in-plane bending of the single extrusion is allowed as they are stochastically distributed and consistently observed. The event of anomalies that increase the

load capacity would otherwise be favorable in the case of the actual applications, as it is considered a stiffening mechanism that hinders crack propagation. The evolution of fracture toughness concerning the crack length and the crack initiation  $G_{IC}$  calculated from three different methods were plotted below in **Figure 10** and **Figure 11**. A general trend of increasing  $G_{IC}$  can be seen in the figure as a manifestation of fiber bridging between the lamina inhibited the crack route.

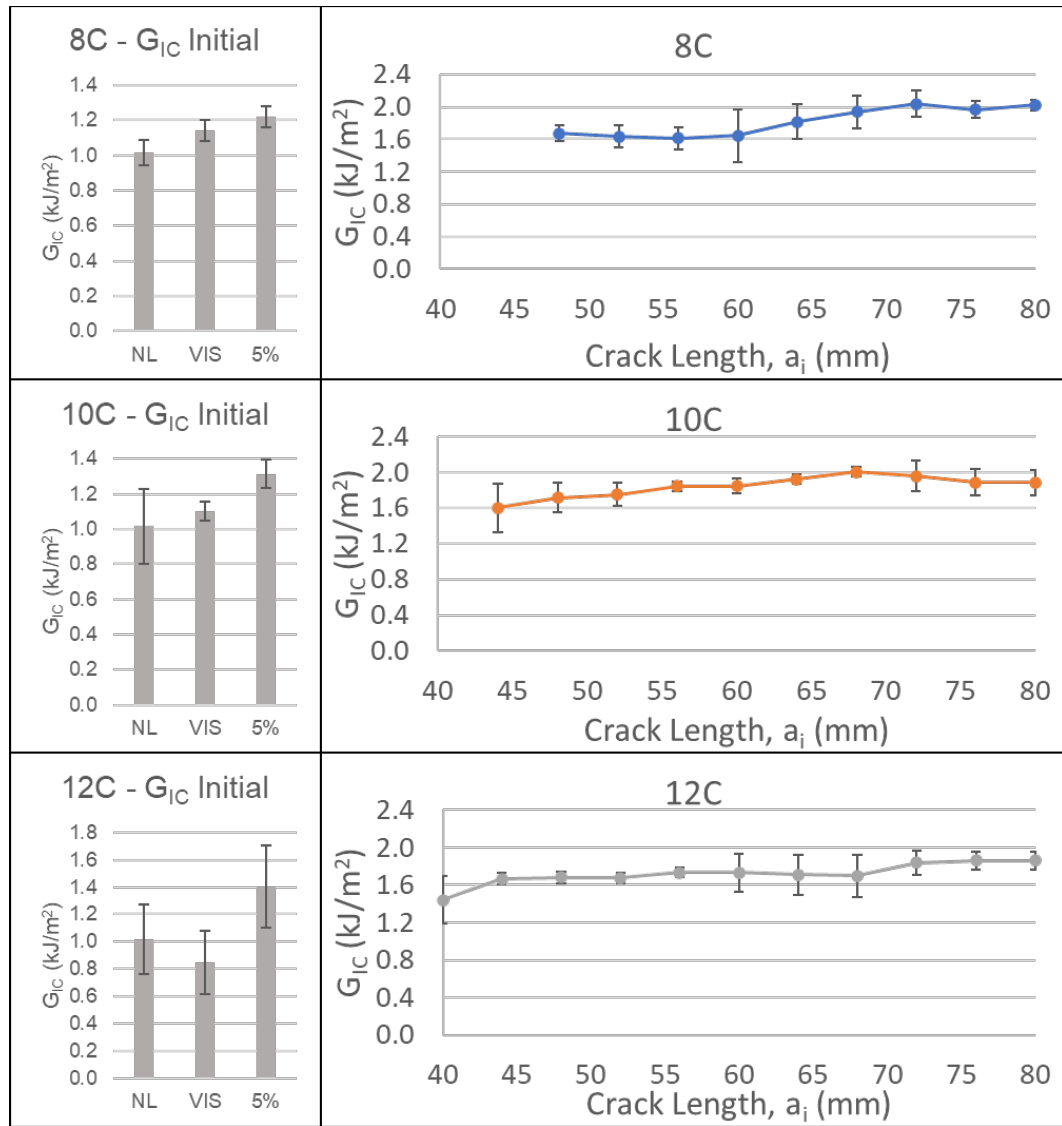


Figure 10. Comparison of all mode I fracture toughness for crack initiation and crack propagation regarding the nominal crack length for CCF samples.

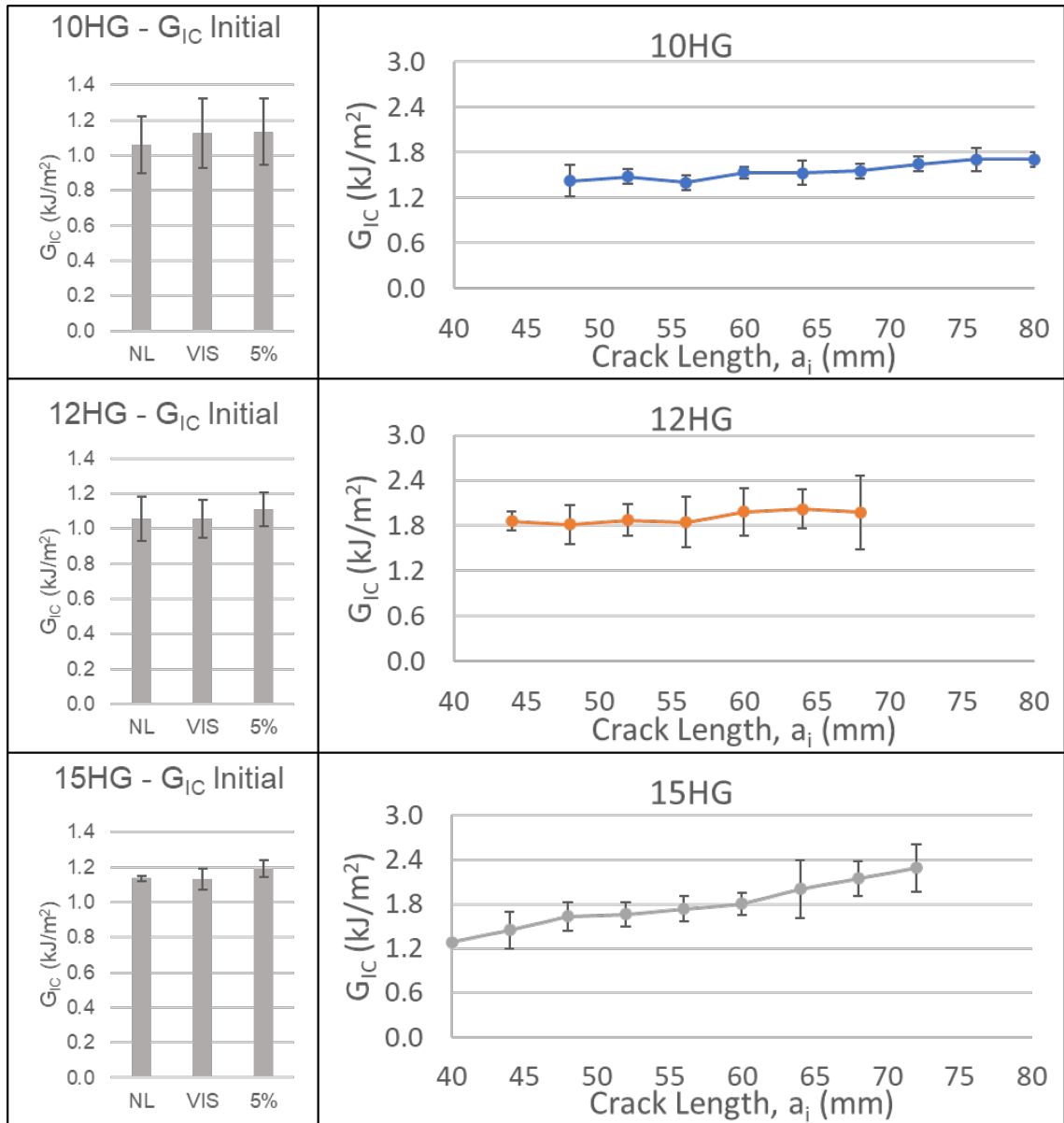


Figure 11. Comparison of all mode I fracture toughness for crack initiation and crack propagation regarding the nominal crack length for HSGTG samples.

A resistance curve was constructed for all DCB samples in **Figure 12**. Observation of the carbon-carbon data shows that fiber bridging can occur with a lower flexural stiffness due to the extensive peeling effect over the interfacial layers, as evident in the stiffening effect in 8C and 10C as the crack propagates. The event was not evident in the 12C samples as the peeling effect on the interlaminar region is less severe for higher



flexural rigidity; therefore, less interfacial stiffening was observed. As the identification of instantaneous crack length is limited in the later propagation stage, an observable maximum crack length between the configurations was also evident. Fiber bridging can occur whenever an extensive unsteady crack propagation is observed due to the artifacts of printing, causing an unbalanced strain energy release within the deposited materials traces in the layer undergoing delamination.

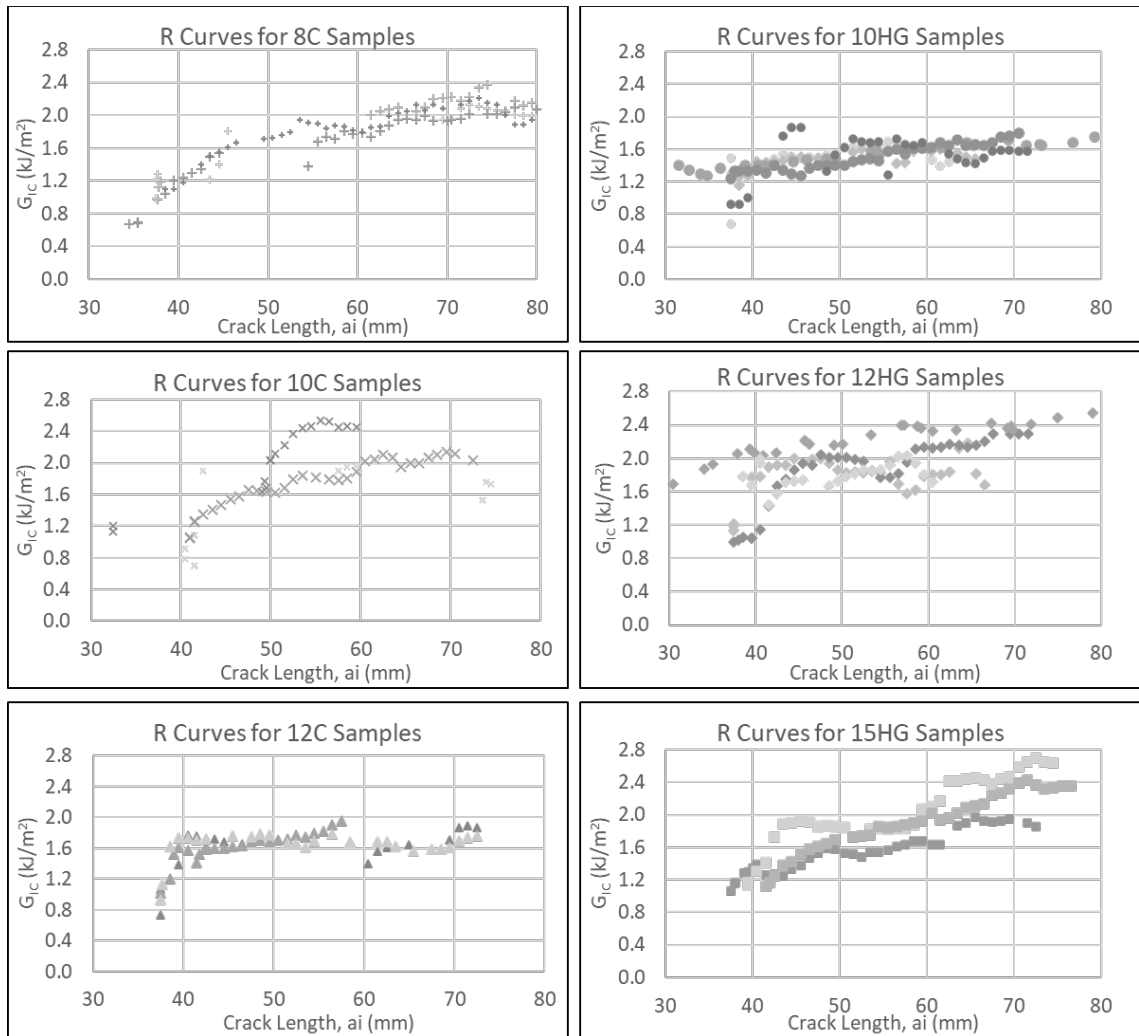


Figure 12. The reduced load-displacement curve for crack propagation for all DCB samples.

A similar trend was found for HSHTG samples, for which the crack growth is nonsteady for both 10HG and 12HG, suggesting an extensive bending in the loading arm. Although the beam flexures differently between the configurations, the initial  $G_{IC}$  remains reasonably consistent within the groups. It was also observed for the 15HG samples that the calculated  $G_{IC}$  goes higher in the later crack propagation stage, resulting from permanent deflection of the outermost laminae, as corroborated with the fractography image as shown in **Figure 13a**. The kinked materials extrusion line on the surface of the outermost layers in 15HG samples was observed due to compression-flexure failure. **Figure 13b**. shows the difference in morphologies between the surface after the crack propagation (left) and the precrack (right). A higher concentration of regime of voids present in the crack propagation surface signals the incident of materials peeling off partially from the surface during the process.

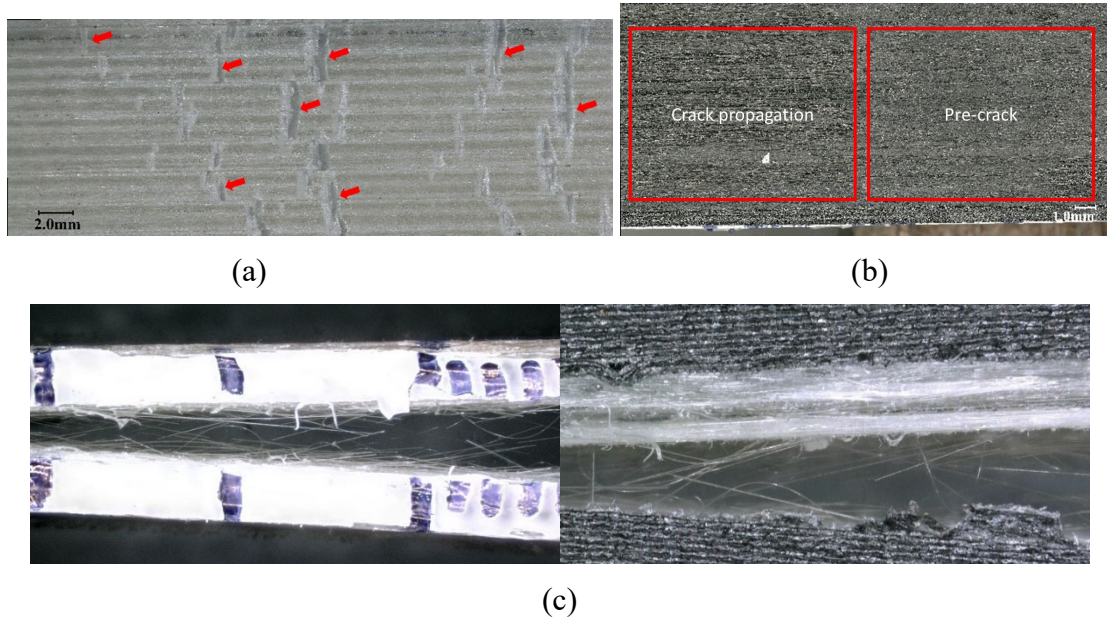


Figure 13 (a) Upper side of the HSHTG samples signals microcrack coalescence over the outermost fiber layer, (b) Fracture surface of the CCF samples, (c) Fiber bridging on the side of DCB samples for HSHTG(left) and CCF (right)

The fractography corroborates the partial disintegration phenomenon that could cause increasing load as the interfaces do not break entirely; therefore, a higher fracture toughness  $G_{IC}$  value is calculated. **Figure 13c** shows the depth scan image using the Keyence microscope, for which fiber bridging is evident.

## CONCLUSIONS

Flexural properties and their relationship to the CFF content were successfully determined, and their relationship with FVF was evaluated. The simple beam analysis can be adopted in orthotropic composite beams as long as the in-plane shear stress is negligible. On the contrary, when the in-plane shear stresses supersede the material's capability, the AMFRP can fail prematurely due to delamination. Treatments of the characterized data show a positive correlation of CFF content to the flexural responses, based on empirical data from this study and the literature. The unstressed fiber and the voids embedded within the beam provide the CFRP composites with a higher strain limit compared to the conventional CFRP composites.

Mode I fracture toughness was characterized on AMFRP samples, and the effect of different laminated sequences on the mode I fracture toughness was examined. The calculated crack initiation  $G_{IC}$  value is consistent for CCF and HSHTG configurations regarding the interface type. Corroboration on the conclusion was inspected with a single-factor ANOVA with repetitive measurements, and the variability within groups of configurations and between groups of surface type was found to be insignificant. The initiation  $G_{IC}$  data for CCF also closely resembles the available data in the literature. The crack propagation  $G_{IC}$  was observed to have an increasing trend along with the crack

propagation length, resulting from the mechanical responses of the beam, including bending, fiber bridging, and kinked surface. A statistical significance was found between the series of crack propagation  $G_{IC}$  for the different configurations, indicating that the crack can propagate unstably in the later stage of the crack propagation, possibly resulting from the stress concentration and fracture jump to an adjacent interface. Although the stochastic voids that introduced the incidences of unstable crack propagation can result in low initiation  $G_{IC}$ , the higher  $G_{IC}$  at the later stage could implicate possible arrest of the fracture. The  $G_{IC}$  equilibrium can fluctuate due to secondary strain energy release phenomena such as fiber bridging and intralaminar fracture. It is determined that the flexural rigidity of the beam does not directly correlate with the initial  $G_{IC}$ . However, it does modify the fracture responses of the laminated FRP plate for crack propagation. Caution should be taken when designing load-bearing laminated structures made of AMFRP composites, for which failure can occur in unexpected areas over the combined compression, shear, peel, and through-interface crack propagation if not accounted for properly.

## REFERENCES

1. Sun, C.T. and Jin, Z.H. (2012) In Sun, C. T. and Jin, Z. H. (eds.), *Fracture Mechanics*. Academic Press, Boston, pp. 1-10.
2. Rice, J.R. (1968) Mathematical analysis in the mechanics of fracture. *Fracture: an advanced treatise*, **2**, 191-311.
3. Meyers, M.A. and Chawla, K.K. (2008) *Mechanical behavior of materials*. Cambridge university press.
4. Budarapu, P.R., Zhuang, X., Rabczuk, T. and Bordas, S.P.A. (2019), *Advances in Crystals and Elastic Metamaterials, Part 2*, pp. 1-103.
5. Barenblatt, G.I. (1962), *Advances in applied mechanics*. Elsevier, Vol. 7, pp. 55-129.

6. Kanninen, M.F., McEvily, A. and Popelar, C.H. (1986) Advanced fracture mechanics.
7. Sela, N. and Ishai, O. (1989) Interlaminar fracture toughness and toughening of laminated composite materials: a review. *Composites*, **20**, 423-435.
8. Carlsson, L.A., Adams, D.F. and Pipes, R.B. (2014) *Experimental characterization of advanced composite materials*. CRC press.
9. Williams, J. (1987) Large displacement and end block effects in the 'DCB' interlaminar test in modes I and II. *Journal of Composite Materials*, **21**, 330-347.
10. Williams, J. (1989) The fracture mechanics of delamination tests. *The Journal of strain analysis for engineering design*, **24**, 207-214.
11. Naik, R.A., Crews, J.H. and Shivakumar, K.N. (1991) Effects of T-tabs and large deflections in double cantilever beam specimen tests. *IN: Composite materials: Fatigue and fracture.*, **3**, 169-186.
12. Hashemi, S., Kinloch, A. and Williams, J. (1989) Corrections needed in double-cantilever beam tests for assessing the interlaminar failure of fibre-composites. *Journal of Materials Science Letters*, **8**, 125-129.
13. Chawla, K.K. (2012) *Composite materials: science and engineering*. Springer Science & Business Media.
14. Ning, H., Lu, N., Hassen, A.A., Chawla, K., Selim, M. and Pillay, S. (2019) A review of Long fibre thermoplastic (LFT) composites. *International Materials Reviews*, **65**, 164-188. <https://doi.org/10.1080/09506608.2019.1585004>.
15. Yuan, S., Li, S., Zhu, J. and Tang, Y. (2021) Additive manufacturing of polymeric composites from material processing to structural design. *Composites Part B: Engineering*, **219**, 108903. <https://doi.org/10.1016/j.compositesb.2021.108903>.
16. Hegab, H.A. (2016) Design for additive manufacturing of composite materials and potential alloys: a review. *Manufacturing Review*, **3**, 11. <https://doi.org/10.1051/mfreview/2016010>.
17. Thompson, M.K., Moroni, G., Vaneker, T., Fadel, G., Campbell, R.I., Gibson, I., Bernard, A., Schulz, J., Graf, P. and Ahuja, B. (2016) Design for Additive Manufacturing: Trends, opportunities, considerations, and constraints. *CIRP annals*, **65**, 737-760.
18. Kang, J., Shangguan, H., Deng, C., Hu, Y., Yi, J., Wang, X., Zhang, X. and Huang, T. (2018) Additive manufacturing-driven mold design for castings. *Additive Manufacturing*, **22**, 472-478.

19. Hegab, H., Khanna, N., Monib, N. and Salem, A. (2023) Design for sustainable additive manufacturing: A review. *Sustainable Materials and Technologies*, **35**. <https://doi.org/10.1016/j.susmat.2023.e00576>.
20. Yang, Q. and Cox, B. (2005) Cohesive models for damage evolution in laminated composites. *International Journal of Fracture*, **133**, 107-137. <https://doi.org/10.1007/s10704-005-4729-6>.
21. Xiang, J., Cheng, P., Wang, K., Wu, Y., Rao, Y. and Peng, Y. (2023) Interlaminar and translaminar fracture toughness of 3D-printed continuous fiber reinforced composites: A review and prospect. *Polymer Composites*. <https://doi.org/10.1002/pc.28065>.
22. Kong, X., Luo, J., Luo, Q., Li, Q. and Sun, G. (2022) Experimental study on interface failure behavior of 3D printed continuous fiber reinforced composites. *Additive Manufacturing*, **59**. <https://doi.org/10.1016/j.addma.2022.103077>.
23. Dang, Z., Cao, J., Pagani, A. and Zhang, C. (2023) Fracture toughness determination and mechanism for mode-I interlaminar failure of 3D-printed carbon-Kevlar composites. *Composites Communications*, **39**. <https://doi.org/10.1016/j.coco.2023.101532>.
24. Aranda, M.T., Reinoso, J. and García, I.G. (2022) On different 3D printing methods and fracture performance in DCB composite specimens including structured interfaces. *Theoretical and Applied Fracture Mechanics*, **122**. <https://doi.org/10.1016/j.tafmec.2022.103552>.
25. Iragi, M., Pascual-González, C., Esnaola, A., Lopes, C.S. and Aretxabaleta, L. (2019) Ply and interlaminar behaviours of 3D printed continuous carbon fibre-reinforced thermoplastic laminates; effects of processing conditions and microstructure. *Additive Manufacturing*, **30**, 100884. <https://doi.org/10.1016/j.addma.2019.100884>.
26. Santos, J.D., Fernandez, A., Ripoll, L. and Blanco, N. (2022) Experimental Characterization and Analysis of the In-Plane Elastic Properties and Interlaminar Fracture Toughness of a 3D-Printed Continuous Carbon Fiber-Reinforced Composite. *Polymers (Basel)*, **14**. <https://doi.org/10.3390/polym14030506>.
27. Katalagarianakis, A., Polyzos, E., Van Hemelrijck, D. and Pyl, L. (2023) Mode I, mode II and mixed mode I-II delamination of carbon fibre-reinforced polyamide composites 3D-printed by material extrusion. *Composites Part A: Applied Science and Manufacturing*, **173**. <https://doi.org/10.1016/j.compositesa.2023.107655>.
28. Luke, S.S., Soares, D., Marshall, J.V., Shedd, J. and Keleş, Ö. (2021) Effect of fiber content and fiber orientation on mechanical behavior of fused filament fabricated continuous-glass-fiber-reinforced nylon. *Rapid Prototyping Journal*, **ahead-of-print**. <https://doi.org/10.1108/RPJ-01-2021-0003>.

29. Polyzos, E., Katalagarianakis, A., Van Hemelrijck, D. and Pyl, L. (2021) Delamination analysis of 3D-printed nylon reinforced with continuous carbon fibers. *Additive Manufacturing*, **46**. <https://doi.org/10.1016/j.addma.2021.102144>.
30. Goh, G.D., Dikshit, V., An, J. and Yeong, W.Y. (2020) Process-structure-property of additively manufactured continuous carbon fiber reinforced thermoplastic: an investigation of mode I interlaminar fracture toughness. *Mechanics of Advanced Materials and Structures*, 1-13. <https://doi.org/10.1080/15376494.2020.1821266>.
31. Long, Y., Zhang, Z., Fu, K. and Li, Y. (2021) Efficient plant fibre yarn pre-treatment for 3D printed continuous flax fibre/poly(lactic) acid composites. *Composites Part B: Engineering*, **227**. <https://doi.org/10.1016/j.compositesb.2021.109389>.
32. He, Q., Wang, H., Fu, K. and Ye, L. (2020) 3D printed continuous CF/PA6 composites: Effect of microscopic voids on mechanical performance. *Composites Science and Technology*, **191**. <https://doi.org/10.1016/j.compscitech.2020.108077>.
33. Touchard, F., Chocinski-Arnault, L., Fournier, T., Magro, C., Lafitte, A. and Caradec, A. (2021) Interfacial adhesion quality in 3D printed continuous CF/PA6 composites at filament/matrix and interlaminar scales. *Composites Part B: Engineering*, **218**, 108891. <https://doi.org/10.1016/j.compositesb.2021.108891>.
34. Santos, J.D., Guerrero, J.M., Blanco, N., Fajardo, J.I. and Paltan, C.A. (2023) Numerical and Experimental Analysis of the Mode I Interlaminar Fracture Toughness in Multidirectional 3D-Printed Thermoplastic Composites Reinforced with Continuous Carbon Fiber. *Polymers (Basel)*, **15**. <https://doi.org/10.3390/polym15102403>.
35. Khosravani, M.R., Frohn-Sörensen, P., Reuter, J., Engel, B. and Reinicke, T. (2022) Fracture studies of 3D-printed continuous glass fiber reinforced composites. *Theoretical and Applied Fracture Mechanics*, **119**. <https://doi.org/10.1016/j.tafmec.2022.103317>.
36. A. Gold, S., Strong, R. and N. Turner, B. (2014) A review of melt extrusion additive manufacturing processes: I. Process design and modeling. *Rapid Prototyping Journal*, **20**, 192-204. <https://doi.org/10.1108/rpj-01-2013-0012>.
37. Turner, B.N. and Gold, S.A. (2015) A review of melt extrusion additive manufacturing processes: II. Materials, dimensional accuracy, and surface roughness. *Rapid Prototyping Journal*, **21**, 250-261. <https://doi.org/10.1108/rpj-02-2013-0017>.
38. Pascual-González, C., Iragi, M., Fernández, A., Fernández-Blázquez, J.P., Aretxabaleta, L. and Lopes, C.S. (2020) An approach to analyse the factors behind the micromechanical response of 3D-printed composites. *Composites Part B: Engineering*, **186**, 107820. <https://doi.org/10.1016/j.compositesb.2020.107820>.

39. Shih, Y.-C., Mohamed, M., Ge, J., Sen, S., Pillay, S. and Ning, H. (2023) Application of interlaminar shear strength and finite element modeling for failure analysis of 3D printed continuous fiber-reinforced composites. *Progress in Additive Manufacturing*. <https://doi.org/10.1007/s40964-023-00417-8>.
40. Chabaud, G., Castro, M., Denoual, C. and Le Duigou, A. (2019) Hygromechanical properties of 3D printed continuous carbon and glass fibre reinforced polyamide composite for outdoor structural applications. *Additive Manufacturing*, **26**, 94-105. <https://doi.org/10.1016/j.addma.2019.01.005>.
41. ASTM. (2015), ISO / ASTM52900-15, Standard Terminology for Additive Manufacturing – General Principles – Terminology. ASTM International, West Conshohocken, PA. <https://doi.org/10.1520/F3177-21>.
42. Markforged Inc. (2022) Materials Datasheet - Composites. <https://web-objects.markforged.com/craft/materials/CompositesV5.2.pdf>.
43. Shih, Y.-C., Ning, H., Sen, S., Mohamed, M., Yan, Y. and Pillay, S. (2024) Assessment of fiber reinforcement strategies for additively manufactured thermoplastic composites using mechanical testing and finite element analysis. *Progress in Additive Manufacturing*. <https://doi.org/10.1007/s40964-024-00569-1>.
44. ASTM. (2017), Standard test methods for flexural properties of unreinforced and reinforced plastics and electrical insulating materials. *ASTM D790-17*. ASTM International, West Conshohocken, PA. <https://doi.org/10.1520/D0790-17>.
45. Melenka, G.W., Cheung, B.K.O., Schofield, J.S., Dawson, M.R. and Carey, J.P. (2016) Evaluation and prediction of the tensile properties of continuous fiber-reinforced 3D printed structures. *Composite Structures*, **153**, 866-875. <https://doi.org/10.1016/j.compstruct.2016.07.018>.
46. Naranjo-Lozada, J., Ahuett-Garza, H., Orta-Castañón, P., Verbeeten, W.M.H. and Sáiz-González, D. (2019) Tensile properties and failure behavior of chopped and continuous carbon fiber composites produced by additive manufacturing. *Additive Manufacturing*, **26**, 227-241. <https://doi.org/10.1016/j.addma.2018.12.020>.
47. ASTM D5528-13, Standard Test Method for Mode I Interlaminar Fracture Toughness of Unidirectional Fiber-Reinforced Polymer Matrix Composites, ASTM International, West Conshohocken, PA, 2013, [www.astm.org](http://www.astm.org).
48. Dickson, A.N., Barry, J.N., McDonnell, K.A. and Dowling, D.P. (2017) Fabrication of continuous carbon, glass and Kevlar fibre reinforced polymer composites using additive manufacturing. *Additive Manufacturing*, **16**, 146-152. <https://doi.org/10.1016/j.addma.2017.06.004>.
49. Parmiggiani, A., Prato, M. and Pizzorni, M. (2021) Effect of the fiber orientation on the tensile and flexural behavior of continuous carbon fiber composites made



via fused filament fabrication. *The International Journal of Advanced Manufacturing Technology*, **114**, 2085-2101.

50. Ghebretinsae, F., Mikkelsen, O. and Akessa, A.D. (2019), *IOP conference series: materials science and engineering*. IOP Publishing, Vol. 700, pp. 012024.
51. Araya-Calvo, M., López-Gómez, I., Chamberlain-Simon, N., León-Salazar, J.L., Guillén-Girón, T., Corrales-Cordero, J.S. and Sánchez-Brenes, O. (2018) Evaluation of compressive and flexural properties of continuous fiber fabrication additive manufacturing technology. *Additive Manufacturing*, **22**, 157-164. <https://doi.org/10.1016/j.addma.2018.05.007>.
52. (2000) *Composite Materials Handbook MIL 17: Vol. II: Polymer Matrix Composites*. MIL-HDBK-17-2F ed. CRC Press LLC.

## OVERALL CONCLUSIONS

The increasing presence of FRP composites in the AM industries is inevitable and evident in the ever-increasing novel composite materials available in the market. The polyamide-based feedstock has been at the forefront of all AM polymers as the most profitable material [4], owing to its promising performance, endurance, and versatility. This study gives a comprehensive analysis of the mechanical behaviors of AMFRP polyamide-based composites. The tensile behaviors of the AMFRP composites with various designed fiber configurations were studied to evaluate the effectiveness of the reinforcement and the resulting AMFRP's performance. The 50%-infilled CCF composites effectively create a hollowed sandwich structure with sufficient continuous fiber in the longitudinal direction to provide reinforcement, which can potentially be used in lightweight structural design. Premature failure was observed in some configurations, citing the possible weaknesses in translaminar and interlaminar direction induced by the combined effect of the geometric characteristics and configured reinforcing strategies. A modeling scheme based on finite element analysis was developed to reduce redundant mechanical tests during trial-and-error and find optimized configurations with numerical simulation.

Materials properties at the ply level were derived and implemented into a CLT-based algorithm. The algorithm was then applied to dimensionally reduced models to generate a solid body. The model implemented accounted for the anisotropic stiffness matrix regarding the stack-up sequences and the geometry nonlinearity from large

deformation. It was found that the simulated modulus and strength are in good agreement with the mechanical test results. The result suggests that the methodology can produce high-fidelity results to simulate AMFRP composites' tensile performance with non-conventional fiber configurations, such as concentric fibers, perimeter walls, and unidirectional reinforcement. Other than the linear elastic behavior of CFRP, the discontinuous FRP samples were also successfully modeled using materials data characterized from a baseline coupon using a multi-linear curve fitting to relate to the instantaneous tangent modulus observed in coupon characterization. The model successfully captures the plastic yielding of the 3D-printed structure in samples with a 50%-infilled hollowed structure, manifesting the stage decohesion of the structure from the physical defects embedded between and within laminae. Failure strain on each sample was plotted against the cross-sectional area fiber content, and it was found that a low fiber fraction can introduce an undesired strain limit while minimal reinforcing is achieved. The homogenization approach is able to generate results with a low error margin. It also retains both anisotropy and elastoplasticity materials' properties using a fine-meshed model. The FEA model was used to predict the stress field in tensile and SLJ samples.

The single-lap joint samples were designed, tested, and analyzed to find a connection between interlaminar shear strength and various interfacial fiber orientations. It is concluded that the characterized SLJ strength of the interface was not solely shear but a complex stress composed of shear, tensile, and peel stresses. The conclusion is backed by fracture surface analysis to highlight morphologies of different fracture modes, while image illustrations to identify the critical fracturing stress were also provided. The statistics of the mechanical results were illustrated and visualized with a boxplot and a 95%

confidence interval plot. The numerical simulation result using finite element analysis software can help to identify the specific fracture mechanisms by factoring in the deformation and material nonlinearity effects. The stress components of tensile, shear, and peel were broken down and illustrated over the 2D and 3D spaces of the bonded interfacial regime. The distribution of shear stresses agrees with the classical analytical SLJ theorem that accounts for the load eccentricity from beam deflection and the effect of differential shear. The SLJ strength of the bonded interfaces was evaluated on a case-by-case basis, and a symmetric adherend design was recommended to avoid excessive unbalanced stresses.

The flexural behavior of AMFRP was investigated using a three-point bending test to evaluate the effectiveness of fiber reinforcement on flexural performance. The flexural stiffness is shown to display a linear relationship to the cross-sectional fiber content. The mode I fracture toughness for two interfaces, between two continuous carbon fiber layers and two continuous glass fiber layers, was characterized. Three variants of beam stiffness were tested for each interfacial bonding condition using different counts of continuous layers. A new method was developed and implemented to manufacture the precrack of the DCB samples. After pausing the printing process, a mold release agent was applied to the desired interfaces.

Examination of the the mode I fracture toughness results using ANOVA found no statistical significance in the variability of the initial  $G_{IC}$  over different beam configurations ( $p > 0.05$ ), confirming that the data reduction technique adapted from the LEFM assumption can capture crack initiation  $G_{IC}$  from the pre-cracked interface with high consistency. However, the subsequent ANOVA treatments on the median and average value

of each series of  $G_{IC}$  throughout crack propagation show statistical significance between in-group and between-group variability, suggesting that the fracture behavior can be associated with the varying beam composition during crack propagation. The initiation  $G_{IC}$  value of  $1\text{kJ/m}^2$  is reported for both the CCF-CCF and HSHTG-HSHTG interface.

The mode I crack propagation behavior of the DCB samples appears to be a dynamic process that can induce damage near the crack front and outermost layer under compression. The load reading on the propagation is determined by multiple mechanical behaviors during the test, including fiber bridging, lamina damage, and crack jumping. This signals that the load-displacement and resistance curves derived from the experiments can only be used to model the behaviors of objects with identical material and geometry. On the contrary, the initial  $G_{IC}$  is relatively consistent regardless of the beams' flexural rigidity. Further studies can be conducted to study the failure behaviors at the ply level and determine their correlation to other characterized materials' properties.

The characteristic behaviors of AMFRP are predominantly governed by the linear elastic orthotropic properties of the continuous fiber undergoing monotonic tensile stresses. However, significant variations of failure modes can be observed in a system of anisotropic mesostructure, for which stress concentration can happen with the non-trivial stress fields. The configurations can be selected comprehensively using a combination of empirical characterization with mechanical testing, analytical mechanics modeling, statistics, and numerical simulation. Analysis of fractography and microscopy images provides physical evidence for failure criteria validation and works interactively with the CAE workflow to achieve optimized mechanical performance of AMFRP.

## FUTURE WORK

The characteristic morphologies and failure behavior of AMFRP can be effectively evaluated before manufacturing and prototyping to accelerate product development. Future work to identify the critical stress components within the bulk AMFRP products can be further done with instantaneous three-dimensional digital image correlation (DIC) to support the modeling development of structural responses analytically or numerically. The area of DfAM provides a foundation to push for optimized design and efficient materials processing workflow to boost confidence in delivering performance-driven engineering design using novel materials for AMFRP. A data-driven modeling approach can be orchestrated by developing a robust material database or library to aid in implementing and predicting the materials' mechanical responses undergoing different AM methods. The mechanical performance of AMFRP can be further improved with a better understanding of the scale-up effect of microstructure-mesostructure-megastructure. Mode-specific failure criteria and proper correction factors can be developed to provide representative mechanical responses with a unified field of defects.

## GENERAL REFERENCES

1. Chawla, K.K. (2012) *Composite materials: science and engineering*. Springer Science & Business Media.
2. Jang, B.Z. (1994) Advanced polymer composites: principles and applications. *ASM International, Materials Park, OH 44073-0002, USA, 1994. 305.*
3. Fidan, I., Imeri, A., Gupta, A., Hasanov, S., Nasirov, A., Elliott, A., Alifui-Segbaya, F. and Nanami, N. (2019) The trends and challenges of fiber reinforced additive manufacturing. *The International Journal of Advanced Manufacturing Technology*, **102**, 1801-1818.
4. Wohlers, T.T., Campbell, I., Diegel, O., Huff, R. and Kowen, J. (2022) *Wohlers Report 2022 3D Printing and Additive Manufacturing Global State of the Industry*.
5. Parandoush, P. and Lin, D. (2017) A review on additive manufacturing of polymer-fiber composites. *Composite Structures*, **182**, 36-53. <https://doi.org/10.1016/j.compstruct.2017.08.088>.
6. A. Gold, S., Strong, R. and N. Turner, B. (2014) A review of melt extrusion additive manufacturing processes: I. Process design and modeling. *Rapid Prototyping Journal*, **20**, 192-204. <https://doi.org/10.1108/rpj-01-2013-0012>.
7. Tekinalp, H.L., Kunc, V., Velez-Garcia, G.M., Duty, C.E., Love, L.J., Naskar, A.K., Blue, C.A. and Ozcan, S. (2014) Highly oriented carbon fiber-polymer composites via additive manufacturing. *Composites Science and Technology*, **105**, 144-150. <https://doi.org/10.1016/j.compscitech.2014.10.009>.
8. Dilberoglu, U.M., Gharehpapagh, B., Yaman, U. and Dolen, M. (2017) The Role of Additive Manufacturing in the Era of Industry 4.0. *Procedia Manufacturing*, **11**, 545-554. <https://doi.org/10.1016/j.promfg.2017.07.148>.
9. Pyl, L., Kalteremidou, K.-A. and Van Hemelrijck, D. (2019) Exploration of the design freedom of 3D printed continuous fibre-reinforced polymers in open-hole tensile strength tests. *Composites Science and Technology*, **171**, 135-151. <https://doi.org/10.1016/j.compscitech.2018.12.021>.
10. Goh, G.D., Dikshit, V., Nagalingam, A.P., Goh, G.L., Agarwala, S., Sing, S.L., Wei, J. and Yeong, W.Y. (2018) Characterization of mechanical properties and

- fracture mode of additively manufactured carbon fiber and glass fiber reinforced thermoplastics. *Materials & Design*, **137**, 79-89. <https://doi.org/10.1016/j.matdes.2017.10.021>.
11. Hart-Smith, L. (1998) Predictions of the original and truncated maximum-strain failure models for certain fibrous composite laminates. *Composites Science and Technology*, **58**, 1151-1178. [https://doi.org/10.1016/s0266-3538\(97\)00192-9](https://doi.org/10.1016/s0266-3538(97)00192-9).
  12. París, F., Velasco, M.L. and Correa, E. (2021) The scale effect in composites: An explanation physically based on the different mechanisms of damage involved in failure. *Composite Structures*, **257**. <https://doi.org/10.1016/j.compstruct.2020.113089>.
  13. Sun, C.T. and Jin, Z.H. (2012) In Sun, C. T. and Jin, Z. H. (eds.), *Fracture Mechanics*. Academic Press, Boston, pp. 227-246.
  14. Liu, P.F. and Zheng, J.Y. (2010) Recent developments on damage modeling and finite element analysis for composite laminates: A review. *Materials & Design*, **31**, 3825-3834. <https://doi.org/10.1016/j.matdes.2010.03.031>.
  15. Camanho, P.P. and Dávila, C.G. (2002) Mixed-mode decohesion finite elements for the simulation of delamination in composite materials.
  16. Dávila, C.G., Camanho, P.P. and Turon, A. (2008) Effective simulation of delamination in aeronautical structures using shells and cohesive elements. *Journal of Aircraft*, **45**, 663-672.
  17. Hopkinson, N., Hague, R. and Dickens, P. (2006) *Rapid manufacturing: an industrial revolution for the digital age*. John Wiley & Sons.
  18. Turner, B.N. and Gold, S.A. (2015) A review of melt extrusion additive manufacturing processes: II. Materials, dimensional accuracy, and surface roughness. *Rapid Prototyping Journal*, **21**, 250-261. <https://doi.org/10.1108/rpj-02-2013-0017>.
  19. Muller, J.P., L. (2021). <https://doi.org/doi.org/10.2777/187237>. [online] Op.europa.eu. Available at: <<https://op.europa.eu/s/sNVu>>
  20. Ford, S.L. (2014) Additive manufacturing technology: potential implications for US manufacturing competitiveness. *J. Int'l Com. & Econ.*, **6**, 40.
  21. Bourell, D.L., Beaman, J.J., Leu, M.C. and Rosen, D.W. (2009) A brief history of additive manufacturing and the 2009 roadmap for additive manufacturing: looking back and looking ahead. *Proceedings of RapidTech*, 24-25.
  22. Hull, C.W. (1986). Google Patents.



23. Ngo, T.D., Kashani, A., Imbalzano, G., Nguyen, K.T.Q. and Hui, D. (2018) Additive manufacturing (3D printing): A review of materials, methods, applications and challenges. *Composites Part B: Engineering*, **143**, 172-196. <https://doi.org/10.1016/j.compositesb.2018.02.012>.
24. G.F, B. and Carvalho, J. (2013) Design for Manufacturing and Assembly methodology applied to aircrafts design and manufacturing. *IFAC Proceedings Volumes*, **46**, 116-121. <https://doi.org/10.3182/20130522-3-br-4036.00044>.
25. Geoffrey, B. (1994) Product design for manufacture and assembly. *Computer-Aided Design*, **26**, 505-520.
26. Thompson, M.K., Moroni, G., Vaneker, T., Fadel, G., Campbell, R.I., Gibson, I., Bernard, A., Schulz, J., Graf, P. and Ahuja, B. (2016) Design for Additive Manufacturing: Trends, opportunities, considerations, and constraints. *CIRP annals*, **65**, 737-760.
27. Akkerman, R., Bouwman, M. and Wijskamp, S. (2020) Analysis of the Thermoplastic Composite Overmolding Process: Interface Strength. *Frontiers in Materials*, **7**. <https://doi.org/10.3389/fmats.2020.00027>.
28. Chacón, J.M., Caminero, M.A., García-Plaza, E. and Núñez, P.J. (2017) Additive manufacturing of PLA structures using fused deposition modelling: Effect of process parameters on mechanical properties and their optimal selection. *Materials & Design*, **124**, 143-157. <https://doi.org/10.1016/j.matdes.2017.03.065>.
29. Ligon, S.C., Liska, R., Stampfl, J., Gurr, M. and Mulhaupt, R. (2017) Polymers for 3D Printing and Customized Additive Manufacturing. *Chem Rev*, **117**, 10212-10290. <https://doi.org/10.1021/acs.chemrev.7b00074>.
30. Wu, W., Geng, P., Li, G., Zhao, D., Zhang, H. and Zhao, J. (2015) Influence of Layer Thickness and Raster Angle on the Mechanical Properties of 3D-Printed PEEK and a Comparative Mechanical Study between PEEK and ABS. *Materials (Basel)*, **8**, 5834-5846. <https://doi.org/10.3390/ma8095271>.
31. Kabir, S.M.F., Mathur, K. and Seyam, A.-F.M. (2020) A critical review on 3D printed continuous fiber-reinforced composites: History, mechanism, materials and properties. *Composite Structures*, **232**, 111476. <https://doi.org/10.1016/j.compstruct.2019.111476>.
32. Hinton, M., Soden, P. and Kaddour, A.-S. (2004) *Failure criteria in fibre reinforced polymer composites: the world-wide failure exercise*. Elsevier.
33. Polyzos, E., Katalagarianakis, A., Polyzos, D., Van Hemelrijck, D. and Pyl, L. (2020) A multi-scale analytical methodology for the prediction of mechanical properties of 3D-printed materials with continuous fibres. *Additive Manufacturing*, **36**, 101394. <https://doi.org/10.1016/j.addma.2020.101394>.

34. Herakovich, C.T. (2012) Mechanics of composites: A historical review. *Mechanics Research Communications*, **41**, 1-20.  
<https://doi.org/10.1016/j.mechrescom.2012.01.006>.
35. Mallick, P.K. (2007) *Fiber-reinforced composites: materials, manufacturing, and design*. CRC press.
36. Kanninen, M.F., McEvily, A. and Popelar, C.H. (1986) *Advanced fracture mechanics*.
37. Dizon, J.R.C., Espera, A.H., Chen, Q. and Advincula, R.C. (2018) Mechanical characterization of 3D-printed polymers. *Additive Manufacturing*, **20**, 44-67.  
<https://doi.org/10.1016/j.addma.2017.12.002>.
38. Carlsson, L.A., Adams, D.F. and Pipes, R.B. (2014) *Experimental characterization of advanced composite materials*. CRC press.
39. Marfia, S. and Sacco, E. (2001) A fracture evolution procedure for cohesive materials. *International journal of fracture*, **110**, 241-261.
40. Sun, C.T. and Jin, Z.H. (2012) In Sun, C. T. and Jin, Z. H. (eds.), *Fracture Mechanics*. Academic Press, Boston, pp. 1-10.
41. Carneiro, O.S., Silva, A.F. and Gomes, R. (2015) Fused deposition modeling with polypropylene. *Materials & Design*, **83**, 768-776.  
<https://doi.org/10.1016/j.matdes.2015.06.053>.
42. Callister, W.D., Rethwisch, D.G., Blicblau, A., Bruggeman, K., Cortie, M., Long, J., Hart, J., Marceau, R., Ryan, M. and Parvizi, R. (2014) *Materials science and engineering: an introduction 9th ed.* wiley.
43. Ning, H., Lu, N., Hassen, A.A., Chawla, K., Selim, M. and Pillay, S. (2019) A review of Long fibre thermoplastic (LFT) composites. *International Materials Reviews*, **65**, 164-188. <https://doi.org/10.1080/09506608.2019.1585004>.
44. Airbus. (2019, August 21). Composites: Airbus continues to shape the future. Airbus. <https://www.airbus.com/newsroom/news/en/2017/08/composites--airbus-continues-to-shape-the-future.html>.
45. van de Werken, N., Tekinalp, H., Khanbolouki, P., Ozcan, S., Williams, A. and Tehrani, M. (2020) Additively manufactured carbon fiber-reinforced composites: State of the art and perspective. *Additive Manufacturing*, **31**, 100962.  
<https://doi.org/10.1016/j.addma.2019.100962>.
46. Li, J., Durandet, Y., Huang, X., Sun, G. and Ruan, D. (2022) Additively manufactured fiber-reinforced composites: A review of mechanical behavior and opportunities. *Journal of Materials Science & Technology*, **119**, 219-244.  
<https://doi.org/10.1016/j.jmst.2021.11.063>.

47. Conti, S., Müller, S. and Ortiz, M. (2018) Data-driven problems in elasticity. *Archive for Rational Mechanics and Analysis*, **229**, 79-123.
48. Meyers, M.A. and Chawla, K.K. (2008) *Mechanical behavior of materials*. Cambridge university press.
49. Elices, M., Guinea, G., Gomez, J. and Planas, J. (2002) The cohesive zone model: advantages, limitations and challenges. *Engineering fracture mechanics*, **69**, 137-163.
50. Erdogan, F. (1995) Fracture mechanics of functionally graded materials. *Composites Engineering*, **5**, 753-770.
51. Sela, N. and Ishai, O. (1989) Interlaminar fracture toughness and toughening of laminated composite materials: a review. *Composites*, **20**, 423-435.
52. Kinloch, A., Lau, C. and Williams, J. (1994) The peeling of flexible laminates. *International Journal of Fracture*, **66**, 45-70.
53. ASTM. (2013), D5528-13 Standard Test Method for Mode I Interlaminar Fracture Toughness of Unidirectional Fiber-Reinforced Polymer Matrix Composites, ASTM International, West Conshohocken, PA, 2013, [www.astm.org/10.1520/D5528-13](http://www.astm.org/10.1520/D5528-13).
54. Goland, M. and Reissner, E. (1944) The stresses in cemented joints.
55. Kendall, K. (1975) Crack propagation in lap shear joints. *Journal of Physics D: Applied Physics*, **8**, 512.
56. Tsai, M.Y. and Morton, J. (1994) An evaluation of analytical and numerical solutions to the single-lap joint. *International Journal of Solids and Structures*, **31**, 2537-2563. [https://doi.org/10.1016/0020-7683\(94\)90036-1](https://doi.org/10.1016/0020-7683(94)90036-1).
57. ASTM. (2016), D4896-01 Standard Guide for Use of Adhesive-Bonded Single Lap-Joint Specimen Test Results. ASTM International, West Conshohocken, PA. <https://doi.org/10.1520/d4896-01r16>.
58. Hart-Smith, L.J. (1973) *Adhesive-bonded single-lap joints*. (No. NASA-CR-112236).
59. Kendall, K. (2021) Energizing ASTM lap joint fracture standards. *Philos Trans A Math Phys Eng Sci*, **379**, 20200287. <https://doi.org/10.1098/rsta.2020.0287>.
60. Blok, L.G., Longana, M.L., Yu, H. and Woods, B.K.S. (2018) An investigation into 3D printing of fibre reinforced thermoplastic composites. *Additive Manufacturing*, **22**, 176-186. <https://doi.org/10.1016/j.addma.2018.04.039>.

61. Caminero, M.A., Chacón, J.M., García-Moreno, I. and Rodríguez, G.P. (2018) Impact damage resistance of 3D printed continuous fibre reinforced thermoplastic composites using fused deposition modelling. *Composites Part B: Engineering*, **148**, 93-103. <https://doi.org/10.1016/j.compositesb.2018.04.054>.
62. Dickson, A.N., Barry, J.N., McDonnell, K.A. and Dowling, D.P. (2017) Fabrication of continuous carbon, glass and Kevlar fibre reinforced polymer composites using additive manufacturing. *Additive Manufacturing*, **16**, 146-152. <https://doi.org/10.1016/j.addma.2017.06.004>.
63. Matsuzaki, R., Ueda, M., Namiki, M., Jeong, T.K., Asahara, H., Horiguchi, K., Nakamura, T., Todoroki, A. and Hirano, Y. (2016) Three-dimensional printing of continuous-fiber composites by in-nozzle impregnation. *Sci Rep*, **6**, 23058. <https://doi.org/10.1038/srep23058>.
64. Araya-Calvo, M., López-Gómez, I., Chamberlain-Simon, N., León-Salazar, J.L., Guillén-Girón, T., Corrales-Cordero, J.S. and Sánchez-Brenes, O. (2018) Evaluation of compressive and flexural properties of continuous fiber fabrication additive manufacturing technology. *Additive Manufacturing*, **22**, 157-164. <https://doi.org/10.1016/j.addma.2018.05.007>.
65. Naranjo-Lozada, J., Ahuett-Garza, H., Orta-Castañón, P., Verbeeten, W.M.H. and Sáiz-González, D. (2019) Tensile properties and failure behavior of chopped and continuous carbon fiber composites produced by additive manufacturing. *Additive Manufacturing*, **26**, 227-241. <https://doi.org/10.1016/j.addma.2018.12.020>.
66. Valoroso, N., Sessa, S., Lepore, M. and Cricri, G. (2013) Identification of mode-I cohesive parameters for bonded interfaces based on DCB test. *Engineering Fracture Mechanics*, **104**, 56-79. <https://doi.org/10.1016/j.engfracmech.2013.02.008>.
67. Camanho, P.P., Davila, C.G. and de Moura, M.F. (2016) Numerical Simulation of Mixed-Mode Progressive Delamination in Composite Materials. *Journal of Composite Materials*, **37**, 1415-1438. <https://doi.org/10.1177/0021998303034505>.
68. Maimí, P., Camanho, P.P., Mayugo, J.A. and Dávila, C.G. (2007) A continuum damage model for composite laminates: Part I – Constitutive model. *Mechanics of Materials*, **39**, 897-908. <https://doi.org/10.1016/j.mechmat.2007.03.005>.
69. Li, S., Thouless, M., Waas, A., Schroeder, J. and Zavattieri, P. (2005) Use of a cohesive-zone model to analyze the fracture of a fiber-reinforced polymer?matrix composite. *Composites Science and Technology*, **65**, 537-549. <https://doi.org/10.1016/j.compscitech.2004.08.004>.
70. Pascual-González, C., Iragi, M., Fernández, A., Fernández-Blázquez, J.P., Aretxabaleta, L. and Lopes, C.S. (2020) An approach to analyse the factors behind the micromechanical response of 3D-printed composites. *Composites Part B: Engineering*, **186**, 107820. <https://doi.org/10.1016/j.compositesb.2020.107820>.

71. Krueger, R. (2012). NASA. <https://ntrs.nasa.gov/citations/20120012955>.
72. Schindelin, J., Arganda-Carreras, I., Frise, E., Kaynig, V., Longair, M., Pietzsch, T., Preibisch, S., Rueden, C., Saalfeld, S., Schmid, B. *et al.* (2012) Fiji: an open-source platform for biological-image analysis. *Nat Methods*, **9**, 676-682. <https://doi.org/10.1038/nmeth.2019>.
73. Markforged Inc. (2022) Materials Datasheet - Composites. <https://web-objects.markforged.com/craft/materials/CompositesV5.2.pdf>.
74. Mankins, J.C. (1995) Technology readiness levels. *White Paper, April*, **6**, 1995.
75. Mankins, J.C. (2009) Technology readiness assessments: A retrospective. *Acta Astronautica*, **65**, 1216-1223. <https://doi.org/10.1016/j.actaastro.2009.03.058>.
76. Héder, M. (2017) From NASA to EU: the evolution of the TRL scale in Public Sector Innovation. *The Innovation Journal*, **22**, 1-23.
77. Budarapu, P.R., Zhuang, X., Rabczuk, T. and Bordas, S.P.A. (2019), *Advances in Crystals and Elastic Metamaterials, Part 2*, pp. 1-103.